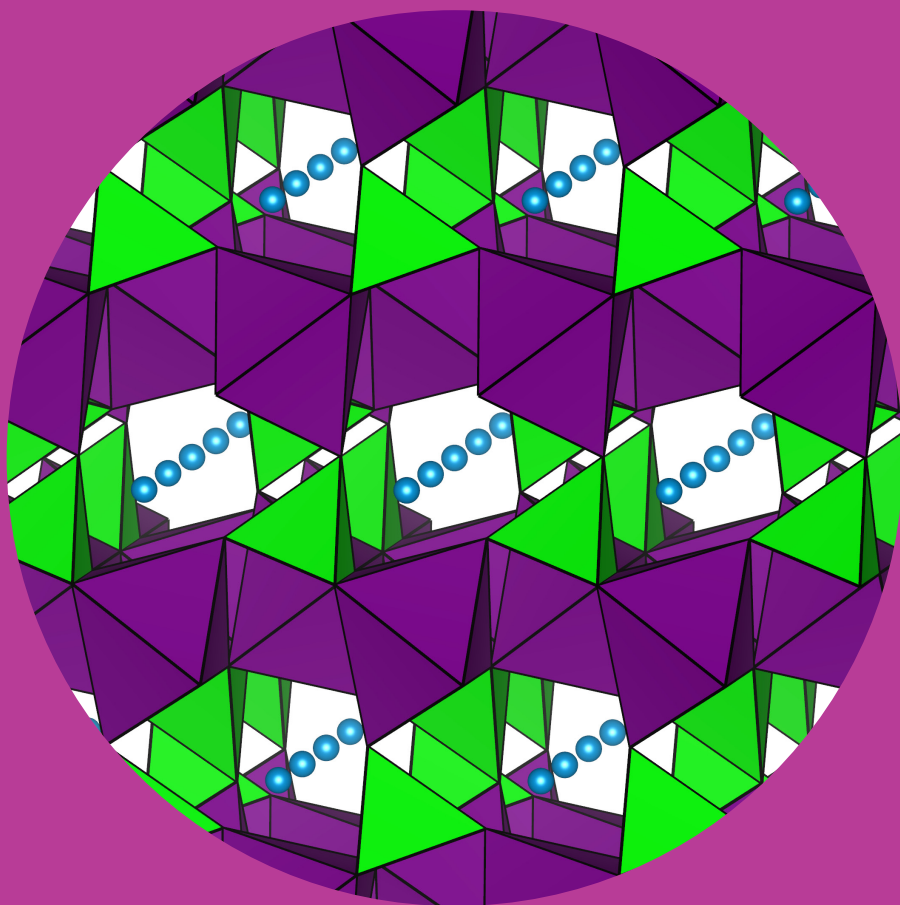


Department of Chemistry

# Electrode Material Solutions for Large-Scale Lithium-Ion Batteries

---

Kirsi Jalkanen



# Electrode Material Solutions for Large-Scale Lithium-Ion Batteries

**Kirsi Jalkanen**

A doctoral dissertation completed for the degree of Doctor of Science (Technology) to be defended, with the permission of the Aalto University School of Chemical Technology, at a public examination held at the lecture hall Ke2 of the school on 14 December 2015 at 12.

**Aalto University**  
**School of Chemical Technology**  
**Department of Chemistry**  
**Laboratory of Inorganic Chemistry**

**Supervising professor**

Professor Maarit Karppinen

**Thesis advisor**

Adjunct Professor Kai Vuorilehto

**Preliminary examiners**

Docent Torbjörn Gustafsson, Uppsala University, Sweden

Professor Martin Winter, University of Münster, Germany

**Opponents**

Professor Margret Wohlfahrt-Mehrens, ZSW Centre for Solar Energy and Hydrogen Research Baden-Württemberg, Germany

Aalto University publication series

**DOCTORAL DISSERTATIONS** 204/2015

© Kirsi Jalkanen

ISBN 978-952-60-6551-9 (printed)

ISBN 978-952-60-6552-6 (pdf)

ISSN-L 1799-4934

ISSN 1799-4934 (printed)

ISSN 1799-4942 (pdf)

<http://urn.fi/URN:ISBN:978-952-60-6552-6>

Unigrafia Oy

Helsinki 2015

Finland

**Author**

Kirsi Jalkanen

**Name of the doctoral dissertation**

Electrode Material Solutions for Large-Scale Lithium-Ion Batteries

**Publisher** School of Chemical Technology

**Unit** Department of Chemistry

**Series** Aalto University publication series DOCTORAL DISSERTATIONS 204/2015

**Field of research** Inorganic Chemistry, Electrochemistry

**Manuscript submitted** 14 August 2015

**Date of the defence** 14 December 2015

**Permission to publish granted (date)** 28 October 2015

**Language** English

**Monograph**

**Article dissertation (summary + original articles)**

**Abstract**

Lithium-ion (Li-ion) batteries have become the power source of large-scale applications, such as electric or hybrid-electric vehicles and energy storage systems, in addition to their conventional use in small consumer electronics. However, the traditional electrode materials do not meet the requirements of safety and lifetime, which are emphasized in the large battery packs. Furthermore, for transportation purposes, a high energy density is needed. The aim of this thesis was to study different electrode materials from these perspectives.

The lifetime of commercial Li-ion cells was studied under different cycling temperatures. Especially after prolonged cycling at elevated temperature, the graphite negative electrode was found to be not only the main source of aging but also a safety risk as dendritic Li depositions, a potential source of short-circuits, were observed. Possible reasons promoting Li plating could be the extensive passivation layer growth on graphite and the consequential cell drying and formation of gaseous components.

A new alternative to the graphite negative electrode is  $\text{Li}_4\text{Ti}_5\text{O}_{12}$  which however decreases the cell voltage thus sacrificing the energy density. This sets a demand for novel, safe, high-voltage positive electrodes of which mixed  $\text{Li}(\text{Fe}_{1-y}\text{M}_y)\text{PO}_4$  ( $M = \text{Co}, \text{Ni}$ ) materials were investigated in this work. A beneficial, mutual influence of the Fe and  $M$  occupying the same lattice site was observed as *e.g.* shift of redox potentials and changes in the delithiation/lithiation reaction mechanisms. Especially the local environment of  $\text{Fe}^{3+}$  was affected by the substitution. An optimal composition for the Co substitution is around  $\text{Li}(\text{Fe}_{0.5}\text{Co}_{0.5})\text{PO}_4$ . In the case of the Ni substitution, on the other hand, the  $\text{Ni}^{2+}/\text{Ni}^{3+}$  redox couple could not be reversibly activated, presumably due to lack of electrical conductivity or possible structural changes.

Knowledge of the heat generation in a Li-ion cell is needed for accurate design of cooling systems and thus avoiding the undesirable cell temperature increase. The reversible part of heat generation depends on the entropy change in the electrode materials during the cell reaction, affected mainly by the arrangement of Li in the electrode lattices. In this work, the entropy change behavior was studied for  $\text{LiFePO}_4$ ,  $\text{Li}(\text{Fe}_{0.33}\text{Mn}_{0.67})\text{PO}_4$ , graphite, and  $\text{Li}_4\text{Ti}_5\text{O}_{12}$  electrode materials and their combinations. Specific materials and states of charge were determined to be unfavorable due to extra heat generation. Furthermore, the effect of Mn substituent was observed in the entropy change behavior of  $\text{Li}(\text{Fe}_{0.33}\text{Mn}_{0.67})\text{PO}_4$ . The impact of reversible heat generation was demonstrated in practice as a cooling effect during the discharge of a commercial Li-ion cell.

**Keywords** Li-ion battery, positive electrode, negative electrode, aging, post-mortem analysis,  $\text{LiFePO}_4$ , chemical substitution, reversible heat generation, entropy change

**ISBN (printed)** 978-952-60-6551-9

**ISBN (pdf)** 978-952-60-6552-6

**ISSN-L** 1799-4934

**ISSN (printed)** 1799-4934

**ISSN (pdf)** 1799-4942

**Location of publisher** Helsinki

**Location of printing** Helsinki

**Year** 2015

**Pages** 137

**urn** <http://urn.fi/URN:ISBN:978-952-60-6552-6>



**Tekijä**

Kirsi Jalkanen

**Väitöskirjan nimi**

Elektrodimateriaaliratkaisut suuren koon litiumioniakkuihin

**Julkaisija** Kemian tekniikan korkeakoulu**Yksikkö** Kemian laitos**Sarja** Aalto University publication series DOCTORAL DISSERTATIONS 204/2015**Tutkimusala** Epäorgaaninen kemia, sähkökemiala**Käsikirjoituksen pvm** 14.08.2015**Väitöspäivä** 14.12.2015**Julkaisuluvan myöntämispäivä** 28.10.2015**Kieli** Englanti **Monografia** **Yhdistelmäväitöskirja (yhteenvedo-osa + erillisartikkelit)****Tiivistelmä**

Kannettavan elektroniikan lisäksi litiumioniakkuja on alettu käyttää suuremmissa sovelluskohteissa, kuten sähkö- ja hybridiajoneuvoissa sekä stationäärisissä energiavarastoissa. Perinteisesti käytetyt elektrodimateriaalit eivät kuitenkaan vastaa suurissa akustoissa korostuvia turvallisuus- ja elinikävaatimuksia. Liikkuvien sovellusten akustolta vaaditaan myös korkea energiatiheys. Tämän työn tarkoituksena oli tutkia erilaisia elektrodimateriaaleja näistä näkökulmista.

Kaupallisten litiumioniakkujen elinikää tutkittiin käyttämällä niitä eri lämpötiloissa. Grafiit-negatiivielektrodin huomattiin olevan paitsi suurin syy kennon ikääntymiseen myös turvallisuusriski. Erityisesti kun kennoa oli käytetty pitkäaikaisesti korkeassa lämpötilassa, siihen havaittiin syntyneen dendriittistä litiumsostumaa, joka voi johtaa oikosulkuun. Mahdollisia litiumsostuman syntyyn vaikuttaneita tekijöitä olivat grafiitin passiivikerroksen voimakas kasvu ja siitä seurannut kennon kuivuminen sekä kaasumaisten yhdisteiden muodostuminen.

Uusi vaihtoehto grafiit-negatiivielektrodille on  $\text{Li}_4\text{Ti}_5\text{O}_{12}$ , mutta sen antama kennojännite on matala ja täten akun energiatiheys laskee. Tästä syystä tarvitaan turvallisia korkean jännitteen positiivielektrodeja, joista tässä työssä tutkittiin seostettuja  $\text{Li}(\text{Fe}_{1-y}\text{M}_y)\text{PO}_4$  ( $M = \text{Co}, \text{Ni}$ ) -materiaaleja. Samaa hilapaikkaa miehittävien Fe:n ja M:n edullinen yhteisvaikutus havaittiin muun muassa hapetus-pelkistyspotentiaalien ja litiointimekanismien muuttumisena. Erityisesti  $\text{Fe}^{3+}$ -n kemiallisen ympäristön huomattiin muuttuvan, kun osa raudasta korvattiin M-metallilla. Co-korvatuille materiaaleille optimaalinen koostumus on noin  $\text{Li}(\text{Fe}_{0.5}\text{Co}_{0.5})\text{PO}_4$ , mutta Ni-seostettujen materiaalien  $\text{Ni}^{2+}/\text{Ni}^{3+}$ -paria ei saatu reagoimaan reversiibelisti. Tämän oletettiin johtuvan liian alhaisesta sähkönjohtavuudesta tai mahdollisista rakennemuutoksista.

Jotta akun jäähditysjärjestelmä osataan suunnitella tarkasti ja välttämään ei-toivotulta lämpötilan nousulta, on yksittäisen litiumionikennon lämmöntuotto tunnettava. Lämmöntuoton reversiibeli osa riippuu elektrodimateriaaleissa tapahtuvista entropianmuutoksista, joihin vaikuttaa pääasiassa litiumin järjestäytyminen niiden hilarakenteissa. Tässä työssä tutkittiin eri elektrodimateriaalien ( $\text{LiFePO}_4$ ,  $\text{Li}(\text{Fe}_{0.33}\text{Mn}_{0.67})\text{PO}_4$ , grafiitti ja  $\text{Li}_4\text{Ti}_5\text{O}_{12}$ ) sekä niiden yhdistelmien entropiakäyttäytymistä. Tiettyjen materiaalien ja kennon latausasteiden havaittiin olevan epäsuotuisia aiheuttaen ylimääräistä lämmöntuottoa. Lisäksi Mn-korvauksen huomattiin muuttavan  $\text{Li}(\text{Fe}_{0.33}\text{Mn}_{0.67})\text{PO}_4$ -materiaalin entropiakäyttäytymistä. Reversiibelin lämmöntuoton vaikutus osoitettiin käytännössä kaupallisen kennon jäähtymisenä sitä purettaessa.

**Avainsanat** litiumioniakku, positiivielektrodi, negatiivielektrodi, ikääntyminen, post mortem -analyysi,  $\text{LiFePO}_4$ , kemiallinen substituuio, reversiibeli lämmöntuotto, entropianmuutos

**ISBN (painettu)** 978-952-60-6551-9**ISBN (pdf)** 978-952-60-6552-6**ISSN-L** 1799-4934**ISSN (painettu)** 1799-4934**ISSN (pdf)** 1799-4942**Julkaisupaikka** Helsinki**Painopaikka** Helsinki**Vuosi** 2015**Sivumäärä** 137**urn** <http://urn.fi/URN:ISBN:978-952-60-6552-6>



# Preface

The work presented in this dissertation was carried out in the Laboratory of Inorganic Chemistry at Aalto University School of Chemical Technology (between October 2013 and August 2015) and at European Batteries Ltd. (between May 2011 and July 2013). Tekes (Finnish Funding Agency for Innovation), European Batteries Ltd., and Walter Ahlström Foundation are gratefully acknowledged for financially supporting this work.

My great gratitude belongs to Prof. Maarit Karppinen for giving me the opportunity to continue and finish this thesis under her supervision, and for all her invaluable help and support in the inorganic chemistry field. I am extremely thankful to my instructor Adjunct Prof. Kai Vuorilehto for introducing me to the world of lithium-ion batteries and teaching me indescribably much about them, and about research in general.

I want to thank my co-authors and the people who have contributed to my work. Special thanks belongs to the fellow lithium-ion battery researches at the Department of Chemistry; Adjunct Prof. Tanja Kallio, Ms. Elina Pohjalainen, and especially Ms. Taina Rauhala and Mr. Mikko Nisula have given me a great deal of help and support in both practical and theoretical matters. I am very grateful to the inorganic chemistry colleagues for sharing their knowledge with me. Above all, I want to thank Ms. Satu Manner for all her help in the beginning and Mr. Otto Mustonen, Mr. Taneli Tiittanen, and Dr. Sami Vasala for their advice. I am also thankful to Dr. Johan Lindén for introducing me to Mössbauer spectroscopy. For the early stages of this work, I want to thank my former colleagues at European Batteries, in particular Mr. Matti Nuutinen and Mr. Timo Aho. For collaboration, I am grateful to Prof. Ulla Lassi's group at Kokkola University Consortium Chydenius and to Dr. Juha Karppinen, Assoc. Prof. Tomi Laurila, Mr. Lasse Skogström, Mr. Ari Hentunen, and Mr. Panu Sainio from Aalto University.

I want to thank the members of the Laboratory of Inorganic Chemistry for a very pleasant and inspiring working atmosphere. *Thin Solid Pancakes* people have made my day, and not only the Thursday.

To my dear friends, for always being there for me. To my parents, for their endless love, encouragement, and support. Thank you!

Espoo, October 2015

Kirsi Jalkanen



# Contents

List of Abbreviations and Symbols .....	i
List of Publications .....	iii
Author's Contribution .....	v
1. Introduction.....	1
1.1 Demands for Large-Scale Li-Ion Battery Electrode Materials..	1
1.2 Electrode Material Choices for Li-Ion Batteries.....	3
1.2.1 Positive Electrodes.....	4
1.2.2 Negative Electrodes .....	5
1.3 Scope of the Present Thesis.....	6
2. Aging of Li-Ion Cells.....	8
2.1 Typical Aging Mechanisms.....	8
2.2 Determining Aging Mechanisms by Post-Mortem Analysis .....	9
2.3 Effect of Electrode Materials.....	10
2.4 Effect of Temperature.....	12
2.4.1 Aging at High Temperatures .....	12
2.4.2 Aging at Low Temperatures.....	14
2.4.3 Comparison of Li Plating at Different Temperatures .....	15
3. $\text{Li}(\text{Fe}_{1-y}\text{M}_y)\text{PO}_4$ ( $M = \text{Mn, Co, Ni}$ ) Positive Electrodes .....	18
3.1 Isovalent Substitution at the Fe Site .....	19
3.1.1 Effect on Lattice Parameters .....	20
3.1.2 Effect on Fe Local Structure .....	22
3.2 Electrochemical Performance .....	25
3.2.1 $M^{2+}/M^{3+}$ Redox Couple Activity .....	25
3.2.2 Shift of Redox Potentials .....	27
3.2.3 Dependence on Substitution Level.....	29
3.3 Delithiation/Lithiation Characteristics .....	30
3.3.1 End Members $\text{LiMPO}_4$ ( $M = \text{Mn, Fe, Co, Ni}$ ).....	31
3.3.2 Mixed $\text{Li}(\text{Fe},M)\text{PO}_4$ ( $M = \text{Mn, Co, Ni}$ ).....	32
4. Reversible Heat Generation in Li-Ion Cells.....	36

4.1	Thermodynamic Relations of a Li-Ion Cell .....	36
4.2	Measuring the Entropy Change .....	38
4.3	Entropy Change in Different Electrode Materials .....	39
4.4	Entropy Change in Full Cells .....	42
5.	Conclusions .....	46
	References .....	49

# List of Abbreviations and Symbols

CV	Cyclic voltammetry
DMC	Dimethyl carbonate
EDS	Energy dispersive X-ray spectroscopy
EOL	End of life
ESS	Energy storage system
EV	Electric vehicle
HEV	Hybrid electric vehicle
ICP	Inductively coupled plasma
IR	Infrared spectroscopy
IS	Isomer shift
OCV	Open circuit voltage
PHEV	Plug-in hybrid electric vehicle
QS	Quadrupole splitting
SEI	Solid electrolyte interface
SEM	Scanning electron microscopy
SOC	State of charge
XAS	X-ray absorption spectroscopy
XPS	X-ray photoelectron spectroscopy
XRD	X-ray diffraction spectroscopy

$\Delta G$	Gibbs free energy change
$\Delta H$	Enthalpy change
$\Delta S$	Entropy change

$F$	Faraday's constant
$I$	Current
$M$	Transition metal
$n$	Number of electrons involved in cell reaction
$Q$	Heat generation rate
$R_i$	Internal resistance
$R_\Omega$	Ohmic resistance
$R_{pol}$	Polarization resistance
$T$	Temperature

# List of Publications

This doctoral dissertation consists of a summary and of the following publications which are referred to in the text by their Roman numerals.

- I** K. Jalkanen, T. Aho and K. Vuorilehto, Entropy change effects on the thermal behavior of a  $\text{LiFePO}_4$ /graphite lithium-ion cell at different states of charge, *Journal of Power Sources* **243** (2013) 354-360.
- II** K. Jalkanen and K. Vuorilehto, Entropy change characteristics of  $\text{LiMn}_{0.67}\text{Fe}_{0.33}\text{PO}_4$  and  $\text{Li}_4\text{Ti}_5\text{O}_{12}$  electrode materials, *Journal of Power Sources* **273** (2015) 351-359.
- III** K. Jalkanen, J. Karppinen, L. Skogström, T. Laurila, M. Nisula and K. Vuorilehto, Cycle aging of commercial NMC/graphite pouch cells at different temperatures, *Applied Energy* **154** (2015) 160-172.
- IV** K. Jalkanen, J. Lindén and M. Karppinen, Local structures in mixed  $\text{Li}_x\text{Fe}_{1-y}\text{M}_y\text{PO}_4$  ( $M = \text{Co}, \text{Ni}$ ) electrode materials, *Journal of Solid State Chemistry* **230** (2015) 404-410.
- V** K. Jalkanen and M. Karppinen, Electrochemical Performance and Delithiation/Lithiation Characteristics of Mixed  $\text{LiFe}_{1-y}\text{M}_y\text{PO}_4$  ( $M = \text{Co}, \text{Ni}$ ) Electrode Materials, *Journal of The Electrochemical Society* **162** (14) (2015) A2780-A2788.



# Author's Contribution

**Publication I:** Entropy change effects on the thermal behavior of a  $\text{LiFePO}_4$ /graphite lithium-ion cell at different states of charge

The author defined the research plan together with the co-authors and carried out a major part of the experimental work. The results were interpreted together with the co-authors. The author had a major role in writing the manuscript.

**Publication II:** Entropy change characteristics of  $\text{LiMn}_{0.67}\text{Fe}_{0.33}\text{PO}_4$  and  $\text{Li}_4\text{Ti}_5\text{O}_{12}$  electrode materials

The author defined the research plan together with the co-author. The author carried out all the experimental work. The results were interpreted together with the co-author. The author had a major role in writing the manuscript.

**Publication III:** Cycle aging of commercial NMC/graphite pouch cells at different temperatures

The author had a supporting role in defining the research plan. The author carried out the cell disassembly together with the co-authors and did the impedance measurements. The author interpreted the results together with the co-authors and had a major role in writing the manuscript.

**Publication IV:** Local structures in mixed  $\text{Li}_x\text{Fe}_{1-y}\text{M}_y\text{PO}_4$  ( $M = \text{Co}, \text{Ni}$ ) electrode materials

The author defined the research plan and carried out all the experimental work. The results were interpreted together with the co-authors. The author had a major role in writing the manuscript.

**Publication V:** Electrochemical Performance and Delithiation/Lithiation Characteristics of Mixed  $\text{LiFe}_{1-y}\text{M}_y\text{PO}_4$  ( $M = \text{Co}, \text{Ni}$ ) Electrode Materials

The author defined the research plan and carried out all the experimental work. The results were interpreted together with the co-author. The author had a major role in writing the manuscript.



# 1. Introduction

Lithium-ion (Li-ion) batteries were first introduced in small, portable consumer electronics, such as cell phones, laptops, and power tools. The most significant advantages of the Li-ion technology were the increased energy density, both gravimetric and volumetric, the longer lifetime, and the flexible and lightweight design possibilities, when compared to competing nickel-cadmium or nickel-metal hydride chemistries.<sup>1</sup>

In recent years, in addition to the small-sized consumer electronics, Li-ion batteries have become the power source for electric vehicles (EV), hybrid or plug-in hybrid electric vehicles (HEV/PHEV), and stationary energy storage systems (ESS). The battery utilization in automotive and energy storage fields is growing rapidly: it is expected to show an over 80% share of all rechargeable battery market, overtaking the portable consumer electronics sector.<sup>2</sup> The replacement of fossil fuels with Li-ion batteries in the automotive applications is driven by energy and environmental issues. However, the governmental policies and support play a significant role, too. For the energy storage systems, a growing demand has emerged from the increased use of renewable energy sources and from the overall increasing consumption of electricity.

In the following, the requirements that large-scale applications set on the Li-ion battery technology are discussed and the different positive and negative electrode material choices are shortly reviewed.

## 1.1 Demands for Large-Scale Li-Ion Battery Electrode Materials

Li-ion battery technology was first commercialized by Sony in 1991. The electrode materials comprised of lithium cobalt oxide ( $\text{LiCoO}_2$ ) as the positive electrode and carbon as the negative electrode. Unlike the earlier Li-metal batteries with Li-metal negative electrode, this “rocking-chair” battery type was based on Li-ion transfer between two intercalation electrodes, which are able to store the Li-ions in their lattices.<sup>3</sup> Replacing the Li-metal electrode significantly improved the lifetime and safety. The  $\text{LiCoO}_2/\text{C}$  electrode combination is still widely used in small consumer electronics as it gives a good energy density. However, these electrode materials are far from optimal for a large battery pack in automotive and energy storage applications. For small-sized devices, a single battery cell or a few cells are often used. On the contrary, large-scale applications like EVs utilize hundreds or thousands of cells, which are connected in series or parallel to form modules and further battery packs. Moreover, the battery lifetime should be longer than the expected life of the powered ap-

plication. Due to this scale-up, different requirements for the single cells are emphasized.

In general, poor intrinsic safety, insufficient lifetime, and high cost are the limiting factors for the Li-ion battery technology in large-scale applications.<sup>2,4-6</sup> Furthermore, especially for EV applications, a high energy density is required for a sufficiently long driving range. Improved fast-charging and low-temperature performance characteristics are needed, too.<sup>4,6</sup> A summary of the USABC (United States Advanced Battery Consortium LLC) goals for EV battery cells is presented in Table 1.

**Table 1.** Summary of USABC goals for Advanced Batteries for EVs at cell level (2020 commercialization).<sup>7</sup>

Characteristics at end of life	Cell level
Energy density, volumetric (C/3 discharge)	750 Wh/l
Energy density, gravimetric (C/3 discharge)	350 Wh/kg
Peak discharge pulse power (30 s)	700 W/kg
Calendar life	15 years
Cycle life	1000 cycles
Operating environment	-30 °C to +52 °C

The energy density goals in Table 1 are not yet achieved.<sup>5,6</sup> The battery energy density is defined as the amount of electrical energy per unit of weight or volume (Wh/kg or Wh/l). It is the product of cell capacity (Ah/kg or Ah/l) and voltage (V). These quantities directly depend on the electrode materials, which should show a high capacity and produce a high cell voltage (high redox potential for the positive and low for the negative electrode). The electrode materials should also retain their capacity and voltage characteristics with increasing current rate (show a good rate capability). Due to the inactive components, like cooling systems and safety devices, the energy density at the battery pack level is roughly only a quarter of the active materials' energy density.<sup>6</sup>

At the moment, the lifetime requirement of 15 years and 1 000 cycles (Table 1) is regarded unproven.<sup>5</sup> A Li-ion cell is defined to have reached its end of life (EOL) when the reversible capacity has reduced to 80% of its original value. Thus for a long lifetime, the cell capacity fade should be slow. Further, to fulfil the power requirements, the internal resistance should remain small. In general, side reactions at electrode-electrolyte interfaces are regarded to be detrimental for the battery lifetime.<sup>1</sup> Side reactions occur if the electrode's potential is outside the electrolyte's stability window. Additionally, for improved durability, the lithium insertion/extraction should not result in large volume changes in the electrode material lattices.

To meet the operating temperature requirements, the battery should be viable, retain sufficient energy and power characteristics, and operate safely both at high and low temperatures. The cost of Li-ion batteries should still be significantly reduced; the price can be brought down by mass production, but the raw materials and their processing are still expensive.<sup>5</sup>

In addition to the performance characteristics in Table 1, the cell safety is a crucial issue. Li-ion batteries have caused fires and explosions, as they are not inherently tolerant to abusive conditions, like over-charge or over-discharge, short-circuits or exposure to very high temperatures.<sup>5,8</sup> In the case of a large-sized battery, the consequences of battery fire or explosion are extremely detrimental. A battery failure

commonly occurs due to thermal runaway reactions inside the cells.<sup>8</sup> In a thermal runaway, an exothermic reaction proceeds in an uncontrollable manner; the reaction is accelerated by temperature increase, which causes a further increase in temperature. Thermal runaway is generally triggered by exothermic decomposition of an electrode-electrolyte interface layer. This decomposition can take place already at temperatures below 100 °C, and it eventually leads to breakdown of the electrode materials. Thus for improved safety, the stability of the electrode-electrolyte interfaces and the electrode materials (at all Li contents) is important, and their thermal decomposition temperatures should be high.<sup>1,2,8</sup> A less exothermic decomposition reaction is beneficial for the safety. Moreover, oxygen should not be released from the electrode material lattice, as it will result in electrolyte combustion and eventually explosion and fire of the battery. No metallic Li plating (Li reduced as metallic on the negative electrode) should occur, as it may lead to growth of Li dendrites. Such dendrites can penetrate the separator and give rise to an internal short-circuit and strong temperature increase inside the cell,<sup>9–11</sup> which can further cause thermal runaway. Avoiding cell failure conditions is especially important for large-scale batteries, as thermal runaway in an individual cell is likely to propagate to the entire battery pack.<sup>12</sup>

## 1.2 Electrode Material Choices for Li-Ion Batteries

The crystal structures of different positive and negative electrode materials are presented in Figure 1.

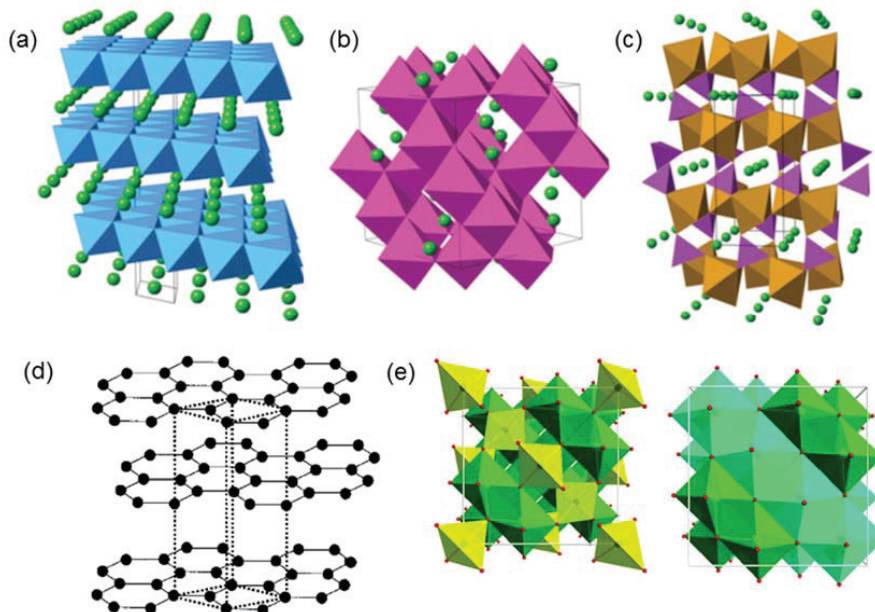


**Figure 1.** Different positive and negative electrode material structures. (a)  $\text{LiCoO}_2$ ,<sup>13</sup> (b)  $\text{LiMn}_2\text{O}_4$ ,<sup>13</sup> (c)  $\text{LiFePO}_4$ ,<sup>13</sup> (d) graphite,<sup>14,adopted</sup> and (e) left  $\text{Li}_4\text{Ti}_5\text{O}_{12}$ , right  $\text{Li}_7\text{Ti}_5\text{O}_{12}$ .<sup>15</sup>

### 1.2.1 Positive Electrodes

#### *LiMO<sub>2</sub>*

Layered metal oxides  $\text{LiMO}_2$  ( $M = \text{Co}, \text{Ni}$ ) show a rhombohedral,  $\alpha\text{-NaFeO}_2$ -type rock salt structure (space group  $R\bar{3}m$ ), presented in Figure 1a. The Co-based  $\text{Li}_x\text{CoO}_2$  was first investigated by Mizushima *et al.*<sup>16</sup> in 1980. It has a relatively high operating voltage (3.9 V vs.  $\text{Li}/\text{Li}^+$ ), but the reversible specific capacity is only 140 mAh/g, because the lattice becomes unstable if more than half of the Li-ions are removed.<sup>17,18</sup> As a consequence, upon over-charge ( $x < 0.5$ ) and temperature increase, the lattice may collapse releasing oxygen: the decomposition forms a severe safety risk. In addition, the high cost and environmental impact of Co restrict its use. The Ni-variant  $\text{Li}_x\text{NiO}_2$  on the other hand offers a higher specific capacity (200 mAh/g),<sup>19–21</sup> and it is more environmentally friendly and cost effective. However, its structural stability is even worse compared to the  $\text{Li}_x\text{CoO}_2$  phase, and synthesizing stoichiometric materials is difficult due to Li-Ni exchange.

As alternatives, mixed layered oxides, such as  $\text{Li}(\text{Ni}_{1-y}\text{Co}_y)\text{O}_2$  and  $\text{Li}(\text{Ni}_{1-y-z}\text{Co}_y\text{Al}_z)\text{O}_2$  (typically  $\text{Li}(\text{Ni}_{0.8}\text{Co}_{0.15}\text{Al}_{0.05})\text{O}_2$ ), have been proposed. They are isostructural with  $\text{LiNiO}_2$  and  $\text{LiCoO}_2$ , but the partial substitution of Ni with Co improves the stability and on the other hand, higher specific capacities are achieved in comparison to  $\text{LiCoO}_2$ .<sup>22,23</sup> Adding small amounts of electrochemically inactive Al further enhances the structural and chemical stability. However, the delithiated material is still prone to decomposition and oxygen release at high temperatures.<sup>24,25</sup>

Further improvements have been achieved with  $\text{Li}(\text{Ni}_{1-y-z}\text{Co}_y\text{Mn}_z)\text{O}_2$  (typically  $\text{Li}(\text{Ni}_{1/3}\text{Co}_{1/3}\text{Mn}_{1/3})\text{O}_2$ )<sup>26,27</sup> materials. During charging,  $\text{Co}^{3+}$  is oxidized to  $\text{Co}^{4+}$  and  $\text{Ni}^{2+}$  to  $\text{Ni}^{4+}$ , but  $\text{Mn}^{4+}$  remains inactive, providing structural stability.<sup>28</sup>  $\text{Li}(\text{Ni},\text{Co},\text{Mn})\text{O}_2$  materials show a reversible specific capacity of 150 - 200 mAh/g and an improved structural and thermal stability in comparison to  $\text{Li}(\text{Ni},\text{Co},\text{Al})\text{O}_2$  materials.<sup>25,29</sup> However, also  $\text{Li}(\text{Ni},\text{Co},\text{Mn})\text{O}_2$  eventually releases oxygen at high temperatures, and structural changes upon cycling limit its rate capability and lifetime.<sup>30–32</sup>

#### *LiMn<sub>2</sub>O<sub>4</sub>*

The cubic spinel structured  $\text{LiMn}_2\text{O}_4$  (space group  $Fd\bar{3}m$ ),<sup>33–35</sup> presented in Figure 1b, is an environmentally friendly, low-cost alternative to the layered oxides. It shows a 4 V vs.  $\text{Li}/\text{Li}^+$  operating voltage and an improved structural stability, but the reversible specific capacity is only 120 mAh/g. Furthermore, the material suffers from fast capacity fade, especially at elevated temperatures. This is caused by structural changes, instability of  $\text{Mn}^{3+}$  (Jahn-Teller distortion), and  $\text{Mn}^{2+}$  dissolution through the  $\text{Mn}^{3+}$  disproportionation reaction.<sup>35–38</sup> Better performance can be achieved by doping or using blends of  $\text{LiMn}_2\text{O}_4$  and  $\text{Li}(\text{Ni},\text{Co},\text{Mn})\text{O}_2$ . Moreover, Li- and Mn-rich  $\text{Li}_2\text{MnO}_3$ -stabilized  $\text{LiMO}_2$  ( $M = \text{Mn}, \text{Ni}, \text{Co}$ ) electrodes have been proposed.<sup>39</sup>

#### *LiMPO<sub>4</sub>*

Olivine-structured metal phosphates  $\text{LiMPO}_4$  ( $M = \text{Mn}, \text{Fe}, \text{Co}, \text{Ni}$ ) were first introduced by the group of Goodenough *et al.*<sup>40</sup> in 1997. They are interesting alternatives to the positive electrode due to the intrinsically stable, three-dimensional orthorhombic lattice (space group  $Pnma$ ), depicted in Figure 1c. The strong P-O bonds in

$\text{PO}_4^{3-}$  polyanions stabilize the structure and prevent the release of oxygen, even at elevated temperatures and without Li at the charged state. The theoretical specific capacity is approx. 170 mAh/g.

Of the metal phosphate group,  $\text{LiFePO}_4$  is already in commercial use. It shows a long cycle life, high safety, and high thermal stability.<sup>1,41–44</sup> Furthermore,  $\text{LiFePO}_4$  is non-toxic and cheap. The electronic and ionic conductivity properties are poor, but this issue has been overcome by decreasing the particle size and coating the particles with carbon.<sup>44,45</sup> However, compared to the layered oxides and  $\text{LiMn}_2\text{O}_4$ , the equilibrium potential of  $\text{LiFePO}_4$  is low (3.4 V vs.  $\text{Li}/\text{Li}^+$ ),<sup>40</sup> which decreases the achievable energy density.

$\text{LiMnPO}_4$  shows a promising equilibrium potential of 4.1 V vs.  $\text{Li}/\text{Li}^+$ ,<sup>40</sup> but it suffers from large polarization and the practical reversible capacity is low. The underlying reasons are the poor electrical conductivity (lower than for  $\text{LiFePO}_4$ ),<sup>46–48</sup> and the Jahn-Teller distortion of  $\text{Mn}^{3+}$  in the charged (delithiated) state. The latter leads to a large lattice volume change and mismatch between the  $\text{LiMnPO}_4$  and  $\text{MnPO}_4$  phases.<sup>46,49,50</sup>

The equilibrium potential of  $\text{LiCoPO}_4$  on the other hand is even higher, 4.8 V vs.  $\text{Li}/\text{Li}^+$ ,<sup>51,52</sup> However, practical discharge capacities of only 100 – 120 mAh/g or less are achieved and the capacity fade is fast.<sup>51,53–59</sup> The poor electrochemical performance has been attributed to the low electronic conductivity (lower than for  $\text{LiFePO}_4$ ),<sup>60,61</sup> slow Li diffusion,<sup>62,63</sup> and electrolyte oxidation at high potentials.<sup>55,57</sup> Moreover, structural changes<sup>64</sup> and instability of the delithiated  $\text{CoPO}_4$  phase may affect the performance.<sup>55,65</sup>

For  $\text{LiNiPO}_4$ , a very high equilibrium potential of approx. 5.1 V vs.  $\text{Li}/\text{Li}^+$  is predicted by calculations.<sup>66</sup> Experimentally, oxidation at 5.3 V and reduction at 5.1 V vs.  $\text{Li}/\text{Li}^+$  has been reported.<sup>67</sup> However, the reversible electrochemical activation of the  $\text{Ni}^{2+}/\text{Ni}^{3+}$  redox couple has been only rarely achieved in non-aqueous electrolytes,<sup>67,68</sup> and many studies report no significant electrochemical activity.<sup>51,69–71</sup> The very poor electronic conductivity (lower than for Fe and Co counterparts),<sup>67,72</sup> small lattice volume for Li diffusion,<sup>67</sup> and large particle size related to synthesis conditions<sup>70</sup> have been proposed to cause the lack of redox activity. In addition, Li-Ni site exchange, blocking the Li diffusion channels, has been speculated.<sup>73</sup> No stable phase is known for the delithiated  $\text{NiPO}_4$ .<sup>67,70,73</sup>

### 1.2.2 Negative Electrodes

#### *Graphite*

Graphite is the most commonly used carbonaceous negative electrode material. It consists of stacked graphene sheets (space group  $P6_3/mmc$ ), illustrated in Figure 1d. Graphite shows a specific capacity of 372 mAh/g for the fully lithiated  $\text{LiC}_6$  composition, and the operating voltage is 0.2 – 0.1 V vs.  $\text{Li}/\text{Li}^+$ . Li intercalates into graphite lattice by filling the gaps between neighboring graphene layers in an ordered, step-wise manner (*staging*).<sup>74</sup> The Li distribution is described by the number of graphene layers between layers of intercalated Li. With increasing Li content (charging), the intercalation proceeds along the following stages: dilute stage-1' (random intercalation), stage-4, stage-3, liquid-like stage-2L (incomplete intercalation), ordered stage-2, and ordered stage-1 ( $\text{LiC}_6$ ).<sup>74</sup> Although graphite is abundant, cheap, and non-toxic,

it has severe drawbacks. The volume change related to the Li intercalation is quite high, 10%. Additionally, although the low potential is beneficial for the cell energy density, it leads to safety and durability problems. Firstly, as the potential of lithiated graphite is outside the electrolyte's stability window, a passivating solid electrolyte interface (SEI) layer is needed on the graphite surface,<sup>75-77</sup> which restricts the lifetime and introduces a safety risk. Secondly, the risk of Li reducing as metallic on the graphite electrode surface is significant, as the potential is very close to 0 V vs. Li/Li<sup>+</sup>.<sup>78-81</sup> In addition to other problems, the Li plating can result in growth of Li dendrites.

#### *Li<sub>4</sub>Ti<sub>5</sub>O<sub>12</sub>*

The spinel-structured lithium titanate Li<sub>4</sub>Ti<sub>5</sub>O<sub>12</sub> (space group  $Fd\bar{3}m$ ) is a fairly new alternative to replace graphite at the negative electrode.<sup>82-85</sup> The theoretical capacity is lower, 175 mAh/g, and the redox potential higher, 1.55 V vs. Li/Li<sup>+</sup>, when compared to graphite. The high potential of Li<sub>4</sub>Ti<sub>5</sub>O<sub>12</sub> prevents SEI-layer formation and risk of Li plating,<sup>86</sup> thus assuring high safety. On the other hand, the cell voltage and energy density decrease. During lithiation (charge), the Li<sub>4</sub>Ti<sub>5</sub>O<sub>12</sub> spinel structure is converted to rock-salt structured Li<sub>7</sub>Ti<sub>5</sub>O<sub>12</sub>, but the volume change related to the phase transformation is negligible (less than 0.1%).<sup>87,88</sup> The spinel and rock-salt structures are shown in Figure 1e. Long lifetime is expected for Li<sub>4</sub>Ti<sub>5</sub>O<sub>12</sub> as SEI-layer is not needed and the volume change upon lithiation/delithiation is extremely small.

### 1.3 Scope of the Present Thesis

The perspective of this work was to investigate Li-ion battery electrode materials, both already commercialized and novel alternatives, in terms of their use in large-scale battery packs. Especially the new demands set to the battery cells were considered: safety, lifetime, and adequate energy density.

In order to meet the lifetime requirements of new applications, the cycle aging of commercial cells was studied at different temperatures.<sup>III,89</sup> The detrimental effect of extreme temperatures on the graphite negative electrode was revealed, in terms of both lifetime and safety. For large-scale batteries, an alternative negative electrode, such as Li<sub>4</sub>Ti<sub>5</sub>O<sub>12</sub>, is needed. However, Li<sub>4</sub>Ti<sub>5</sub>O<sub>12</sub> significantly decreases the cell voltage and the achievable energy density, and thus a high-voltage positive electrode is required. The current oxide and spinel materials are not optimal due to structural stability issues, which restrict their performance, lifetime, and safety.

Creating safe and structurally stable high-voltage positive electrode materials would be a solution for compatible energy densities of Li<sub>4</sub>Ti<sub>5</sub>O<sub>12</sub> negative electrode based cells. Mixed Li(Fe<sub>1-y</sub>M<sub>y</sub>)PO<sub>4</sub> ( $M = \text{Co, Ni}$ ) materials were studied inside a wide compositional range ( $0 \leq y \leq 1$ ) as potential positive electrodes combining high safety with adequately high energy density.<sup>IV,V</sup> The mixed compositions show better electrochemical performance than their parent  $y = 1$  phases and on the other hand, a higher average potential as the  $y = 0$  composition. In addition to the electrochemical performance evaluation, the effect of substitution on the delithiation/lithiation characteristics and on the Fe local environment was investigated in order to understand the substitution-induced effects. Especially the different substitution schemes were compared to reveal reasons to the lack of reversible Ni<sup>2+</sup>/Ni<sup>3+</sup> redox couple ac-

tivity, as the Ni-substituted materials would be more environmentally friendly and cost-effective, and theoretically show even higher average potentials.

In order to avoid excess heating of the battery and thus safety risks and unnecessary lifetime decrease, knowledge of the cell heat generation is required. In this work, the influence of different electrode materials on the cell heat generation was investigated.<sup>1,11</sup> The reversible part of the heat generation is related to the Li arrangement in the electrode material lattices, and it was studied by potentiometrically measuring the entropy change ( $\Delta S$ ) at different states of charge (SOC). Specific SOC ranges of different electrode material combinations were shown to be unfavourable due to increased heat generation. Additionally, the influence of different delithiation/lithiation mechanisms on the  $\Delta S$  behaviour was evaluated.

## 2. Aging of Li-Ion Cells

The performance of Li-ion cells degrades both during operation and storage: the phenomenon is called aging and it is observed as capacity fade and resistance increase. For EV, HEV/PHEV, and ESS applications, the battery pack desired lifetime is much higher than for consumer electronics, due to the battery's high initial cost and long life of the application itself. To be able to develop and design cells with long enough lifetimes, the aging mechanisms have to be studied in detail. Furthermore, aging induced safety risks must be examined in order to ensure safe operation of the battery near the end of life, too.

Li-ion batteries are to be used at different ambient temperatures, both high and low, and thus the dependence of aging on temperature should be investigated. Especially for transportation applications, ability to operate at low temperatures is needed. On the other hand, due to an inevitable heat generation during operation, cells especially in the middle of a large-sized battery pack are exposed to elevated temperatures. Furthermore, large temperature gradients can exist even within a single cell,<sup>90</sup> and non-uniform aging in different parts of the same cell has been demonstrated.<sup>91</sup> The pressure build-up and heat dissipation depend on the cell construction (pouch, prismatic or cylindrical) and may affect the aging phenomena, for example the Li plating.<sup>92,93</sup>

The properties of the cell's electrode materials largely affect the observed aging mechanisms. Especially the formation of passivating films and dissolution of active material elements are highly chemistry specific and problematic for the cell lifetime. In addition, certain positive and negative electrode material properties decrease the cell lifetime when combined, whereas some chemistry combinations are expected to be very durable. In the following, the main cycle aging mechanisms and the related safety aspects at different temperatures are discussed. A special focus is on the graphite electrode, as it is still most widely used as negative electrode. Additionally, the promising  $\text{Li}_4\text{Ti}_5\text{O}_{12}$  and  $\text{LiFePO}_4$  materials are covered more extensively.

### 2.1 Typical Aging Mechanisms

Cell aging is observed both during cycling (charge or discharge condition) and storage: it results in capacity fade and resistance increase, decreasing the energy and power densities. Aging is generally accelerated by non-ambient, typically elevated, temperatures and by high current rates. In addition, cycling to a high charge cut-off voltage or storage at high state of charge (SOC) enhance aging. The cycle depth and location (cycling SOC range) have an effect, too.

Aging mechanisms of Li-ion batteries can be divided into chemical and mechanical factors. Possible chemical factors are side reactions, most importantly at the electrode-electrolyte interfaces, structural degradation, and loss of active electrode materials by dissolution.<sup>78,94,95</sup> Active material loss can also take place through mechanical degradation of the non-active cell components or the material itself. Volume variations in the active material lattice or surface film growth may cause coating cracking or electrical isolation. Furthermore, current collector corrosion and degradation of the conductive additive or binder material can lead to contact losses.<sup>78,79,96-98</sup>

The electrochemical characteristics measured for a full cell include both the positive and negative electrode contributions. Thus the numerous possible processes leading to cell aging are difficult to distinguish from each other. Cell disassembly and post-mortem analysis are important tools for discovering the chemical and mechanical origins behind the cell degradation.

## 2.2 Determining Aging Mechanisms by Post-Mortem Analysis

In the post-mortem analysis, several analysis methods can be used to examine the electrode samples at different probing depths (bulk methods *versus* surface sensitive methods). For receiving structural and morphology information from the bulk, X-ray diffraction spectroscopy (XRD), scanning electron microscopy (SEM), Raman spectroscopy, and X-ray absorption spectroscopy (XAS) are used, for example. XRD can reveal possible phase changes in the active materials or structural degradation,<sup>97</sup> but it is insensitive to lighter elements, amorphous components, and trace amounts (~2% detection limit). SEM imaging gives information on the particle morphology (particle size, possible cracking *etc.*), and it can also indicate surface film formation.<sup>92,97,99-101</sup> Raman spectroscopy measures the structural ordering. It is used to analyze the degree of disorder in graphite electrodes or graphitic conductive additives,<sup>97</sup> or to track phase transitions (crystal symmetry changes).<sup>102</sup> XAS provides element-specific information on the local environment (oxidation state or changes in the bonding).<sup>97</sup>

To probe the formation and compositions of the thin surface films on electrodes (especially graphite's SEI-layer), X-ray photoelectron spectroscopy (XPS), infrared spectroscopy (IR), and Raman spectroscopy can be utilized, for instance. With XPS, information on the chemical structure and composition of the surface film is achieved.<sup>103-106</sup> IR and Raman methods are used to detect different bonds and thus possible compounds in the surface films.

Energy dispersive X-ray spectroscopy (EDS) and inductively coupled plasma spectroscopy (ICP) methods are employed to track the elemental compositions. With ICP, even trace amounts can be detected,<sup>92,97</sup> whereas EDS analysis can be used for elemental mapping, but its sensitivity especially for lighter elements is limited.

The electrochemical performance of the positive and negative electrodes can be estimated separately by testing electrode samples, collected from the disassembled cells, in half-cells. In the half-cell configuration, Li-metal is used as the counter electrode (unlimited Li source). For example, loss of active material due to exfoliation or electrical isolation can be determined. Furthermore, the full cell resistance can be

divided into positive and negative electrode contributions, and hence the surface layer and charge transfer resistances can be separated. However, special care needs to be taken during the test cell preparation: in general, only one-sided electrode coatings can be tested in half-cells, which means that the other side of the double-sided composite electrode has to be dissolved to reveal the bare current collector.

Visual inspection is an important part especially for graphite negative electrodes. The different lithiation states of graphite show different colors. The pristine black-grey color of graphite is changed upon Li intercalation through dark blue to red for the stage-2 ( $\text{LiC}_{12}$ ) phase and finally to golden yellow for the fully-lithiated stage-1 ( $\text{LiC}_6$ ) compound.<sup>107,108</sup> Thus color differences can give valuable information on the uniformity of the delithiation state: if cells are disassembled at higher SOC, possible inactive areas can be detected as non-uniform color. Furthermore, Li trapped in the graphite lattice due to contact losses could be revealed, too. Metallic Li plating on the graphite negative electrode can be observed as a silver or silvergrey colored uniform layer,<sup>93,109</sup> as more local metallic stains,<sup>91</sup> or even as dendritic grains.<sup>III</sup> The plated Li reacts vigorously with water generating hydrogen.<sup>93,109,III</sup> Visual inspection of the separator can reveal signs of detached surface films or Li deposits. Also the amount of free electrolyte can be judged, and the electrode thicknesses can be measured in order to estimate surface layer growth.

A major challenge in the post-mortem analysis is the air- and moisture-sensitivity of the electrodes, especially lithiated graphite electrode and plated Li. Changes in the SEI-layer composition and LiOH formation have been observed during air and moisture exposure of lithiated graphite.<sup>103</sup> As a consequence, the graphite surface is partially delithiated. In air, plated Li is suggested to first form  $\text{Li}_2\text{O}$ , and then be further converted to LiOH and finally to  $\text{Li}_2\text{CO}_3$  by reaction with moisture and  $\text{CO}_2$ .<sup>93</sup> As the samples are often analyzed, or at least transferred, in humid air atmosphere, these reactions must be taken into account upon results interpretation. *Prior* to characterization, the electrode samples are rinsed typically with dimethyl carbonate (DMC) to remove the electrolyte salt  $\text{LiPF}_6$  residues, as  $\text{LiPF}_6$  decomposes creating HF in contact with moisture or other impurities. However, upon rinsing the samples, some surface films may possibly be removed, and the samples' air-sensitivity may change.<sup>103</sup>

## 2.3 Effect of Electrode Materials

In general, Li-ion cell aging originates from the graphite negative electrode, and it is mainly related to the graphite SEI-layer degradation and growth reactions.<sup>94,96,110–112</sup> SEI-layer is initially formed because the graphite electrode potential is outside the electrolyte's stability window, and thus the electrolyte is reduced on the graphite electrode surface. In proper electrolytes, the reduction reaction products passivate the graphite surface. When the cell is cycled, the graphite electrode is exposed to a constant volume change. As a consequence, even a highly stable and protective SEI-layer will undergo minor cracking and decomposition.<sup>96,111–113</sup> This results in layer reformation and growth, until an electronically insulating composition is reached. Presence of HF due to  $\text{LiPF}_6$  decomposition will destabilize the SEI-layer and lead to highly resistive LiF formation.<sup>113,114</sup> In the SEI-layer reformation reactions, active Li

is consumed and capacity fade is thus accelerated. Furthermore, due to growth and structural changes, the SEI-layer resistance and further the cell's impedance increase. Gaseous components are produced inside the cell in the SEI-forming reactions.<sup>79,115</sup> A thick SEI-layer can decrease graphite's accessible surface area and cause contact losses, and eventually even partially penetrate to the separator, clogging its pores.<sup>78,96</sup>

Another aging and especially safety related issue of graphite negative electrode is the Li plating phenomenon. During cell charging, Li can deposit as metallic on the graphite surface instead of intercalating into the graphite lattice. This Li plating takes place if the graphite electrode potential is forced below 0 V vs. Li/Li<sup>+</sup> due to high polarization or by mass transport limitation (graphite surface gets saturated because of slow Li diffusion).<sup>78–80,93,109,116,117</sup> These conditions are usually met at low-temperature charging or at charging with high currents,<sup>81,93,117–119</sup> but they can be also produced by an inhomogeneous current or potential distribution.<sup>78,96</sup> The graphite's SEI-layer characteristics can affect the intercalation kinetics and thus enhance the plating condition.<sup>119,120</sup> Li plating is also promoted by poor cell balancing (too high positive-to-negative electrode ratio) or geometric misfits (negative electrode geometrically smaller than the positive)<sup>78,80,81,93,119,120</sup> and by a large graphite particle size.<sup>80</sup> The formation of metallic Li depositions consumes active lithium, decreases the coulombic efficiency, and leads to capacity fade. Furthermore, the metallic Li forms a SEI-layer when in contact with the electrolyte. Thus the graphite electrode resistance is increased and additional electrolyte is consumed.

For the Li<sub>4</sub>Ti<sub>5</sub>O<sub>12</sub> negative electrode, no SEI-layer is needed due to its higher redox potential, and the volume change upon Li insertion/extraction is insignificant. Furthermore, no Li plating takes place. These properties predict a minimal aging rate for Li<sub>4</sub>Ti<sub>5</sub>O<sub>12</sub>, and extremely long cycle lives have been demonstrated.<sup>41,121,122</sup> Nevertheless, significant gas evolution (mainly H<sub>2</sub>, CO<sub>2</sub>, and CO) and consequential cell swelling have been reported in several studies for Li<sub>4</sub>Ti<sub>5</sub>O<sub>12</sub> electrodes.<sup>123–127</sup> A related capacity fade has been observed, too. Water reduction to H<sub>2</sub> at the Li<sub>4</sub>Ti<sub>5</sub>O<sub>12</sub> electrode was suggested as a possible gas evolution mechanism, due to moisture contamination from improperly dried materials or from the cell assembly.<sup>123,124</sup> This reaction was proposed to further lead to CO<sub>2</sub> evolution and Li-alkyl-carbonate surface film deposition on the Li<sub>4</sub>Ti<sub>5</sub>O<sub>12</sub> electrode.<sup>124</sup> Differences in the cell assembly process can significantly affect the cell's moisture content and possibly explain the discrepancies between different studies. However, also an interfacial reaction between the Li<sub>4</sub>Ti<sub>5</sub>O<sub>12</sub> surface and the alkyl carbonate electrolyte solvents has been suggested,<sup>127</sup> leading to similar gas evolution. Surface films comprising of organic species<sup>128</sup> or inorganic LiPF<sub>6</sub> decomposition products<sup>123,129</sup> have been reported, too.

For positive electrode materials, structural changes, metal dissolution, chemical decomposition, and surface modification are the main aging mechanisms.<sup>78,79,94,95</sup> For LiCoO<sub>2</sub>-, LiNiO<sub>2</sub>-, and LiMn<sub>2</sub>O<sub>4</sub>-based materials, undesirable phase transitions can take place at high SOCs and in over-charge conditions, leading to structure degradation.<sup>95</sup> LiMn<sub>2</sub>O<sub>4</sub> is prone to structural changes also at the over-discharged state, due to Jahn-Teller distortion of Mn<sup>3+</sup>.<sup>38</sup> The Mn<sup>4+</sup> in Li(Ni,Co,Mn)O<sub>2</sub> is more stable, but structural changes at the particle surfaces have still been observed, resulting in degradation of the Li migration tunnels.<sup>30,130</sup> Phase transitions or structural disorder-

dering can cause increased volume changes upon Li insertion/extraction, thus promoting contact losses. For  $\text{LiFePO}_4$ , no cycling induced structural changes are predicted.<sup>91,131,132</sup>

Due to metal dissolution, the active positive electrode material is lost, but more importantly, the metal ions migrate to the graphite negative electrode: they are reduced at the low potential and incorporated in the graphite's SEI-layer, leading to increased layer growth and resistance increase.<sup>78,94,96,133</sup> The metal dissolution is accelerated by elevated temperatures, high SOC, and HF in moisture or impurity contaminated electrolyte.<sup>78,79,95,134</sup> Especially the Mn dissolution from  $\text{LiMn}_2\text{O}_4$  is significant.<sup>78,95,133,135</sup> For  $\text{Li}(\text{Ni},\text{Co},\text{Mn})\text{O}_2$ , in addition to Mn, also Co and Ni dissolution has been detected.<sup>99,134</sup> Fe dissolution from  $\text{LiFePO}_4$  has also been reported: it is related to HF contamination of the electrolyte and accelerated at elevated temperatures.<sup>102,136–138</sup> The phenomenon is attributed to HF attacking the  $\text{LiFePO}_4$  surface, and it is suggested to lead to formation of a resistive surface film, which comprises of  $\text{LiPF}_6$  decomposition products.<sup>102</sup> According to Wang *et al.*,<sup>136,137</sup> Fe-containing impurity phases in the  $\text{LiFePO}_4$  active material are especially susceptible to be attacked by HF, resulting in higher Fe dissolution rates. Carbon coating has been observed to stabilize the  $\text{LiFePO}_4$  surface to some extent.<sup>137</sup>

For the high-voltage oxide positive electrodes, surface film formation has been proposed to take place, promoted by high SOC.<sup>95,104,105,112,114,139–141</sup> However, the film character is suggested to be different from graphite's SEI-layer, having less passivating character;<sup>104</sup> only a slight film growth has been observed to take place during cycling.<sup>105</sup> For  $\text{LiFePO}_4$ , no significant surface film due to electrolyte oxidation products is predicted.<sup>104</sup>

## 2.4 Effect of Temperature

Different aging mechanisms take over at non-ambient temperatures. Typically, aging is faster at elevated cycling or storage temperature,<sup>92,110,142,III</sup> as all parasitic reactions are accelerated. However, for cells with graphite negative electrode,<sup>92,93,143</sup> also cycling at low temperatures can accelerate aging. The cycle aging rate of  $\text{Li}(\text{Ni},\text{Mn},\text{Co})\text{O}_2\text{-LiMn}_2\text{O}_4/\text{C}$  cell chemistry was found to be at its minimum at +25 °C temperature; both higher and lower temperatures were demonstrated to accelerate the performance degradation.<sup>92</sup>

### 2.4.1 Aging at High Temperatures

At elevated temperatures, the accelerated graphite SEI-layer degradation and decomposition is the major aging factor.<sup>78,113,144</sup> Partial dissolution and structural changes, resulting in increased amount of inorganic, higher resistance components (for example LiF), take place. Decomposition of the SEI-layer is predicted at temperatures above +60 °C. Especially the metal dissolution from the positive electrode, increased at elevated temperatures, is detrimental for the SEI-layer. Due to the layer degradation, capacity fade and resistance increase are accelerated, and more gaseous products are formed. Also Li plating has been observed as a consequence of prolonged cycling at room temperature or higher,<sup>91,96,145,III</sup> although it is generally pre-

dicted for low temperatures and high-rate charging. The Li plating will be discussed in Chapter 2.4.3 in more detail.

For  $\text{Li}_4\text{Ti}_5\text{O}_{12}$  electrodes, the gas evolution problem has been observed to be promoted by elevated temperatures.<sup>126</sup> Due to its high potential and lack of passivating SEI-layer,  $\text{Li}_4\text{Ti}_5\text{O}_{12}$  is not predicted to be sensitive to positive electrode metal dissolution.<sup>121</sup> However, some studies have detected Mn traces on the  $\text{Li}_4\text{Ti}_5\text{O}_{12}$  electrodes of cycle aged,  $\text{LiMn}_2\text{O}_4$ -positive electrode containing cells.<sup>123,125</sup> For positive electrodes, in addition to the increased metal dissolution, surface film formation is generally promoted at elevated temperatures.<sup>78,79,95,134</sup> Phase transitions can be accelerated, too.<sup>95</sup>

In the present work, cycle aging of commercial, pouch-type  $\text{Li}(\text{Ni},\text{Mn},\text{Co})\text{O}_2/\text{graphite}$  cells (40 Ah rated capacity) was studied.<sup>III</sup> Cycle aging was performed at three different temperature conditions: (i) room temperature, (ii) +45 °C charge/+45 °C discharge, and (iii) +45 °C charge/+65 °C discharge. For the +45 °C/+65 °C condition, a prolonged cycling to 50% capacity fade was carried out, in order to emphasize the aging phenomena produced by the extreme aging conditions. The capacity fade with cycling and the cell impedance at different capacity fade conditions are shown in Figure 2. In the impedance spectra, the electrodes' polarization resistance was reflected as two partly overlapping semi-circles, one at higher and one at lower frequencies. The cell impedance growth has been attributed to increasing positive electrode charge transfer resistance,<sup>97,99</sup> seen as the lower frequency semi-circle growth upon cycling. The higher frequency semi-circle has been related to the graphite electrode and its SEI-layer resistance.<sup>101,146</sup>

Increasing the cycling temperature from room temperature to +45 °C decreased the cycle life by over 20%. As the discharge temperature was further elevated to +65 °C, the capacity fade was accelerated, and 80% of rated capacity was reached already after 800 cycles (70% decrease in cycle life). In general, the graphite electrode SEI-layer growth has been identified as the main capacity fade origin for  $\text{Li}(\text{Ni},\text{Mn},\text{Co})\text{O}_2(-\text{LiMn}_2\text{O}_4)/\text{graphite}$  cells.<sup>92,99,147</sup> In many cases, it has been accelerated by metal dissolution at the positive electrode. Based on post-mortem analysis,<sup>III</sup> the cell capacity fade at room temperature was attributed in the present work to the SEI-layer growth at the graphite negative electrode. No obvious morphology or structure changes in the electrode bulks were detected. It was observed that the polarization resistance ( $R_{\text{pol}}$ ) evolution was very similar at room temperature and at +45 °C (Figure 2b), implying that the phenomena leading to electrodes' resistance growth were not significantly altered by this temperature increase.

However, for the elevated discharge temperature (+45 °C/+65 °C condition), clearly faster capacity fade and increased electrodes' polarization resistance were demonstrated already at 80%, but especially at 50% capacity fade (Figure 2).<sup>III</sup> The growth of both semi-circle resistances was observed to be accelerated at this elevated temperature condition. Especially the higher frequency semi-circle, related to the graphite's SEI-layer, became clearly visible. Indeed, in post-mortem analysis, a highly resistive LiF was detected on the graphite electrode by XRD, and fast SEI-layer degradation is predicted due to the high +65 °C temperature. Mechanical coating degradation was observed for the  $\text{Li}(\text{Ni},\text{Mn},\text{Co})\text{O}_2$  electrode, possibly due to binder material decomposition. This can at least partly explain the low frequency resistance

growth. No metals from the  $\text{Li}(\text{Ni},\text{Mn},\text{Co})\text{O}_2$  electrode were discovered at the graphite electrode, but the sample preparation (DMC rinsing) may have removed some surface layers. For the cell cycled at  $+45\text{ }^\circ\text{C}$ , some cycling-induced Li plating was observed. Further for the  $+45\text{ }^\circ\text{C}/+65\text{ }^\circ\text{C}$  condition, a drastically increased amount of Li depositions was detected. The promoted Li plating is concluded as the additional capacity fade origin at elevated temperatures. Interestingly, the ohmic resistance ( $R_\Omega$ ) at 80% shows a clear dependence on the cycling temperature.

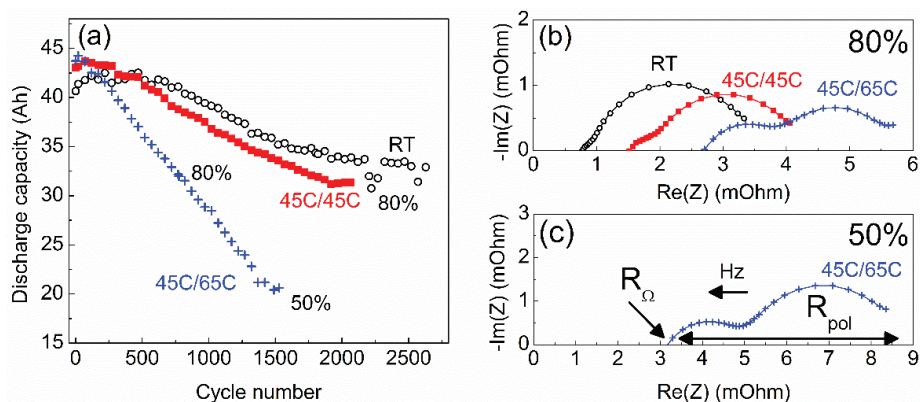


**Figure 2.** Cycle aging of commercial 40 Ah  $\text{Li}(\text{Ni},\text{Co},\text{Mn})\text{O}_2/\text{graphite}$  pouch-cells at different temperature conditions: room temperature (RT),  $+45\text{ }^\circ\text{C}$  charge/ $+45\text{ }^\circ\text{C}$  discharge (45C/45C), and  $+45\text{ }^\circ\text{C}$  charge/ $+65\text{ }^\circ\text{C}$  discharge (45C/65C).<sup>111</sup> (a) Capacity fade with cycle number; (b) cell impedance at 80% and (c) at 50% of rated capacity. The different  $\text{Re}(Z)$  axis scales between (b) and (c) is to be noticed.

#### 2.4.2 Aging at Low Temperatures

During cycling at temperatures below  $0\text{ }^\circ\text{C}$ , again the graphite negative electrode is the main origin of aging. Rather than decreased electrolyte conductivity, the slow Li diffusion in the graphite electrode is the rate limiting factor for low temperature charging,<sup>143</sup> and the resulting Li plating on graphite electrode is the main aging mechanism. Charging at temperatures below  $0\text{ }^\circ\text{C}$  is not recommended,<sup>81</sup> and a significant amount of Li is plated due to charging at  $-20\text{ }^\circ\text{C}$  temperature with 0.2C current,<sup>143,148</sup> for example. The Li plating phenomenon will be discussed more in Chapter 2.4.3.

In addition, the slow Li diffusion in graphite can result in significant concentration gradients inside the graphite particles. As the Li insertion/extraction causes a noticeable volume change, the concentration gradients can lead to diffusion-induced stress and eventually graphite particle cracking.<sup>149,150</sup> The crack formation is significantly accelerated by low temperatures (slow diffusion) and high current rates, and it also depends on the graphite particle size.<sup>149–151</sup> In the study of Takahashi *et al.*,<sup>149</sup> graphite particle cracking after 100 cycles at  $-10\text{ }^\circ\text{C}$  temperature (10C current rate) was confirmed. In the present work,<sup>89</sup> a surprisingly good rate capability performance was observed in half-cell testing of graphite electrodes, which were disassembled from a low-temperature ( $-18\text{ }^\circ\text{C}$ ) cycled commercial  $\text{LiFePO}_4/\text{graphite}$  cell.<sup>152</sup> In the cell disassembly, the graphite electrodes were observed to be covered with a uniform layer of plated Li. However, in the subsequent electrochemical testing, a relatively better performance was demonstrated than for graphite electrodes disassem-

bled from a fresh reference cell. It is speculated that the enhanced performance could be due to an increased graphite particle surface area. This increase may be caused by graphite particle cracking during the low-temperature cycling. In SEM analysis, signs of crack formation and a broadened particle size distribution, with more smaller particles possibly due to the cracking, were observed for the  $-18\text{ }^{\circ}\text{C}$  cycled graphite electrode, when compared to the fresh reference cell. SEM images of the graphite electrodes are presented in Figure 3.

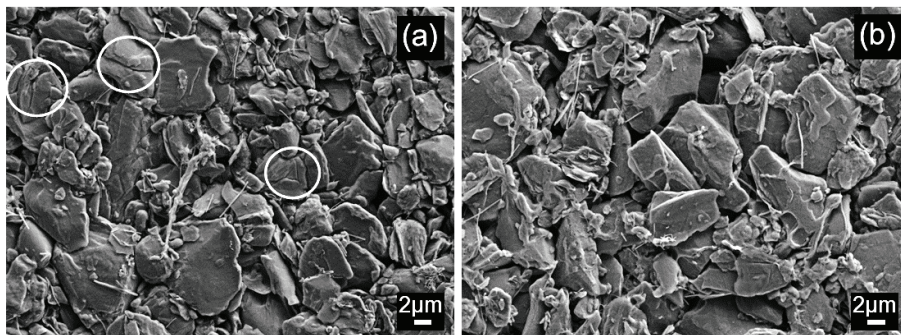


**Figure 3.** SEM images of graphite electrodes disassembled from  $\text{LiFePO}_4/\text{graphite}$  cells.<sup>89</sup> (a)  $-18\text{ }^{\circ}\text{C}$  cycled cell (examples of crack formation indicated), (b) fresh reference cell. Due to sample preparation, surface deposits are seen on the graphite particles.

For  $\text{Li}_4\text{Ti}_5\text{O}_{12}$ , an excellent low-temperature behaviour is expected,<sup>153–156</sup> and the performance is more limited by the electrolyte conductivity. For positive electrodes, the metal dissolution and surface film formation are suppressed at low temperatures, and no special low-temperature related aging phenomena have been suggested.<sup>154,156–158</sup>

#### 2.4.3 Comparison of Li Plating at Different Temperatures

The factors leading to Li plating and also the resulting plating morphology are different depending on the temperature. At higher temperatures, Li diffusion is faster and thus higher charge currents or otherwise high graphite electrode polarization due to inhomogeneous current/potential distribution are needed to induce the Li plating condition. Li can deposit either in a reversible or irreversible manner:<sup>93,109</sup> reversible plating retains electrical contact with the graphite electrode, whereas irreversible plating can easily lose its contact with the graphite electrode and become isolated, irreversibly lost dead Li.

At low temperatures, usually a flat and uniform layer of plated Li is observed, with no dendrite formation.<sup>93,109</sup> This kind of Li plating is expected to have a low surface area, accompanied with only moderate SEI-layer formation and high reversibility for the plating. The reversibly plated Li can be at least partly recovered to active, cyclable Li. The Li deposition can be oxidized in a subsequent discharge cycle before the actual Li deintercalation,<sup>93,109,119,120,148</sup> detected as an initial high-voltage plateau in the cycling curve. It can also intercalate into the graphite lattice during a rest period.<sup>143,148</sup> On the contrary, at higher temperatures, Li plating takes place as more local spots, with dendritic, mossy nature, producing high surface area Li plating.<sup>93,96,III</sup>

This kind of Li plating is more prone to be irreversible; it results in increased amount of SEI-layer formation on the deposition, and it is easily exfoliated from the graphite electrode surface.<sup>93,III</sup>

In the present study, signs of minor Li plating were observed already in a non-cycled, fresh cell.<sup>III</sup> This is anticipated to be due to gas bubbles, produced in the initial SEI-layer formation during the formation cycles.<sup>79,115</sup> The later movement of such gas can reveal unexploited positive electrode. This may lead to inhomogeneous current and potential distributions (increased current density for certain spots) and thus to Li plating instead of intercalation. Especially after prolonged cycling at the elevated +45 °C/+65 °C temperature, a significant increase in the amount of Li plating was observed.<sup>III</sup> It has been suggested that excessive SEI-layer formation can lead to clogging of the graphite negative electrode pores, which decreases the accessible surface area and thus introduces a higher current rate to the remaining active areas.<sup>96</sup> This can lead to a Li plating condition. Furthermore, a thick and highly resistive SEI-layer can increase the graphite electrode polarization and thus promote Li plating.<sup>109</sup> Based on the present work,<sup>III</sup> an additional, Li plating accelerating scenario is suggested for prolonged cycling at elevated temperatures. Due to increased degradation and growth of the graphite electrode's SEI-layer, electrolyte consumption is accelerated, and lots of gaseous components are formed. At the same time, at high temperatures, the solubility of gases decreases, and thus an increased amount of gaseous components are present in the cell. Gas between the electrodes and the lack of electrolyte may disturb the current and potential distributions, thus promoting the Li plating condition. The plated Li further reacts with the electrolyte, whereby more electrolyte is consumed and more gas produced. On the contrary, Li plating at low temperatures has been suggested to be self-inhibiting due to loss of cyclable Li, which changes the electrodes' capacity balance.<sup>93</sup> As a consequence, high graphite electrode lithiation states, at which Li plating is more prone to take place, are no longer favoured.

In the present work, the cell's ohmic resistance was observed to increase with increasing amount of Li plating.<sup>III</sup> The ohmic resistance evolution is depicted in Figure 4. Lack of electrolyte and possible clogging of the separator pores are anticipated as the main origins of ohmic resistance growth. In the post-mortem analysis, adhered depositions were observed in the separators of the +45 °C and +45 °C/+65 °C cycled cells. The depositions were attributed to the plated Li and its SEI-layer, as they were at the same locations than Li plating at the corresponding graphite electrodes.

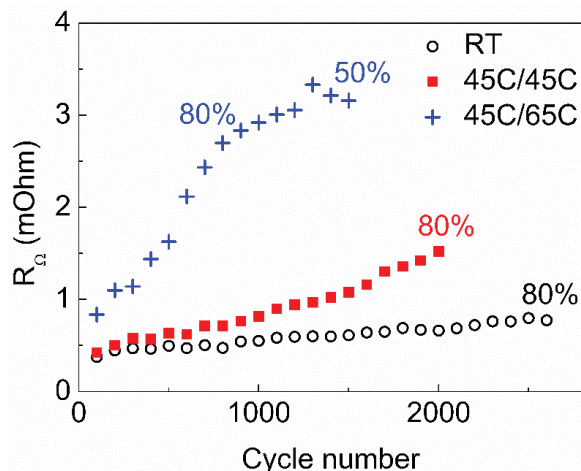


**Figure 4.** Ohmic resistance evolution in commercial 40 Ah Li(Ni,Co,Mn)O<sub>2</sub>/graphite pouch-cells during cycling at different temperature conditions: room temperature (RT), +45 °C charge/+45 °C discharge (45C/45C), and +45 °C charge/+65 °C discharge(45C/65C).<sup>III</sup> The state of capacity fade (80%/50% of rated capacity) is indicated.

Based on the present work,<sup>III</sup> it is concluded that a post-mortem study is needed to unambiguously detect irreversible Li plating. As no electrical contact to the graphite electrode is retained, no irreversibly plated Li is expected to be oxidized during the subsequent discharge cycle and thus no characteristic high-voltage plateau is produced. To follow the graphite negative electrode potential and possible polarization below 0 V vs. Li/Li<sup>+</sup>, a separate reference electrode, mounted inside the cell, would be needed. The cell's coulombic efficiency could be tracked, but it is additionally affected by other side reactions, such as the graphite electrode SEI-layer reactions. A suddenly accelerated capacity fade and resistance increase,<sup>96</sup> or a sudden capacity drop<sup>159</sup> have been suggested as signs of Li plating. Yet in the present work, no such behaviour was observed (Figures 2 and 4).<sup>III</sup> In addition, cell thickness measurement has been proposed for Li plating diagnosis.<sup>93,160</sup> The method was claimed to take into account gas formation, but the procedure was demonstrated only for reasonably uniform low-temperature Li plating.<sup>160</sup> Thus its accuracy and applicability for localized, dendritic Li depositions is unproved. Additionally, Li plating has been tracked by *in-situ* neutron diffraction,<sup>148</sup> but such a measurement needs special arrangements and equipment.

### 3. $\text{Li}(\text{Fe}_{1-y}\text{M}_y)\text{PO}_4$ ( $M = \text{Mn}, \text{Co}, \text{Ni}$ ) Positive Electrodes

As can be concluded based on Chapter 2, the graphite negative electrode is usually the limiting factor in terms of cell lifetime and also safety, both during low and high temperature operation.  $\text{Li}_4\text{Ti}_5\text{O}_{12}$ , however, is intrinsically more suitable for safe operation also at extreme temperatures and for achieving long lifetimes, especially if the gas evolution problem can be solved. As a positive electrode,  $\text{LiFePO}_4$  is a promising alternative to be paired with  $\text{Li}_4\text{Ti}_5\text{O}_{12}$ , because it is also safe and stable upon cycling.

To date,  $\text{LiFePO}_4$  is the only material of the  $\text{LiMPO}_4$  metal phosphate group in commercial use. However, when combined with  $\text{Li}_4\text{Ti}_5\text{O}_{12}$ , the cell voltage and thus energy density are very low for transportation purposes. Higher voltage positive electrode materials with the same intrinsically safe structural properties would be more beneficial. The lack of sufficient electrochemical performance restricts the use of high-voltage metal phosphates ( $\text{LiMnPO}_4$ ,  $\text{LiCoPO}_4$ , and  $\text{LiNiPO}_4$ ). However, creating mixed  $\text{Li}(\text{Fe}_{1-y}\text{M}_y)\text{PO}_4$  ( $M = \text{Mn}, \text{Co}, \text{Ni}$ ) solid-solutions could offer improved performance whilst remaining the stable and safe olivine structure. Mixed compositions of  $\text{Li}(\text{Co},\text{Mn})\text{PO}_4$ <sup>161</sup> or  $\text{Li}(\text{Co},\text{Ni})\text{PO}_4$ <sup>69,161</sup> have been investigated, too, but the Fe in structure seems to be crucial for the conductivity properties.<sup>69,72</sup> Also multi-component systems with ternary<sup>162,163</sup> and even quaternary<sup>164</sup> transition metal compositions have been studied.

So far, most of the studies have focused on  $\text{Li}(\text{Fe}_{1-y}\text{Mn}_y)\text{PO}_4$  materials, and promising results have been achieved for  $\text{Li}(\text{Fe}_{0.2}\text{Mn}_{0.8})\text{PO}_4/\text{Li}_4\text{Ti}_5\text{O}_{12}$  test cells.<sup>129,165</sup> However, when a ternary  $\text{Li}(\text{Fe}_{1/3}\text{Mn}_{1/3}\text{Co}_{1/3})\text{PO}_4$  material was tested,<sup>163</sup> the  $\text{Mn}^{2+}/\text{Mn}^{3+}$  redox couple performance was characterized by an exceptionally large polarization (compared to the  $\text{Fe}^{2+}/\text{Fe}^{3+}$  and  $\text{Co}^{2+}/\text{Co}^{3+}$  redox regions). This was attributed to the intrinsically slow polaronic conduction of the Jahn-Teller distorted  $\text{Mn}^{3+}$ . The Mn-substituted materials were proposed to ultimately suffer from a similar issue,<sup>163</sup> which can potentially restrict their electrochemical performance and use in Li-ion batteries.

In the present thesis, Co- and Ni-substituted materials were studied.<sup>IV,V</sup> These systems would theoretically yield higher average potentials compared to the Mn-substituted system. In addition, the purpose was to compare the different substitution schemes at a wide compositional range in order to increase knowledge of the substitution-induced effects. In the following, mixed  $\text{Li}(\text{Fe}_{1-y}\text{M}_y)\text{PO}_4$  ( $M = \text{Mn}, \text{Co}, \text{Ni}$ ) materials are considered in terms of their structure, electrochemical performance, and delithiation/lithiation characteristics.

### 3.1 Isovalent Substitution at the Fe Site

The Li(Fe<sub>1-y</sub>M<sub>y</sub>)PO<sub>4</sub> phosphate structure is composed of LiO<sub>6</sub> and (Fe/M)O<sub>6</sub> octahedra and PO<sub>4</sub> tetrahedra. Substitution takes place at the Fe site, so that the Li atoms occupy the M1 site and the Fe/M atoms the M2 site. One (Fe/M)O<sub>6</sub> octahedron shares corners with four other (Fe/M)O<sub>6</sub> octahedra and edges with two LiO<sub>6</sub> octahedra.<sup>40,166</sup> Li-ion diffusion takes place in one-dimensional channels along the b axis.<sup>167,168</sup> The orthorhombic olivine structure of a mixed Li(Fe<sub>1-y</sub>M<sub>y</sub>)PO<sub>4</sub> (M = Mn, Co, Ni) phosphate is presented in Figure 5.

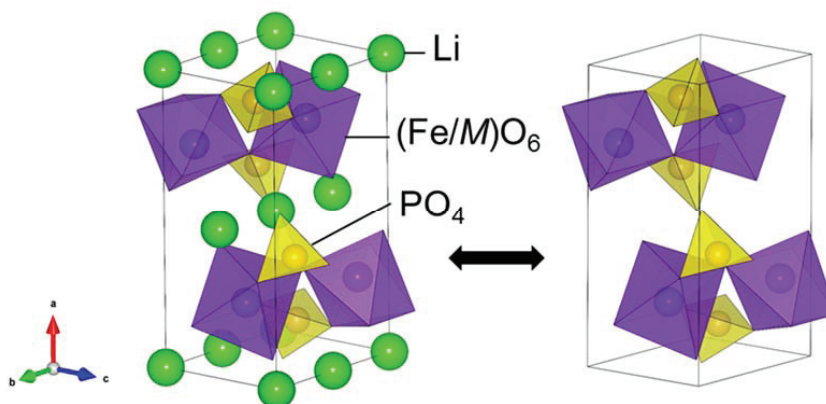


**Figure 5.** Schematic structure of the orthorhombic olivine Li(Fe<sub>1-y</sub>M<sub>y</sub>)PO<sub>4</sub> (M = Mn, Co, Ni) in lithiated (left) and delithiated (right) states (image produced by Vesta).<sup>169</sup>

At low substitution levels ( $y \leq 0.1$ ), isovalent or aliovalent substitution at the Fe (M2) site is employed in order to enhance the conductivity properties by creating mixed-valence states.<sup>170–172</sup> At the higher substitution levels ( $y > 0.1$ ), isovalent substitution with  $M = \text{Mn, Co, or Ni}$  aims for a higher average potential and thus for an increased cell voltage and energy density. For  $M = \text{Mn}$ <sup>46,71,173–175</sup> and  $\text{Co}$ <sup>63,71,176, V</sup>, the  $M$  atom has been shown to react at its own higher-voltage plateau  $M^{2+}/M^{3+}$ . These features are illustrated in Figure 6, where a schematic discharge curve for a Li(Fe<sub>0.4</sub>Co<sub>0.6</sub>)PO<sub>4</sub> material and the theoretical energy density (mWh/g) for different substitution schemes of Li(Fe<sub>1-y</sub>M<sub>y</sub>)PO<sub>4</sub> (M = Mn, Co, Ni) are presented.

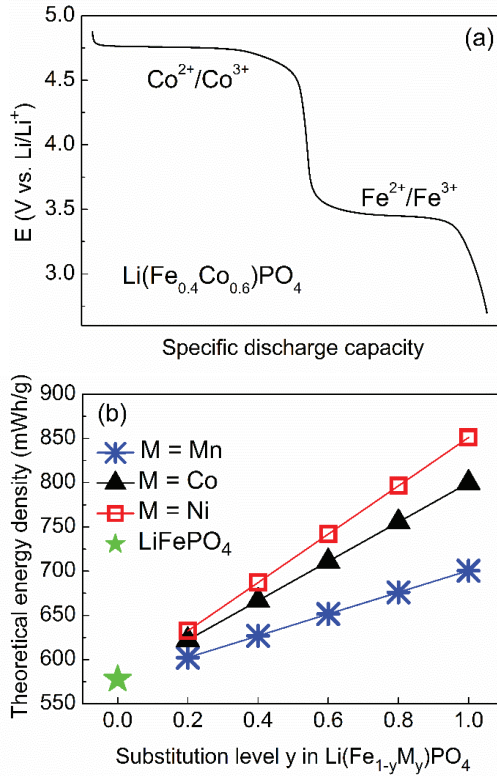


**Figure 6.** (a) Schematic discharge curve for a mixed  $\text{Li}(\text{Fe}_{0.4}\text{Co}_{0.6})\text{PO}_4$  material; (b) the theoretical energy density of  $\text{Li}(\text{Fe}_{1-y}\text{M}_y)\text{PO}_4$  ( $M = \text{Mn}, \text{Co}, \text{Ni}$ ) materials at different  $y$ . The energy densities are calculated based on theoretical specific capacities and redox potentials (3.4 V vs.  $\text{Li}/\text{Li}^+$  for  $\text{Fe}^{2+}/\text{Fe}^{3+}$ , 4.1 V for  $\text{Mn}^{2+}/\text{Mn}^{3+}$ , 4.8 V for  $\text{Co}^{2+}/\text{Co}^{3+}$ , and 5.1 V for  $\text{Ni}^{2+}/\text{Ni}^{3+}$ ).

The ionic radii and the  $d$ -electron configurations for the high-spin, 6-coordinated  $(\text{Fe}/M)^{2+}$  and  $(\text{Fe}/M)^{3+}$  valence states are presented in Table 2. In addition, the predicted Jahn-Teller activity is indicated.

**Table 2.** Ionic radius,  $^{177}$   $d$ -electron configuration, and predicted Jahn-Teller effects of  $M^{2+}$  and  $M^{3+}$  ( $M = \text{Mn}, \text{Fe}, \text{Co}, \text{Ni}$ ) in high-spin 6-coordinated states.

$M$	ionic radius ( $M^{2+}$ ), Å	$M^{2+}$ $d$ -electron configuration	Jahn-Teller effect	ionic radius ( $M^{3+}$ ), Å	$M^{3+}$ $d$ -electron configuration	Jahn-Teller effect
Mn	0.830	$d^5$	-	0.645	$d^4$	strong
Fe	0.780	$d^6$	weak	0.645	$d^5$	-
Co	0.745	$d^7$	weak	0.61	$d^6$	weak
Ni	0.690	$d^8$	-	0.60	$d^7$	weak

### 3.1.1 Effect on Lattice Parameters

In XRD, the solid-solution formation is observed as a continuous shift of diffraction peaks with the changing lattice parameters, according to Vegard's law. The lattice parameter evolution in the solid-solution series of  $\text{Li}(\text{Fe}_{1-y}\text{M}_y)\text{PO}_4$  ( $M = \text{Mn},^{175} \text{Co},^{\text{IV}} \text{Ni}^{\text{IV}}$ ) is presented in Figure 7. Additionally, the product  $a * c$  is depicted, estimating the Li diffusion channel area.<sup>63,168</sup>

According to Figure 7, the lattice parameters show different dependencies on the  $M^{2+}$  ionic radius. For the larger-sized Mn substituent, all the lattice parameters,  $a$ ,  $b$ , and  $c$ , increase with increasing  $y$ ,<sup>175,178</sup> thus resulting in isotropic unit cell volume increase. For both Co and Ni substitution schemes (smaller-sized  $M^{2+}$ ), the  $a$  and  $b$  lattice parameters were observed to decrease.<sup>IV</sup> However, although the  $c$  parameter slightly decreased for the smaller Ni substituent, a minor increase was shown for the Co-substituted system,<sup>IV</sup> in spite of  $\text{Co}^{2+}$  being smaller than  $\text{Fe}^{2+}$ . Furthermore, changes in the  $c$  parameter are overall more subtle compared to those of  $a$  and  $b$  parameters.

In the  $a$  direction, the olivine structure can be considered as  $\text{MO}_6$  layers connected by  $\text{PO}_4$  and Li. The main contribution to the layer thickness and  $a$  parameter arises from the  $\text{MO}_6$  and is thus strongly affected by the radius of the metal cation  $M^{2+}$ ,<sup>71,179</sup> However, in the  $b$  and  $c$  directions, also the size of  $\text{PO}_4$  tetrahedra (P-O bond length) affects the  $\text{MO}_6$  size.<sup>71</sup> For the  $b$  axis, the arrangement is stiffer, but along the  $c$  axis, the structure is more flexible. This has been attributed to the ability of the  $\text{MO}_6$  octahedra to tilt,<sup>179</sup> explaining the minor changes in  $c$  parameter. However, the increasing  $c$  parameter in the Co-substitution scheme suggests additional interactions.<sup>71</sup> In addition to the size differences, the  $\text{Co}^{2+}$  and  $\text{Ni}^{2+}$  show differing Jahn-Teller activities (Table 2). This might affect the size-inconsistent  $c$  parameter behaviour.

As a consequence of changing lattice parameters, the unit cell volume and the Li diffusion area ( $a * c$  in Figure 7) expand for increasing Mn substitution level. For the Co and Ni substitutions, a clearly decreased volume for Li diffusion was predicted, especially for the smaller-sized Ni substituent.<sup>V</sup>

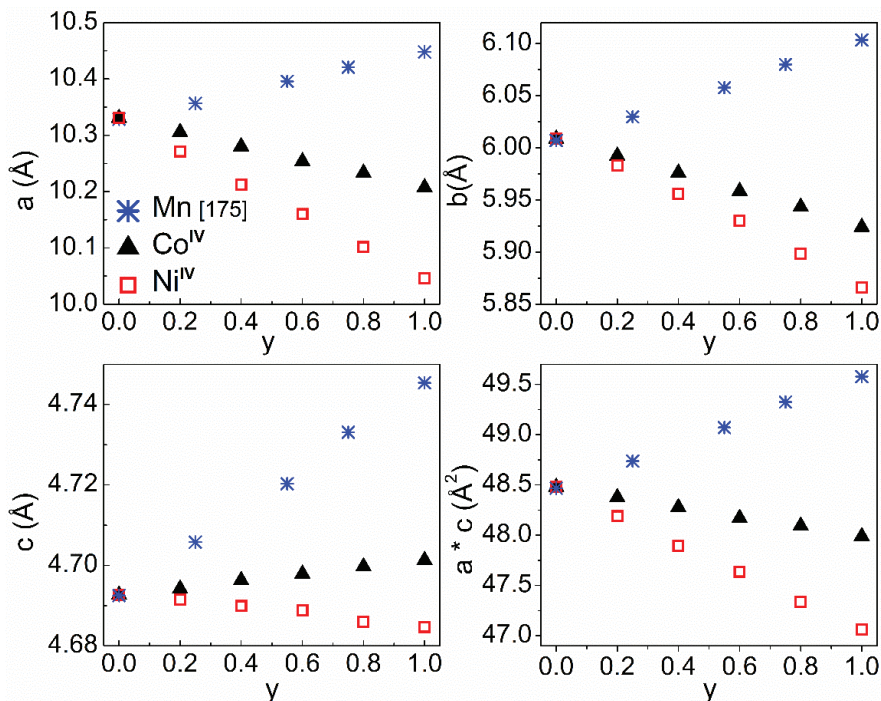


**Figure 7.** Lattice parameter evolution with substitution level  $y$  in the solid-solution series of  $\text{Li}(\text{Fe}_{1-y}\text{M}_y)\text{PO}_4$  ( $M = \text{Mn}$ ,<sup>175</sup>  $\text{Co}^{\text{IV}}$ ,  $\text{Ni}^{\text{IV}}$ ). The product  $a * c$  estimates the Li diffusion channel area.

### 3.1.2 Effect on Fe Local Structure

Changes in the local structure of Fe are predicted with substitution, as the bond lengths and octahedral distortion change. The chemical environment of Fe can be probed with  $^{57}\text{Fe}$  Mössbauer spectroscopy, where a specific  $\gamma$ -radiation source (here  $^{57}\text{Co}$ ) is used to excite  $^{57}\text{Fe}$  isotopes. As a result, a recoil-free, resonant absorption and emission of  $\gamma$ -rays is produced in the solid lattice (*Mössbauer effect*). The radiation source is accelerated through different velocities in order to slightly alter the  $\gamma$ -ray energies (Doppler effect), because changes in the chemical environment shift the  $^{57}\text{Fe}$  nuclear energies. The velocity at which the Mössbauer effect is observed is thus characteristic for a certain Fe local environment.

The Fe valence state is reflected in the isomer shift (IS) with respect to  $\alpha$ -Fe. In the Mössbauer spectrum, this is shown as the location (midpoint) of the corresponding doublet at the velocity axis. Characteristic IS values for the  $\text{Fe}^{2+}$  the  $\text{Fe}^{3+}$  components in olivine structure (octahedral  $\text{FeO}_6$  coordination) are around 1.2 mm/s and 0.4 mm/s,<sup>44,180–182,IV</sup> respectively. The asymmetry of the surrounding electrical environment is displayed in an increasing quadrupole splitting value (QS). This is observed as the doublet width at the velocity axis. In general, the high distortion of the  $\text{FeO}_6$  octahedra in  $\text{LiFePO}_4$  results in exceptionally large QS values. Moreover, due to the asymmetric charge distribution around  $\text{Fe}^{2+}$  ( $d^6$  in  $\text{Fe}^{2+}\text{O}_6$ ),<sup>183</sup> larger QS values are observed for  $\text{Fe}^{2+}$  than for  $\text{Fe}^{3+}$  ( $d^5$  in  $\text{Fe}^{3+}\text{O}_6$ ). A schematic of an  $^{57}\text{Fe}$  Mössbauer spectrum is shown in Figure 8 for a partially delithiated  $\text{Li}_x\text{FePO}_4$  sample, where both  $\text{Fe}^{2+}$  and  $\text{Fe}^{3+}$  are present.

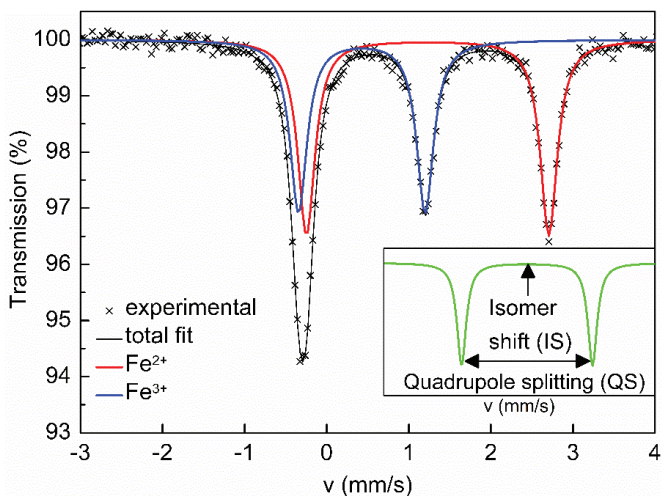


**Figure 8.** Schematic  $^{57}\text{Fe}$  Mössbauer spectrum for a partially delithiated  $\text{Li}_x\text{FePO}_4$  sample, where  $\text{Fe}^{2+}$  and  $\text{Fe}^{3+}$  show their characteristic doublets. Inset shows how isomer shift and quadrupole splitting values are reflected in the doublet location and width at the velocity axis.

For substituted materials, an effect of the next-nearest-neighboring  $M$  on the Fe local electrical environment is generally predicted,<sup>181,182,184</sup> as one  $\text{FeO}_6$  shares corners with four other  $(\text{Fe}/M)\text{O}_6$  octahedra. The local environment of Fe can be altered by the different size or valence state of  $M$ .<sup>181</sup> However, as the  $\text{FeO}_6$  octahedron shares

edges with two neighboring LiO<sub>6</sub> octahedra, also the M1 site occupancy (occupied by Li or vacant) can affect the local structure.

For Li(Fe,Ni)PO<sub>4</sub> powders, a very slightly but still consistently increasing quadrupole splitting value of the Fe<sup>2+</sup> doublet with increasing Ni content was observed.<sup>IV</sup> Corresponding results were reported by Lee *et al.*<sup>185</sup> As the M1 site in Li(Fe,Ni)PO<sub>4</sub> is fully occupied by Li, the changes must be due to the next-nearest Ni neighbors. The slight increase in the quadrupole splitting indicates a minor growth in the environment asymmetry with increasing Ni content. It may be induced by the smaller-sized Ni-substituent or by the different Jahn-Teller activities of Fe<sup>2+</sup> and Ni<sup>2+</sup>. Interestingly, no similar trend was seen for the Co-substituted counterparts.<sup>IV</sup> The dissimilar *c* parameter behaviour might imply a differing distortion between the Ni and Co substitution schemes. This could be related to the slightly different quadrupole splitting trends between increasing substitution levels of Ni and Co.

Although the delithiation state of Li<sub>x</sub>FePO<sub>4</sub> is changed, that is the LiFe<sup>2+</sup>PO<sub>4</sub>/Fe<sup>3+</sup>PO<sub>4</sub> ratio varies (due to the two-phase reaction mechanism, see Chapter 3.3.1), the Mössbauer parameters remain constant.<sup>180,IV</sup> This reflects the constant phase compositions (constant Fe<sup>2+</sup> and Fe<sup>3+</sup> local environments). Interestingly, in the present work, much more significant changes were revealed as the mixed Li<sub>x</sub>(Fe<sub>1-y</sub>M<sub>y</sub>)PO<sub>4</sub> (M = Co, Ni) compositions were investigated.<sup>IV</sup> In Mössbauer measurements, the effect of isovalent substitution at the M2 site has been observed to have only a negligible effect on the Fe<sup>2+</sup> local environment.<sup>182,184,186,IV</sup> On the other hand, a significant change in the electrical environment around the Fe<sup>3+</sup> component has been demonstrated.<sup>182,184,185,IV</sup> At room temperature, one doublet was observed for Fe<sup>3+</sup> in partially delithiated Li<sub>x</sub>(Fe<sub>1-y</sub>Co<sub>y</sub>)PO<sub>4</sub> (*x* = *y*).<sup>182</sup> At 5 K temperature, two overlapping subspectra for the Fe<sup>3+</sup> component were reported,<sup>182,184</sup> due to the better spectral resolution. Rusakov *et al.*<sup>182</sup> and Novikova *et al.*<sup>184</sup> attributed the appearance of two separate subspectra to the Co distribution: one Fe<sup>3+</sup> subspectrum was similar to the unsubstituted FePO<sub>4</sub> sample, having only Fe at the neighboring M2 site (4Fe), and the second to Fe<sup>3+</sup> with one Co neighbor (3Fe1Co). However, with increasing *y*, no further subspectrum, corresponding to two Co neighbors (2Fe2Co), emerged. Moreover, the subspectra relative ratios did not match a random Co distribution; it was concluded that the Co is orderly distributed in a way that each Fe has no more than one Co in the nearest environment.<sup>182,184</sup>

In the present work,<sup>IV</sup> the effect of Co and Ni substitution on the Fe<sup>2+</sup> and Fe<sup>3+</sup> local environments was studied at (i) approx. halfway of the Fe<sup>2+</sup>/Fe<sup>3+</sup> redox region (equal amounts of Fe<sup>2+</sup> and Fe<sup>3+</sup> present) and (ii) fully-charged (4.99 V vs. Li/Li<sup>+</sup>) state (only Fe<sup>3+</sup> present). Figure 9 shows the fitted doublets for the Fe<sup>2+</sup>/Fe<sup>3+</sup> and Fe<sup>3+</sup> components in (i) and (ii) measurement schemes, respectively. For higher *y*, the total amount of Fe was decreased, and thus the relative spectral intensity is smaller. Only insignificant changes in the Fe<sup>2+</sup> doublet were observed with varying *y*. On the contrary, the Fe<sup>3+</sup> doublet showed a clearly decreasing quadrupole splitting with increasing *y*.

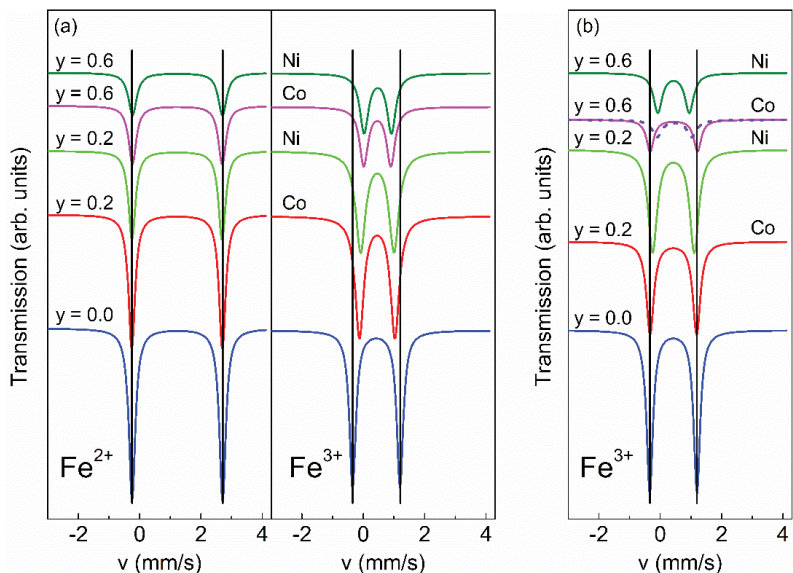


**Figure 9.**  $^{57}\text{Fe}$  Mössbauer spectroscopy results for  $\text{Li}_x(\text{Fe}_{1-y}\text{M}_y)\text{PO}_4$  ( $M = \text{Co}, \text{Ni}$ ) materials at different delithiation states  $x$  and substitution levels  $y$ .<sup>IV</sup> (a) Fitted  $\text{Fe}^{2+}$  and  $\text{Fe}^{3+}$  doublets at approx. halfway of the  $\text{Fe}^{2+}/\text{Fe}^{3+}$  redox region, (b) fitted  $\text{Fe}^{3+}$  doublet(s) at fully-charged (4.99 V vs.  $\text{Li}/\text{Li}^+$ ) state. Only for  $y = 0$ , a minor  $\text{Fe}^{2+}$  doublet (approx. 3% relative area) was observed at the fully-charged state.

In the present work, changes in the  $\text{Fe}^{3+}$  Mössbauer spectrum were attributed primarily to the neighboring M1 site occupancy.<sup>IV</sup> Li *et al.*<sup>181</sup> argued that the M2 site local environment is more affected by the M1 site than by the neighboring M2 site. This was explained by the shorter distance between the edge-sharing M1 and M2 sites compared to the corner-sharing neighboring M2 sites. At the  $\text{Fe}^{2+}/\text{Fe}^{3+}$  redox region, the presence of  $\text{M}^{2+}$  was anticipated to introduce an increased Li occupancy at the neighboring M1 site. Thus if a random  $\text{M}^{2+}$  distribution is assumed,  $\text{Fe}^{3+}$  is expected to experience Li next-nearest-neighbors. According to Figure 9a, this produces a higher symmetry for its electrical environment (decreasing QS with increasing  $y$ ), when compared to  $y = 0$ . This suggested dominating contribution of the neighboring M1 site is supported by the fact that both Co and Ni substitution schemes gave uniform results (different  $M$  at the M2 site) in the present work.<sup>IV</sup> Yamada *et al.*<sup>178</sup> reported a similar effect for a  $\text{Li}_x(\text{Fe},\text{Mn})\text{PO}_4$  material. They discovered a smaller quadrupole splitting value for the  $\text{Fe}^{3+}$  doublet in  $\text{Li}_{0.6}(\text{Fe}_{0.4}\text{Mn}_{0.6})\text{PO}_4$  ( $x = 0.6$ ) compared to the delithiated  $(\text{Fe}_{0.4}\text{Mn}_{0.6})\text{PO}_4$  ( $x = 0$ ) composition.

As the fully-charged samples were considered in the present work (Figure 9b), the Ni substitution scheme showed somewhat smaller quadrupole splitting values in comparison to Co substitution or  $y = 0$ .<sup>IV</sup> This could originate from the residual Li in the Ni-substituted samples, due to a lack of  $\text{Ni}^{2+}/\text{Ni}^{3+}$  couple activity. For the Co-substitution scheme, a more complete delithiation was anticipated. The  $y = 0.2$  sample showed an  $\text{Fe}^{3+}$  doublet very similar to the  $\text{Fe}^{3+}$  doublet in  $y = 0$  compound.<sup>IV</sup> This is attributed to a vacant neighboring M1 site. For  $y = 0.6$ , two  $\text{Fe}^{3+}$  doublets were observed: again one corresponding to  $y = 0$  and one with a smaller quadrupole splitting value.<sup>IV</sup> Presence of  $\text{Fe}^{3+}$  in an additional phase with residual Li, due to poor  $\text{Co}^{2+}/\text{Co}^{3+}$  kinetics and incomplete delithiation, was speculated. This would explain the appearance of two different doublets. For  $y = 0$  ( $\text{LiFePO}_4$ ), due to

phase separation to LiFe<sup>2+</sup>PO<sub>4</sub> and Fe<sup>3+</sup>PO<sub>4</sub>, the neighboring M1 site of Fe<sup>3+</sup> remains vacant for varying delithiation states: no difference in the Fe<sup>3+</sup> doublet between the partially- and fully-delithiated compositions were observed (between Figures 9a and 9b).<sup>IV</sup>

## 3.2 Electrochemical Performance

In general, when optimizing the electrochemical performance for high energy densities, the amount of Fe should be sufficient for ensuring adequate conductivity properties. On the other hand, the amount of *M* should be as high as possible for increased average potential. With optimized carbon coating and particle size minimization, the electrical conductivity can be improved and Li diffusion enhanced. Also high-voltage electrolytes or electrolyte additives should be designed for improving stability at the high-potential *M*<sup>2+</sup>/*M*<sup>3+</sup> plateau and diminishing parasitic electrolyte oxidation reactions.

### 3.2.1 *M*<sup>2+</sup>/*M*<sup>3+</sup> Redox Couple Activity

Although performance degradation has been demonstrated for Li(Fe<sub>1-y</sub>Mn<sub>y</sub>)PO<sub>4</sub><sup>40,46,174,187-189</sup> and Li(Fe<sub>1-y</sub>Co<sub>y</sub>)PO<sub>4</sub><sup>60,63,71,176,190</sup>,<sup>V</sup> materials at higher substitution levels *y*, the Mn<sup>2+</sup>/Mn<sup>3+</sup> and Co<sup>2+</sup>/Co<sup>3+</sup> redox couples show reversible electrochemical activity. However, the Ni<sup>2+</sup>/Ni<sup>3+</sup> couple is significantly more difficult to activate in a reversible manner. For LiNiPO<sub>4</sub>, reversible electrochemical delithiation/lithiation has been only rarely demonstrated, possibly at least partly due to the insufficient conductivity properties. Wolfenstine *et al.*<sup>67</sup> prepared LiNiPO<sub>4</sub> materials under different synthesis conditions; only the samples with electrically conductive phosphide impurities and an additional carbon coating showed electrochemical activity. Furthermore, the graphitic carbon foam/LiNiPO<sub>4</sub> composites (with 90 wt-% carbon) prepared by Dimesso *et al.*<sup>68</sup> have shown reversible electrochemical activity (oxidation at 5.1 – 5.3 V and reduction at 4.9 V vs. Li/Li<sup>+</sup>). For the mixed Li(Fe,Ni)PO<sub>4</sub> compositions, the presence of Fe should improve the electrical conductivity and increase the volume for Li diffusion. Despite this, poor results have been achieved.<sup>70,71,191</sup>,<sup>V</sup>

Qing *et al.*<sup>191</sup> were able to chemically extract over 95% of the Li from a Li(Fe<sub>0.4</sub>Ni<sub>0.6</sub>)PO<sub>4</sub> sample; by electrochemical charging, only 41% delithiation was achieved, corresponding almost entirely to the Fe<sup>2+</sup>/Fe<sup>3+</sup> redox couple. However, for a Li(Fe<sub>0.2</sub>Ni<sub>0.8</sub>)PO<sub>4</sub>/C sample with carbon-coated particles, an initial Ni<sup>2+</sup>/Ni<sup>3+</sup> oxidation peak at 5.2 V vs. Li/Li<sup>+</sup> was detected in the study of Wang *et al.*<sup>70</sup> Nevertheless, no reduction reaction was observed in the subsequent reduction scan, and only the Fe<sup>2+</sup>/Fe<sup>3+</sup> redox couple showed reversible reactions. Similar results were obtained in the present study.<sup>V</sup> Figure 10 presents the initial cyclic voltammetry (CV) scan for Li(Fe<sub>1-y</sub>Ni<sub>y</sub>)PO<sub>4</sub>/C samples. In addition, redox peak areas corresponding to the amount of oxidized/reduced material are shown. The materials were prepared with 5 wt-% addition of sucrose, whereby a carbon-coating of approx. 1 - 2 wt-% was achieved.<sup>IV,V</sup> Oxidation activity in the high-potential (> 4.4 V vs. Li/Li<sup>+</sup>) region was shown only during the first delithiation, and it was attributed to partial oxidation of the Ni<sup>2+</sup>/Ni<sup>3+</sup> couple (Figure 10b).<sup>V</sup> However, no activity at high potentials was de-

ected in the following reduction scan, and only the  $\text{Fe}^{2+}/\text{Fe}^{3+}$  couple showed reversible reactions (Figure 10a). This was regardless of the studied wide range of  $y$ , from high to low Fe contents.

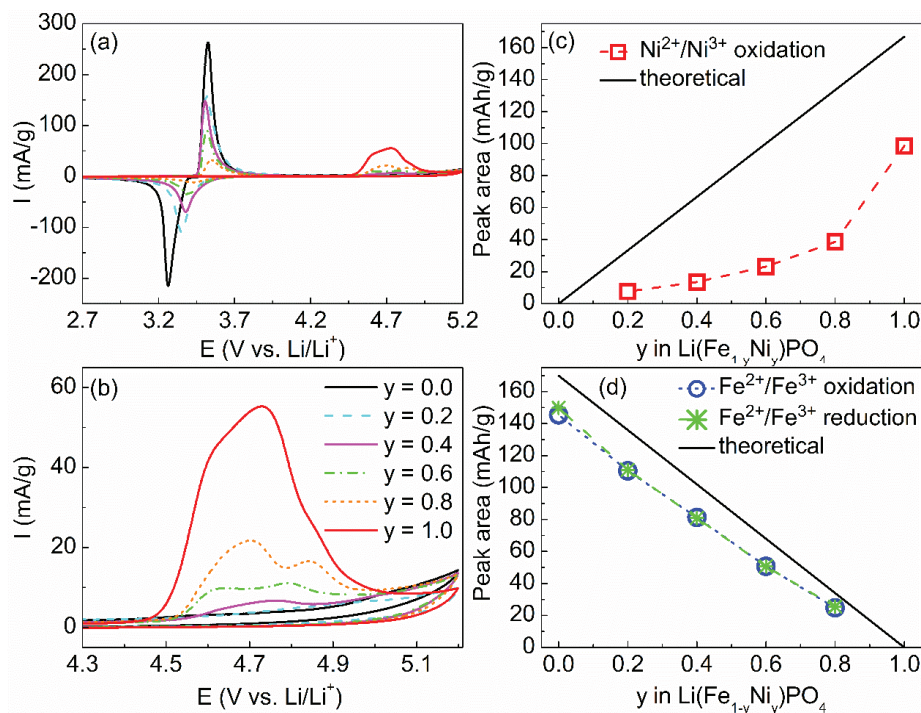


**Figure 10.** Electrochemical performance of  $\text{Li}(\text{Fe}_{1-y}\text{Ni}_y)\text{PO}_4/\text{C}$  materials in cyclic voltammetry at 0.05 mV/s scan rate.<sup>v</sup> (a) - (b) The initial delithiation-lithiation cycle. (c) Peak areas for  $\text{Ni}^{2+}/\text{Ni}^{3+}$  and (d)  $\text{Fe}^{2+}/\text{Fe}^{3+}$  redox couples. In (c) and (d), the theoretical values are shown for comparison.

A common restraint in activating the  $\text{Ni}^{2+}/\text{Ni}^{3+}$  couple in  $\text{Li}(\text{Fe},\text{Ni})\text{PO}_4$  seems to be the poor electrical conductivity, consistent with the results for  $\text{LiNiPO}_4$  materials. The small volume for Li diffusion (Figure 7) may hinder the  $\text{Ni}^{2+}/\text{Ni}^{3+}$  couple activation, too. Nevertheless, electrochemical activity, although not reversible, has been demonstrated only for materials with carbon coated particles.<sup>70,v</sup> Surprisingly, in the present work, the amount of oxidized Ni actually increased with increasing Ni content  $y$  (Figure 10c).<sup>v</sup> An opposite behaviour would be expected, based on the general effect of Fe in the mixed phosphate materials. In the XRD characterization,  $\text{Ni}_3\text{P}$  and  $\text{Li}_4\text{O}_7\text{P}_2$  impurities were detected for the  $\text{Li}(\text{Fe}_{1-y}\text{Ni}_y)\text{PO}_4/\text{C}$  active material powders at  $y \geq 0.6$ .<sup>iv</sup> The amount of impurities was observed to increase with increasing  $y$ ; especially for  $y = 1$  it was considerable.  $\text{Ni}_3\text{P}$  impurities are produced due to the synthesis conditions (carbon-containing precursors or carbon additive heated in Ar atmosphere), and they are known to show a high electrical conductivity.<sup>192,193</sup> Thus the enhanced  $\text{Ni}^{2+}/\text{Ni}^{3+}$  couple oxidation at higher Ni contents is attributed at least partly to the conductivity enhancing  $\text{Ni}_3\text{P}$  impurities, consistently with results discussed for  $\text{LiNiPO}_4$ .<sup>67</sup>

In general, for  $\text{LiNiPO}_4$  materials, clearly larger oxidation responses have been found compared to the reduction direction, implying that the lithiation (Li insertion)

reaction is more hindered than the delithiation (Li extraction).<sup>67,70</sup> It seems that the Li(Fe,Ni)PO<sub>4</sub> materials show the same characteristic, as electrochemical activity has been reported only for the first, initial delithiation.<sup>70</sup> In the present work, it was observed that the Ni<sup>2+</sup>/Ni<sup>3+</sup> redox couple shows the partial oxidation at significantly lower potentials than the predicted 5.1 V vs. Li/Li<sup>+</sup> (Figure 10b). In addition, the varying Fe content did not appear to affect the peak position. Gangulibabu *et al.*<sup>194</sup> claimed to have measured oxidation peak for LiNiPO<sub>4</sub> at 3.82 V and reduction peak at 3.4 V vs. Li/Li<sup>+</sup> (inside 2.8 – 4.8 V cycling range). Rommel *et al.*<sup>73</sup> however speculated that this redox activity was not related to the Ni<sup>2+</sup>/Ni<sup>3+</sup> redox couple, as the potential was significantly lower than the expected > 5 V. Croy *et al.*<sup>195</sup> found that Ni<sup>2+</sup> was oxidized to Ni<sup>3+</sup> already at 4.3 V vs. Li/Li<sup>+</sup> in the LiNiPO<sub>4</sub>-coating of a Li<sub>2</sub>MnO<sub>3</sub>-LiCoO<sub>2</sub> material. However, it was discovered that Ni<sup>2+</sup> had actually displaced the Li in the transition metal layers of Li<sub>2</sub>MnO<sub>3</sub> domains. Taking this into consideration, a structural change could explain the low potential of the Ni<sup>2+</sup>/Ni<sup>3+</sup> oxidation peak in the present work. Nevertheless, no signs of structural destruction were revealed in *ex-situ* XRD analysis of cycled electrodes, and the Fe<sup>2+</sup>/Fe<sup>3+</sup> redox couple in the Li(Fe<sub>1-y</sub>Ni<sub>y</sub>)PO<sub>4</sub> materials showed reversible and stable electrochemical activity (Figure 10d).

The intrinsic difficulty in activating Ni *versus* Co is also reflected in studies investigating Li(Co,Ni)PO<sub>4</sub> materials. Wolfenstine *et al.*<sup>69</sup> expected their Li(Co<sub>1-y</sub>Ni<sub>y</sub>)PO<sub>4</sub> samples (no carbon coating) to show a higher electrical conductivity compared to pure LiNiPO<sub>4</sub>. However, electrochemical activity was demonstrated only for the Co<sup>2+</sup>/Co<sup>3+</sup> redox couple, and the presence of varying amounts of Ni had no effect. Rommel *et al.*<sup>179</sup> prepared carbon-coated Li(Co<sub>1-y</sub>Ni<sub>y</sub>)PO<sub>4</sub>/C materials. For  $y = 1$  (LiNiPO<sub>4</sub>), a broad oxidation peak during the first charge was shown already at 4.46 – 4.62 V vs. Li/Li<sup>+</sup>. This peak was however claimed to appear at a too low potential for the Ni<sup>2+</sup>/Ni<sup>3+</sup> couple oxidation and attributed to either irreversible structural changes or formation of a passivating SEI-layer. No clear oxidation response above 5.0 V was demonstrated, but interference of overlapping parasitic electrolyte oxidation reactions was speculated. For  $y = 0.66$ , no oxidation response near the 4.6 V was observed. However, for  $y = 0.33$ , a similar oxidation peak as for the  $y = 1$  compound was distinguished. Additionally, a small reversible response around 5 V vs. Li/Li<sup>+</sup> for the  $y = 0.33$  was speculated. Based on the present work,<sup>v</sup> the distinct activity of the  $y = 1$  (LiNiPO<sub>4</sub>) sample in comparison to the  $y = 0.66$  sample could be due to an enhanced electrical conductivity: Rommel *et al.*<sup>179</sup> reported Ni<sub>3</sub>P impurities for the  $y = 1$  composition. For the  $y = 0.33$  compound, the higher amount of Co might have improved the conductivity.

### 3.2.2 Shift of Redox Potentials

A mutual influence of Fe and M on the redox potentials has been demonstrated. Figure 11 shows the Fe<sup>2+</sup>/Fe<sup>3+</sup> discharge plateau during galvanostatic cycling and the average redox potential (midpoint of oxidation and reduction peaks in CV measurements) for Li(Fe,Co/Ni)PO<sub>4</sub> materials. For Co substitution, an upward shift in the lower Fe<sup>2+</sup>/Fe<sup>3+</sup> couple potential and a downward shift in the higher Co<sup>2+</sup>/Co<sup>3+</sup> couple potential were observed in the present work.<sup>v</sup> This corresponds to the results reported for Co- and Mn-substituted materials in other studies.<sup>63,173,178,196</sup> For the Ni

substitution scheme, a similar upward shift in the  $\text{Fe}^{2+}/\text{Fe}^{3+}$  couple potential was demonstrated.<sup>v</sup>

Due to two different metal species co-existing at the same M2 lattice site, the average  $M$ -O bond covalence is changed with substitution. In comparison to the end-members ( $y = 0$  or  $1$ ), an increased covalence results in higher redox energy and thus a decreased redox potential. Correspondingly, a decreased covalence increases the redox potential. The altered  $M$ -O covalence can either arise from a changed electronegativity or a changed  $M$ -O bond length.<sup>196</sup> For the Mn-substituted materials, the shift of redox potentials has been attributed to the larger-sized  $\text{Mn}^{2+}$ , which elongates the  $M$ -O bond.<sup>173,196</sup> Additionally, the  $\text{Fe}^{3+}-\text{O}-\text{Mn}^{2+}$  superexchange interactions can destabilize the higher-potential  $\text{Mn}^{2+}/\text{Mn}^{3+}$  couple and increase its redox energy.<sup>40,178,196</sup>

For the smaller-sized Co substituent, the redox potential shift has been assigned to Co being less electropositive than Fe,<sup>196</sup> which decreases the average  $M$ -O bond covalence. As a result, the  $\text{Fe}^{2+}/\text{Fe}^{3+}$  couple redox potential increases and the  $\text{Co}^{2+}/\text{Co}^{3+}$  potential decreases. Superexchange interactions might also affect the  $\text{Co}^{2+}/\text{Co}^{3+}$  couple potential.<sup>196</sup> In the present work, it was anticipated that the Ni substituent, being smaller and even less electropositive than Co, shows a corresponding effect.<sup>v</sup> This would explain the increased  $\text{Fe}^{2+}/\text{Fe}^{3+}$  redox potentials in  $\text{Li}(\text{Fe},\text{Ni})\text{PO}_4$  materials. However, no impact on the  $\text{Ni}^{2+}/\text{Ni}^{3+}$  couple response was detected (Figure 10), but again, no reversible  $\text{Ni}^{2+}/\text{Ni}^{3+}$  redox peaks were demonstrated.

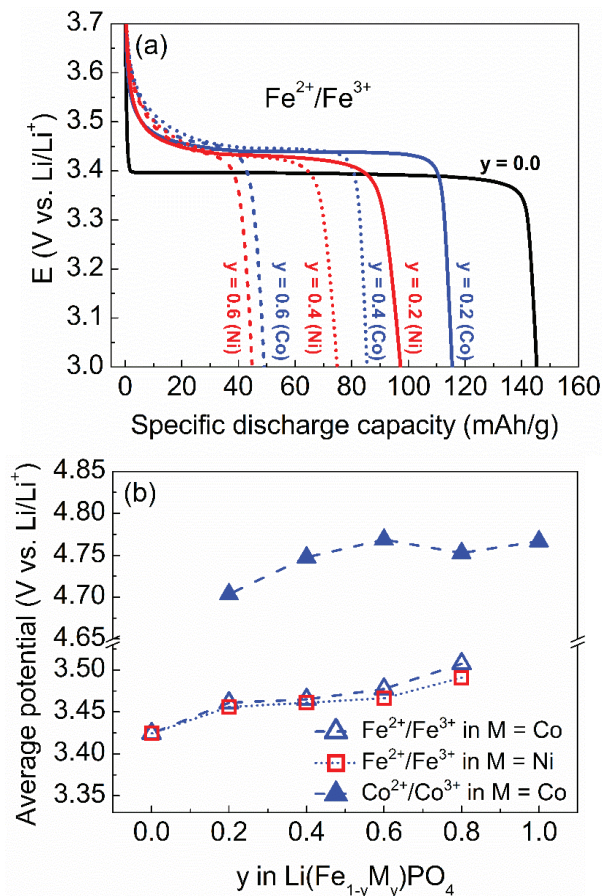


**Figure 11.** Shift of redox potentials in Li(Fe<sub>1-y</sub>M<sub>y</sub>)PO<sub>4</sub> (M = Co, Ni) materials.<sup>v</sup> (a) Galvanostatic Fe<sup>2+</sup>/Fe<sup>3+</sup> discharge plateau at 0.1C rate (preceding charge cut-off voltage 4.1 V vs. Li/Li<sup>+</sup>), (b) average potential of redox peaks in cyclic voltammetry (scan rate 0.05 mV/s).

### 3.2.3 Dependence on Substitution Level

For Li(Fe<sub>1-y</sub>Mn<sub>y</sub>)PO<sub>4</sub> materials, the optimal electrochemical performance has been proposed for substitution levels of  $0.6 \leq y \leq 0.8$ .<sup>46,129,165,174,197,198</sup> In the present work, Li(Fe<sub>1-y</sub>Co<sub>y</sub>)PO<sub>4</sub> materials were tested at different current rates,<sup>v</sup> and the obtained discharge energy densities (specific capacity \* average potential) are shown in Figure 12. In addition, the Co<sup>2+</sup>/Co<sup>3+</sup> redox peak areas from CV measurements are presented. It is concluded that compositions of  $0.2 \leq y \leq 0.6$  show comparable or even higher energy densities in comparison to  $y = 0$  (LiFePO<sub>4</sub>).

For the higher substitution levels  $y$ , although higher potentials were achieved, the discharge capacities were poor and the polarization with increasing current rate was more pronounced. It was assumed that the high Co<sup>2+</sup>/Co<sup>3+</sup> redox potential combined with the high polarization did not allow the oxidation reaction to be fully completed before the charge cut-off voltage (4.9 V vs. Li/Li<sup>+</sup>).<sup>v</sup> A higher charge-voltage limit of 4.99 V was tested, but it resulted in accelerated capacity fade, although the initial capacity values were increased. This emphasizes the high-potential problematics. In this sense the slight, Fe-induced decrease in the Co<sup>2+</sup>/Co<sup>3+</sup> redox potential (Figure

11b) is very beneficial. The  $\text{Co}^{2+}/\text{Co}^{3+}$  redox peak areas showed a growing deviation from the theoretical value with increasing  $y$ , as presented in Figure 12b. Most probably the electrical conductivity or the volume for Li diffusion are not sufficient at higher  $y$ , which again emphasizes the performance enhancing influence of Fe.

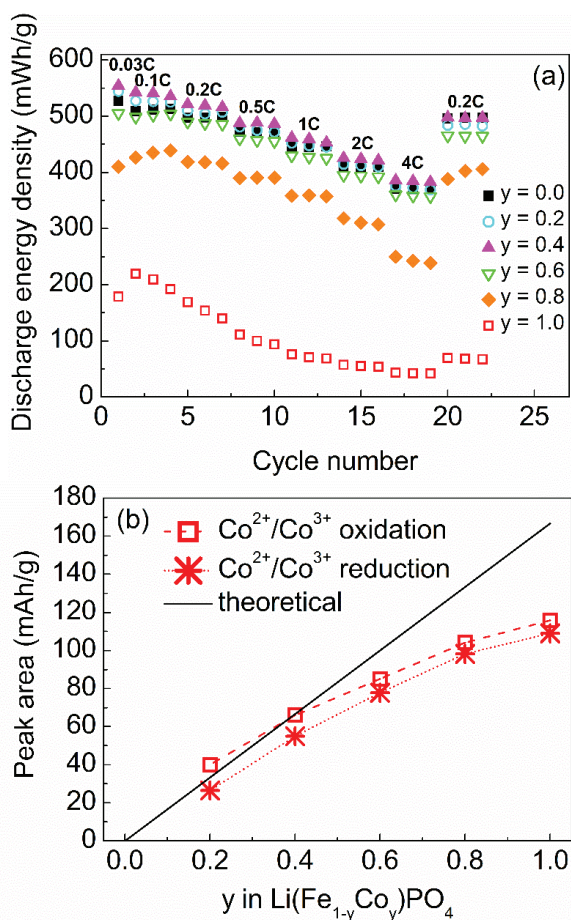


**Figure 12.** The dependence of  $\text{Li}(\text{Fe}_{1-y}\text{Co}_y)\text{PO}_4$  electrochemical performance on substitution level  $y$ . (a) Discharge energy density at different current rates (4.9 V vs.  $\text{Li}/\text{Li}^+$  charge cut-off voltage). 1C defines a current that (dis)charges the cell's theoretical capacity in one hour. (b)  $\text{Co}^{2+}/\text{Co}^{3+}$  redox peak areas in cyclic voltammetry (0.05 mV/s scan rate). Theoretical values are shown for comparison.

### 3.3 Delithiation/Lithiation Characteristics

For EV/HEV applications, for example, fast-charging is needed for efficient operation. For an optimal performance, in addition to a good electronic conductivity, the Li diffusion should be fast. The conductivity properties of  $\text{LiMPO}_4$  materials have been improved by decreasing the particle size and coating the particles with carbon, but also the delithiation/lithiation (charge/discharge) mechanism has an effect. For high charge and discharge rates, the two-phase reaction mechanism is considered to be rate limiting.<sup>199</sup> Interestingly, the delithiation/lithiation mechanism varies with changing  $M$  in  $\text{LiMPO}_4$  and with the isovalent Fe site substitution.

### 3.3.1 End Members LiMPO<sub>4</sub> (M = Mn, Fe, Co, Ni)

The reaction mechanism of LiFePO<sub>4</sub> is still under active discussion.<sup>43</sup> Generally, the delithiation/lithiation is accepted to proceed as a two-phase reaction, where the ratio of LiFePO<sub>4</sub> and FePO<sub>4</sub> phases varies but the phase compositions remain constant. The volume difference between the lithiated/delithiated phases is approx. 6.5%.<sup>40</sup> Different models for this two-phase transition have been presented, for example the core-shell or shrinking core,<sup>40,200</sup> domino-cascade,<sup>201</sup> and mosaic models.<sup>202</sup> Additionally, the two-phase structure co-existence as either intra-particle (two-phase co-existence inside an individual particle) or inter-particle (all individual particles in either delithiated or lithiated form) has been discussed.<sup>203,204</sup> The phase separation produces a kinetic limitation due to single Fe valence (Fe<sup>2+</sup> in LiFePO<sub>4</sub> and Fe<sup>3+</sup> in FePO<sub>4</sub>), as it results in low carrier density.<sup>40,172</sup> Furthermore, the two-phase reaction is restricted by the required nucleation and growth steps of the second phase, in comparison to a single-phase solid-solution mechanism.<sup>199</sup> Thus a diffusional solid-solution pathway would be beneficial for a high rate capability. In fact, the practical rate capabilities achieved for LiFePO<sub>4</sub>-based cells are surprisingly high when compared to the predicted theoretical performance,<sup>205</sup> which puts the current view of the two-phase reaction mechanism in doubt.

Single-phase solid-solution regions in LiFePO<sub>4</sub> materials have been predicted for extreme conditions: high temperatures<sup>206</sup> or extremely small, nano-scale particles.<sup>207,208</sup> However, narrow single-phase regions in Li<sub>x</sub>FePO<sub>4</sub> have been suggested to exist at room temperature outside the LiFePO<sub>4</sub>/FePO<sub>4</sub> miscibility gap, near the initial and final stages of delithiation.<sup>209,210</sup> More recently, experimental evidence of wider single-phase regions has been collected at very high current rates ( $\geq 10\text{C}$ ).<sup>211,212</sup> In addition to the continuous solid-solution regions, metastable intermediate phases ( $x = 0.6 - 0.75$ <sup>212</sup> or  $x = 2/3$ <sup>213</sup>) have also been suggested.

Despite the same olivine structure, the delithiation/lithiation reaction of LiCoPO<sub>4</sub> proceeds in two steps through an intermediate phase. The mechanism consists of two two-phase regions, LiCoPO<sub>4</sub> ↔ Li<sub>x</sub>CoPO<sub>4</sub> and Li<sub>x</sub>CoPO<sub>4</sub> ↔ CoPO<sub>4</sub>,<sup>55</sup> where  $x = 0.755$ .<sup>214</sup> or  $x = 2/3$ .<sup>57</sup> In addition,  $x = 0.2 - 0.45$  composition has been suggested.<sup>215</sup> However, broad co-existence ranges have been observed for the three phases due to slow kinetics. Additionally, a single-phase solid-solution region is speculated to exist in the beginning of delithiation/end of lithiation.<sup>55,57</sup> The reaction mechanism proceeding through an intermediate phase has not yet been fully explained. Nevertheless, the formation of the delithiated CoPO<sub>4</sub> phase is suggested to be energetically less favourable in comparison to FePO<sub>4</sub>,<sup>57,216</sup> and the intermediate Li<sub>x</sub>CoPO<sub>4</sub> phase is proposed to be at least metastable.<sup>214</sup> In practice, the delithiation/lithiation mechanism has been reported to produce two oxidation peaks or charge plateaus.<sup>60,217,218,V</sup> However, for the lithiation (discharge) direction, only one single response is often resolved.<sup>215,217,218,V</sup> It is worth noticing that the metastable phases suggested for Li<sub>x</sub>FePO<sub>4</sub><sup>212,213</sup> show a compositional analogy with the intermediate Li<sub>x</sub>CoPO<sub>4</sub> phase.<sup>55,57,214</sup>

For LiMnPO<sub>4</sub>, a two-phase reaction takes place, but the volume change between lithiated/delithiated phases is higher (almost 9% or over),<sup>219,220</sup> when compared to LiFePO<sub>4</sub>. For LiNiPO<sub>4</sub>, no unambiguous data of the reaction mechanism are available, but a two-phase mechanism has been speculated.<sup>221</sup>

### 3.3.2 Mixed Li(Fe,M)PO<sub>4</sub> (M = Mn, Co, Ni)

For the mixed metal phosphate materials, wide single-phase solid-solution regions have been demonstrated also at equilibrium conditions. The particle size, morphology, and experimental conditions may significantly affect the solid-solution composition existence.

For Li<sub>x</sub>(Fe<sub>1-y</sub>Mn<sub>y</sub>)PO<sub>4</sub> materials, Yamada *et al.*<sup>46,174</sup> first reported a change in the Fe<sup>2+</sup>/Fe<sup>3+</sup> couple redox reaction mechanism: the Fe<sup>2+</sup>/Fe<sup>3+</sup> two-phase reaction was gradually converted to a single-phase solid-solution mechanism with increasing Mn content *y*. For *y* > 0.6, pure single-phase mechanism was observed for the Fe<sup>2+</sup>/Fe<sup>3+</sup> region. Interestingly, the Mn<sup>2+</sup>/Mn<sup>3+</sup> redox reaction was suggested to proceed completely via a two-phase mechanism for all *y*. However, Yamada *et al.*<sup>46,174</sup> used a chemical delithiation method, and contradictory results have been presented. A narrow solid-solution region around  $x \approx y$  ( $0.55 < x < 0.7$  for  $y = 0.6$ <sup>222</sup> and  $0.5 \leq x \leq 0.6$  for  $y = 0.5$ <sup>223</sup>) has been suggested, but wider solid-solution ranges have been proposed, too.<sup>175,224–226</sup>

According to the calculations of Malik *et al.*,<sup>227</sup> a single-phase domain is expected at intermediate delithiation states for Li<sub>x</sub>(Fe<sub>1-y</sub>Mn<sub>y</sub>)PO<sub>4</sub> materials. The single-phase composition is centered at  $x \approx y$ , extending to the Mn<sup>2+</sup>/Mn<sup>3+</sup> region. The single-phase appearance was attributed to the random distribution of Mn in the structure, diluting the interactions leading to phase separation in the end-member compositions (*y* = 0 or 1): the strong Mn<sup>2+</sup>-Li<sup>+</sup> attractive and Fe<sup>3+</sup>-Li<sup>+</sup> repulsive interactions interfere with each other. The contradiction with experimental studies,<sup>46,174</sup> showing a pure two-phase mechanism for the Mn<sup>2+</sup>/Mn<sup>3+</sup> redox reaction, was explained by the strong Jahn-Teller effect of Mn<sup>3+</sup>.<sup>227</sup> The Jahn-Teller effect leads to a severe lattice distortion, which is not well predicted by the calculation model. Thus in practice, a stronger phase-separation interaction is assumed for the Mn<sup>2+</sup>/Mn<sup>3+</sup> region. Malik *et al.*<sup>227</sup> speculated that the scenario of interfering interactions would be applicable to other metal phosphates, too.

For Li<sub>x</sub>(Fe<sub>1-y</sub>Ni<sub>y</sub>)PO<sub>4</sub> materials, the effect of Ni substitution on the Fe<sup>2+</sup>/Fe<sup>3+</sup> redox couple appears not to be examined before. For Li<sub>x</sub>(Fe<sub>1-y</sub>Co<sub>y</sub>)PO<sub>4</sub>, substitution-induced changes in the redox mechanisms have been suggested.<sup>63,161</sup> In the present work, indications of solid-solution compositions in the Fe<sup>2+</sup>/Fe<sup>3+</sup> redox couple region were observed for both Li<sub>x</sub>(Fe<sub>1-y</sub>Co<sub>y</sub>)PO<sub>4</sub> and Li<sub>x</sub>(Fe<sub>1-y</sub>Ni<sub>y</sub>)PO<sub>4</sub> materials at higher *y*.<sup>v</sup> The XRD patterns measured for *ex-situ* electrode samples at approx. halfway of the Fe<sup>2+</sup>/Fe<sup>3+</sup> redox region (equal amounts of Fe<sup>2+</sup> and Fe<sup>3+</sup> present) are shown in Figure 13. At the Fe<sup>2+</sup>/Fe<sup>3+</sup> region, similar changes in phase compositions with increasing *y* were demonstrated for both Co and Ni substitution schemes: the two-phase composition of *y* = 0 is preserved in the *y* = 0.2 samples (Figure 13a), whereas the *y* = 0.6 samples appear to be in a single phase (Figure 13b). Differing phase compositions can exist at other delithiation states, but it is concluded that for higher *y* (*y* = 0.6), indications of a single-phase domain are found at the Fe<sup>2+</sup>/Fe<sup>3+</sup> redox region. Thus corresponding to the discussed Li<sub>x</sub>(Fe<sub>1-y</sub>Mn<sub>y</sub>)PO<sub>4</sub> materials, the Fe<sup>2+</sup>/Fe<sup>3+</sup> redox couple delithiation characteristics depend on the substitution level *y*.

Kosova *et al.*<sup>63</sup> claimed that Li<sub>x</sub>(Fe<sub>1-y</sub>Co<sub>y</sub>)PO<sub>4</sub> materials would show a single-phase delithiation mechanism at all *x* (both Fe<sup>2+</sup>/Fe<sup>3+</sup> and Co<sup>2+</sup>/Co<sup>3+</sup> redox regions) for *y* ≤



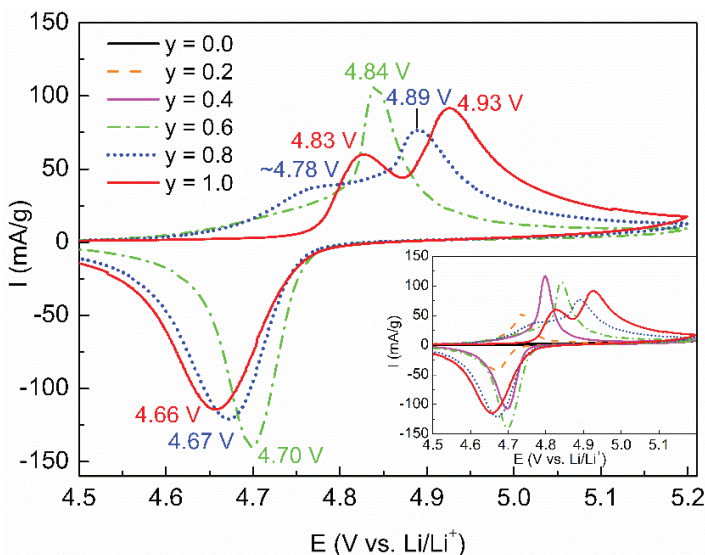


**Figure 14.** Cyclic voltammograms for  $\text{Li}(\text{Fe}_{1-y}\text{Co}_y)\text{PO}_4$  materials at different substitution levels  $y$  (0.05 mV/s scan rate).<sup>v</sup> The corresponding  $\text{Co}^{2+}/\text{Co}^{3+}$  redox peak positions are indicated for  $y = 0.6 - 1.0$ . For  $y < 0.6$  (shown in the inset), only one  $\text{Co}^{2+}/\text{Co}^{3+}$  oxidation/reduction peak was observed.

Interestingly, a similar substitution-induced effect on the  $\text{Co}^{2+}/\text{Co}^{3+}$  redox couple has been observed for  $\text{Li}(\text{Co},\text{Ni})\text{PO}_4$  materials. Rommel *et al.*<sup>179</sup> reported a two-step  $\text{Co}^{2+}/\text{Co}^{3+}$  redox reaction (two oxidation peaks) for  $\text{Li}(\text{Co}_{0.66}\text{Ni}_{0.33})\text{PO}_4$  composition, but no double peak character was indicated or demonstrated for  $\text{Li}(\text{Co}_{0.33}\text{Ni}_{0.66})\text{PO}_4$ . This suggests that the presence of Ni has a similar effect on the  $\text{Co}^{2+}/\text{Co}^{3+}$  redox mechanism as was observed for Fe,<sup>63,v</sup> and also the required substitution levels seem to correspond each other (< 60% Co).

Single-phase existence has been proposed also for other mixed substitution schemes, including  $\text{Li}(\text{Co}_{0.6}\text{Mn}_{0.4})\text{PO}_4$ ,<sup>161</sup>  $\text{Li}(\text{Fe}_{1/3}\text{Mn}_{1/3}\text{Co}_{1/3})\text{PO}_4$ ,<sup>163</sup>  $\text{Li}(\text{Fe}_{0.75}\text{Zn}_{0.25})\text{PO}_4$ ,<sup>228</sup> and  $\text{Li}(\text{Fe}_{0.3}\text{Mn}_{0.2}\text{Mg}_{0.5})\text{PO}_4$ <sup>229</sup> materials. For example, the electrochemically inactive Mg substituent in  $\text{Li}(\text{Fe}_{0.3}\text{Mn}_{0.2}\text{Mg}_{0.5})\text{PO}_4$  was claimed to reduce the lattice strain upon the delithiation/lithiation reaction by decreasing the lattice mismatch and thus suppressing the phase separation.<sup>229</sup> Due to this, a single-phase composition was proposed also for the  $\text{Mn}^{2+}/\text{Mn}^{3+}$  region, different from the behaviour of  $\text{Li}(\text{Fe},\text{Mn})\text{PO}_4$ .

Figure 15 presents the volume decrease from the lithiated to the delithiated phase for different metal phosphate materials. It is to be noticed that in case of the inactive Mg substituent, the lattice volume change is between  $\text{Li}(\text{Fe}_{0.3}\text{Mn}_{0.2}\text{Mg}_{0.5})\text{PO}_4$  and  $\text{Li}_{0.5}(\text{Fe}_{0.3}\text{Mn}_{0.2}\text{Mg}_{0.5})\text{PO}_4$ .<sup>229</sup> As a general trend, it is observed that upon increasing substitution level  $y$ , the volume change between lithiated/delithiated phases decreases for most of the materials. An exception is the  $\text{Li}_x(\text{Fe}_{0.4}\text{Mn}_{0.6})\text{PO}_4$  compound,<sup>178</sup> for which the overall volume change is clearly higher than for other substitution schemes. However, the volume change between  $x = 1$  and  $x = 0.6$  ( $\text{Fe}^{2+}/\text{Fe}^{3+}$ ) is only 1.8%, but a significantly larger difference of 7.1% was indicated between  $x = 0.6$  and  $x = 0$  ( $\text{Mn}^{2+}/\text{Mn}^{3+}$ ). Thus the two-phase  $\text{Mn}^{2+}/\text{Mn}^{3+}$  region seems to be responsible for the large lattice volume change between  $x = 0$  and  $x = 1$

compositions. Furthermore, for LiNiPO<sub>4</sub>, the lattice volume change calculated with the GGA+U method<sup>66</sup> is exceptionally small.

Based on Figure 15, it seems that the discussed appearance of single-phase solid-solution regions is connected to the substitution-induced decrease in the volume change between lithiated and delithiated compositions. When the unit cell volumes of lithiated/delithiated forms were considered,<sup>v</sup> especially the volume of the delithiated phase appeared to increase with substitution. As a result, the lattice volume change decreases for the mixed phosphate materials. According to the Mössbauer measurements in the present work (Figure 9),<sup>iv</sup> due to the presence of Co/Ni in the Li<sub>x</sub>(Fe,Co/Ni)PO<sub>4</sub> materials, the Fe<sup>3+</sup> local environment indeed was changed at the partially delithiated states. The observed increase in the electrical environment symmetry could imply a diminished octahedral distortion in the Fe<sup>3+</sup>O<sub>6</sub> octahedra. Possibly the strong M<sup>2+</sup>-Li<sup>+</sup> attractive and M<sup>3+</sup>-Li<sup>+</sup> repulsive interactions predicted by calculations of Malik *et al.*<sup>227</sup> could contribute to this phenomenon. This would be supported by the observations made here before: the substitution level seems to affect the delithiation/lithiation characteristics rather than the choice of the substituent M.

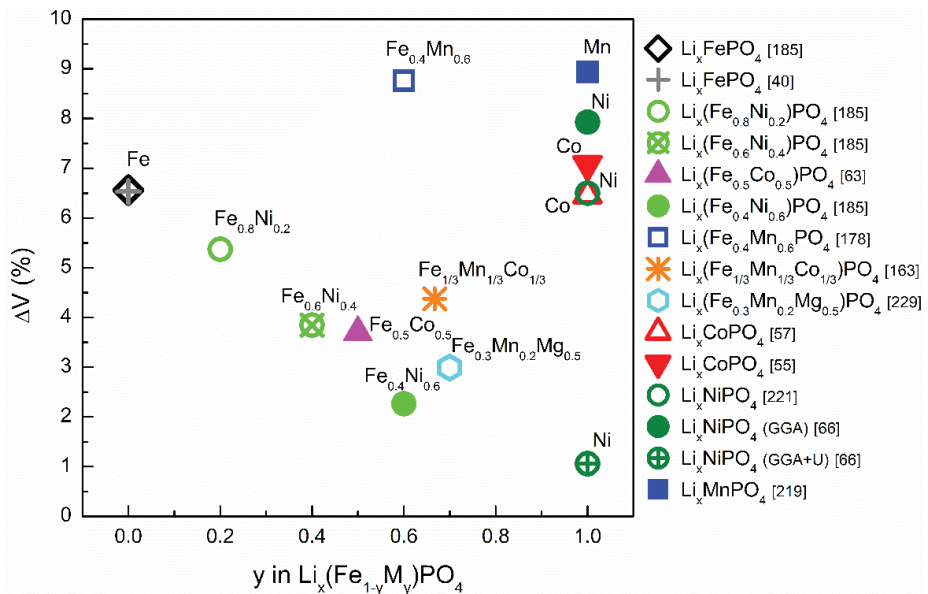


**Figure 15.** Comparison of literature data on unit cell volume decrease between lithiated and delithiated compositions as function of substitution level  $y$  for different Li<sub>x</sub>(Fe<sub>1-y</sub>M<sub>y</sub>)PO<sub>4</sub> materials. Data for Li<sub>x</sub>(Fe<sub>0.3</sub>Mn<sub>0.2</sub>Mg<sub>0.5</sub>)PO<sub>4</sub><sup>229</sup> is between  $x = 1$  and  $x = 0.5$ , for Li<sub>x</sub>NiPO<sub>4</sub><sup>221</sup> between  $x = 1$  and  $x = 0.09$ , and for Li<sub>x</sub>(Fe<sub>0.5</sub>Co<sub>0.5</sub>)PO<sub>4</sub><sup>63</sup> between  $x = 1$  and  $x = 0.04$ .

## 4. Reversible Heat Generation in Li-Ion Cells

In Li-ion batteries, the energy lost to resistances and overpotentials is converted to heat. In large-sized applications, hundreds of individual cells are packed tightly together to form a battery pack. As a result, the area-to-volume ratio is small, which leads to an ineffective heat transfer from the outer surface. As already discussed in Chapter 2, the cell aging and thus cycle life critically depend on the operating and storage temperatures. In addition, the battery safety is affected by the ambient and internal temperatures: it was shown that the risk of Li plating and dendrite formation exists at high temperature cycling.<sup>III</sup> Furthermore, if the cell internal temperature is allowed to rise uncontrollably, thermal runaway reactions can be triggered.

To avoid over-heating and the related aging and safety issues, properly designed cooling systems, either active or passive, are needed in large-sized systems. Implementation of a cooling system decreases the gravimetric and volumetric energy densities and also leads to parasitic power consumption, decreasing the overall system efficiency.<sup>230</sup> This emphasizes accurate sizing of the cooling system. For that, knowledge of the exact heat generation of different cell chemistries at different SOC and current rates is needed. The total heat generation consists of irreversible and reversible parts, where the reversible contribution significantly depends on the electrode materials. Using electrode material combinations with a possibly small net heat generation is often beneficial. In HEV applications for example, the battery operates mainly inside a relatively narrow SOC range (*microcycling*). Thus it is important to know which SOC are favourable in the sense of avoiding extra heat production.

In this chapter, the general theory of heat generation in Li-ion cells is discussed with an emphasis on the reversible part. The entropy change ( $\Delta S$ ) behaviour of individual electrode materials is covered, and the heat generation in different positive-negative electrode combinations are compared.

### 4.1 Thermodynamic Relations of a Li-Ion Cell

In a Li-ion cell, heat is produced due to the electrochemical processes at the positive and negative electrodes, and also due to ohmic losses caused by movement of Li-ions and electrons. The heat generation rate  $Q$  of a Li-ion cell is defined as the amount of heat exchanged between the cell and the surroundings, and it is given here in watts (W). For the following discussion, an exothermic cell reaction is specified as negative heat flow, that is,  $Q < 0$  is generated heat (transferred from the cell to the surround-

ings) and  $Q > 0$  absorbed heat (heat flow from surroundings to the cell). The discharge current direction is determined to be positive in sign.

The battery cell heat generation equation was derived by Bernardi *et al.*,<sup>231</sup> whereby the total heat generation rate  $Q_{total}$  consists of the following terms:

$$Q_{total} = Q_{irreversible} + Q_{reversible} + Q_{mixing} + Q_{phase\ change} \quad (1)$$

$Q_{irreversible}$  describes the polarization losses due to deviation from the open circuit voltage (OCV). The polarization is caused by ohmic losses, charge transfer overpotentials, and mass transfer limitations, related to the cell reaction.  $Q_{reversible}$  is the entropic heating of the electrode reactions, and  $Q_{mixing}$  is due to relaxation of concentration gradients developed inside the cell (important for large particle sizes and high current rates).  $Q_{phase\ change}$  arises from phase changes (other than crystalline phase transition). For Li-ion cells, it is assumed that no side reactions affecting the electrochemical heat generation take place and that no phase change effects exist. Furthermore, the  $Q_{mixing}$  contribution can usually be neglected,<sup>232</sup> especially for the relatively small particle size of commercial cells.<sup>233</sup> For no spatial variation of temperature or SOC, the  $Q_{total}$  can be presented in a simplified form, consisting of only  $Q_{irreversible}$  and  $Q_{reversible}$ .<sup>231,232,234</sup>

$$Q_{total} = Q_{irreversible} + Q_{reversible} = -I^2 R_i + T \Delta S \frac{I}{nF} \quad (2)$$

where  $I$  is the operating current value,  $R_i$  cell's internal resistance,  $T$  temperature,  $\Delta S$  entropy change,  $F$  Faraday's constant, and  $n$  number of electrons participating in the cell reaction (here  $n = 1$ ).  $Q_{irreversible}$  is always exothermic and thus generated heat ( $Q_{irreversible} < 0$ ) for both current directions (charge and discharge). On the contrary,  $Q_{reversible}$  can be either generated or absorbed heat, that is negative or positive in sign, depending on  $\Delta S$  and operating current  $I$ .

Depending on the sum of  $Q_{irreversible}$  and  $Q_{reversible}$ , and on the current direction in Equation 2, the cell either generates heat or cools down absorbing heat from the surroundings. The importance of  $Q_{irreversible}$  versus  $Q_{reversible}$  is determined by several factors: the cell SOC (determines the  $\Delta S$  value), the operating current  $I$ , cell aging ( $R_i$  increases upon aging), and ambient temperature ( $R_i$  decreases and  $|Q_{reversible}|$  increases with increasing temperature). Usually less extra heat is produced at higher temperatures, as the contribution of  $Q_{irreversible}$  is smaller due to decreasing  $R_i$ .<sup>235,236</sup>

In battery thermal modelling and simulation, some studies have neglected the contribution of  $Q_{reversible}$ ,<sup>237,238</sup> or assumed it to be constant with SOC.<sup>239,240</sup> However, Bandhauer *et al.*<sup>232</sup> emphasized the importance of including  $Q_{reversible}$  as function of SOC in thermal models: according to their review, the contribution of  $Q_{reversible}$  is often significant even at a 1C current rate. Furthermore, for a high-rate designed LiFePO<sub>4</sub>/C cell (small  $R_i$ ) at 55 °C temperature, significant contribution from  $Q_{reversible}$  was found even at very high 5C current rate.<sup>236</sup> In the present work, a cooling effect originating from the dominating  $Q_{reversible}$  was shown at low 0.1C discharge rate.<sup>1</sup>

## 4.2 Measuring the Entropy Change

Traditionally,  $\Delta S$  is measured using either a calorimetric or a potentiometric measurement. A novel method called the “electrothermal impedance spectroscopy (ETIS)” was recently introduced by Schmidt *et al.*<sup>241</sup> In the present work, the potentiometric method was mainly used,<sup>I,II</sup> and only a qualitative calorimetric experiment was performed.<sup>I</sup>

In the calorimetric method, the  $Q_{irreversible}$  contribution has to be first determined in order to be able to derive  $Q_{reversible}$  from the calorimetric data.<sup>232</sup> The  $Q_{irreversible}$  could be assumed constant and calculated by measuring the total heat generation:  $Q_{reversible}$  is cancelled out when the charge and discharge directions are subtracted. Alternatively,  $Q_{irreversible}$  can be estimated by calculating the cell overpotential from OCV and operating voltage data. The method accuracy is usually worse than in the potentiometric method: it is restricted by the temperature measurement, especially in case of cells with only little active material,<sup>242</sup> and by the need to separately determine  $Q_{irreversible}$ .<sup>241</sup> Furthermore, a properly sized calorimeter is required, and a large cell heat capacity and inactive mass may cause further measurement error.<sup>235,241</sup>

Potentiometric measurement is based on the temperature dependence of the cell’s OCV, and this method gives a very good accuracy. However, the potentiometric measurements need long measurement times, and the results can be affected by self-discharge phenomena during the extended relaxation periods.<sup>242–244</sup>

In the potentiometric method,  $\Delta S$  is determined by measuring the cell’s OCV at different temperatures  $T$ .  $\Delta S$  is related to the OCV through the Gibbs free energy change  $\Delta G$ :

$$\Delta G = \Delta H - T\Delta S \quad (3)$$

$$\Delta G = -nF(OCV) \quad (4)$$

$$-nF(OCV) = \Delta H - T\Delta S \quad (5)$$

where  $\Delta H$  is the enthalpy change in the cell reaction. Thus the cell OCV is divided into  $\Delta H$  and  $\Delta S$  terms ( $n = 1$ ), and  $\Delta S$  can be calculated from the slope of OCV *versus*  $T$ :

$$OCV = -\frac{\Delta H}{F} + \frac{T\Delta S}{F} \quad (6)$$

$$\Delta S = F \frac{\partial(OCV)}{\partial T} \quad (7)$$

The principle of a potentiometric  $\Delta S$  measurement is illustrated in Figure 16. The cell is first charged/discharged to the desired SOC, and after a stabilization period (several hours), the temperature is ramped and the cell OCV is recorded at each temperature. When the OCV values are plotted *versus* temperature,  $\Delta S$  can be calculated from the slope according to Equation 7. This procedure is repeated at different SOCs.

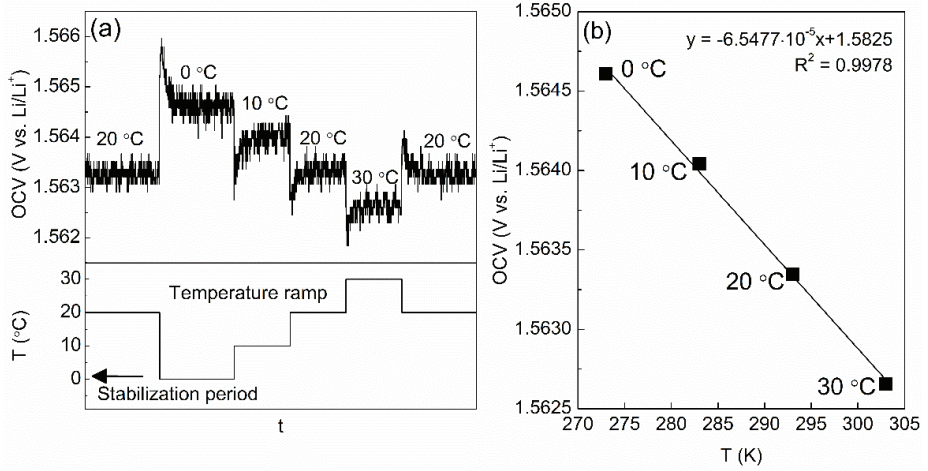


**Figure 16.** Principle of the potentiometric entropy change ( $\Delta S$ ) measurement.<sup>1,11</sup> (a) Temperature ramp and the corresponding change in open circuit voltage (OCV); (b) OCV values as a function of temperature with linear fitting.  $\Delta S$  can be calculated from the slope of OCV versus T.

In ETIS, a sinusoidal excitation current is used to create a heat flow inside the cell, whereby the  $Q_{irreversible}$  and  $Q_{reversible}$  can be separated by their different frequencies.<sup>241</sup> A small, continuous DC current is superimposed to charge/discharge the cell. For calculating  $\Delta S$ , a thermal transfer function needs to be measured for one frequency with another method (typically with the potentiometric method), and the conditions need to remain constant for the further measurements. The advantages of this method are the very short measurement times, good accuracy, and the possibility to perform an almost continuous measurement of  $\Delta S$ . However, the need for calibration measurement is a disadvantage. Additionally, the SOC resolution is poor, which can however be improved by shortening the measurement interval ( $\Delta SOC$ ).

### 4.3 Entropy Change in Different Electrode Materials

For a Li-ion cell electrode, the origin of  $\Delta S$  upon Li insertion/extraction has been assigned to changes mainly in the configurational entropy. Thus the  $\Delta S$  is a measure of the Li arrangement (order/disorder), reflecting the occupancy of Li sites in the electrode material lattices.<sup>245–249</sup> A positive  $\Delta S$  indicates increased disorder (reduction reaction, Li intercalation direction), whereas a negative  $\Delta S$  is a sign of ordering. Thus  $\Delta S$  can give additional information on phase transitions and structural ordering.<sup>245,246,248</sup>

As current is passed through the cell, Li-ions intercalate/deintercalate to/from the electrode material lattices, whereby different Li arrangements occur at different SOC. Thus  $\Delta S$  has to be measured as a function of the SOC, and both the positive and negative electrode contributions have to be included. The full cell's  $\Delta S$  in the discharge direction can be calculated from half-cell data as follows:

$$\begin{aligned} \Delta S_{full\ cell, discharge} &= \Delta S_{positive\ electrode, reduction} + \Delta S_{negative\ electrode, oxidation} \\ &= \Delta S_{positive\ electrode, reduction} - \Delta S_{negative\ electrode, reduction} \end{aligned} \quad (8)$$

The measured values of  $\Delta S$  are for the reduction reaction direction, and thus the negative electrode  $\Delta S$  has to be reversed in sign to obtain the value for oxidation direction. An empty lattice can be considered as very ordered, whereby intercalation of Li is reflected in a large positive  $\Delta S$  (high degree of disorder), as many equivalent sites are available for the Li.<sup>250–252</sup> When sites of equal energy are almost filled, addition of further Li creates a more ordered state (full lattice), resulting in a negative  $\Delta S$ .

In addition to the configurational entropy, other possible contributions are the vibrational and electronic entropies, which are usually neglected for intercalation reactions.<sup>245,246,248,253</sup> The electronic contribution has been shown to be of no significance in comparison to the configurational entropy.<sup>249,250,252</sup> The vibrational entropy can account for overall negative values of  $\Delta S$ , but its contribution is either assumed negligibly small or usually not expected to change with SOC.<sup>245,248,249</sup>

In the present work,  $\Delta S$  behaviour with SOC was determined for different electrode materials.<sup>I,II</sup> The  $\Delta S$  versus SOC curves of  $\text{LiFePO}_4$ ,  $\text{Li}(\text{Fe}_{0.33}\text{Mn}_{0.67})\text{PO}_4$ ,  $\text{Li}_4\text{Ti}_5\text{O}_{12}$ , and graphite materials are shown in Figure 17. The galvanostatic charge-discharge curves at low 0.03C current are also depicted. The measurements were performed with the potentiometric method in half-cells against metallic Li counter electrode. The lithiation/delithiation state is presented by SOC values, where 0% SOC corresponds to a fully-discharged cell (positive electrode lithiated and negative electrode delithiated) and 100% SOC to a fully-charged cell (positive electrode delithiated and negative electrode lithiated).

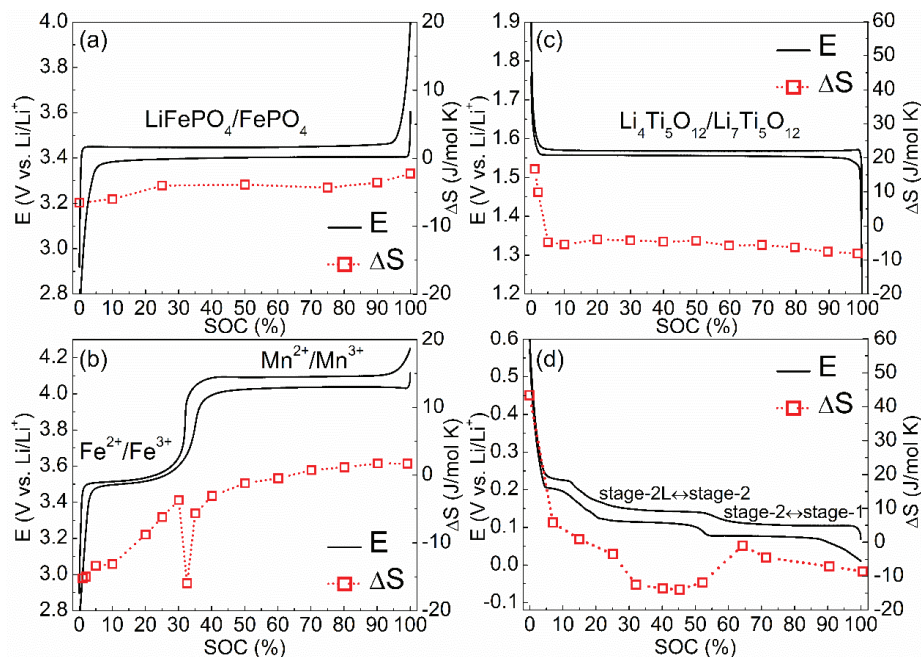


**Figure 17.** Galvanostatic charge-discharge cycle (at 0.03C current) and entropy change ( $\Delta S$ ) as functions of state of charge for different electrode materials. (a)  $\text{LiFePO}_4$ ,<sup>I</sup> (b)  $\text{Li}(\text{Fe}_{0.33}\text{Mn}_{0.67})\text{PO}_4$ ,<sup>II</sup> (c)  $\text{Li}_4\text{Ti}_5\text{O}_{12}$ ,<sup>II</sup> and (d) graphite.<sup>I</sup>

In Figure 17, two basic trends are observed: an essentially constant  $\Delta S$  with SOC of  $\text{LiFePO}_4$  and  $\text{Li}_4\text{Ti}_5\text{O}_{12}$  (except for  $< 5\%$  SOC) materials and a more strongly varying  $\Delta S$  of  $\text{LiFe}_{0.33}\text{Mn}_{0.67}\text{PO}_4$  and graphite. Typically, for a two-phase lithium insertion/extraction mechanism, a constant  $\Delta S$  with SOC is shown. The phase compositions remain unchanged and only their relative amounts vary: the Li arrangement in each phase is not affected by the changing SOC, and no changes in the configurational entropy are observed. For  $\text{LiFePO}_4$  at equilibrium conditions, phase separation to  $\text{LiFePO}_4$  and  $\text{FePO}_4$  is expected. This was observed to be reflected in the constant  $\Delta S$  vs. SOC.<sup>I</sup> However, narrow solid-solution areas outside the miscibility gap have been suggested for small  $\text{LiFePO}_4$  particles ( $< 200$  nm), and these regions have been concluded to show sharp changes in the otherwise constant  $\Delta S$ .<sup>209,243,253</sup> In the present work, no signs of such sharp changes were observed (Figure 17a), but the particle size was considerably larger.<sup>I</sup>

For  $\text{Li}_4\text{Ti}_5\text{O}_{12}$ , a two-phase lithiation/delithiation mechanism with co-existing  $\text{Li}_4\text{Ti}_5\text{O}_{12}/\text{Li}_7\text{Ti}_5\text{O}_{12}$  phases has been generally suggested.<sup>87,254,255</sup> In the present work, the constant  $\Delta S$  vs. SOC plateau of  $\text{Li}_4\text{Ti}_5\text{O}_{12}$  at 5 – 100% SOC was attributed to a two-phase behaviour.<sup>II</sup> A constant  $\Delta S$  for the intermediate SOCs has been reported in other studies,<sup>256,257</sup> too. For the 0 – 3% SOC range, a narrow single-phase solid-solution region has been proposed to exist.<sup>87</sup> The steep decrease in  $\Delta S$  at the beginning of Li intercalation ( $< 5\%$  SOC, Figure 17c) could be due to such single-phase region. Additionally, Li intercalates to the initially empty 16c site of  $\text{Li}_4\text{Ti}_5\text{O}_{12}$ . Thus the intercalation of first Li-ions could create disorder and result in a positive  $\Delta S$  values. However, at the same time, the Li originally in the spinel  $\text{Li}_4\text{Ti}_5\text{O}_{12}$  structure moves from the 8a site to the 16c site to form rock-salt structured  $\text{Li}_7\text{Ti}_5\text{O}_{12}$ .<sup>258</sup> This may also affect the  $\Delta S$  features.

On the contrary to  $\text{LiFePO}_4$  and  $\text{Li}_4\text{Ti}_5\text{O}_{12}$  materials, several plateaus in  $\Delta S$  versus SOC were observed for the graphite electrode (Figure 17d): the  $\Delta S$  behaviour follows the Li ordering (*staging*) in the graphite lattice.<sup>I</sup> At first, the empty graphite lattice can be considered as very ordered. Intercalation of Li to form the dilute stage-1' compound was shown as an increased disorder (strong  $\Delta S > 0$  for 0 – 10 % SOC). A smaller incline of  $\Delta S$  was observed for further lithiation. At approx. 30 - 50% SOC and further at 50 – 100% SOC, two distinct plateaus in the  $\Delta S$  curve were demonstrated. These plateaus correspond to the stage-2L $\leftrightarrow$ stage-2 and stage-2 $\leftrightarrow$ stage-1 transitions, respectively, reflecting the two-phase co-existence. According to Reynier *et al.*,<sup>250,252</sup> the vibrational part of  $\Delta S$  contributes to the overall negative  $\Delta S$  values of graphite at SOCs higher than 25%.

For the  $\text{Li}(\text{Fe}_{0.33}\text{Mn}_{0.67})\text{PO}_4$  material,  $\Delta S$  behaviour with SOC was discovered to follow the distinct  $\text{Fe}^{2+}/\text{Fe}^{3+}$  and  $\text{Mn}^{2+}/\text{Mn}^{3+}$  redox plateaus (Figure 17b), 0 – 33% and 33 – 100% SOC, respectively.<sup>II</sup> In comparison to the un-substituted  $\text{LiFePO}_4$  (Figure 17a), a more sloping  $\Delta S$  was demonstrated in the  $\text{Fe}^{2+}/\text{Fe}^{3+}$  region of the Mn-substituted material. This could be due to a changed  $\text{Fe}^{2+}/\text{Fe}^{3+}$  reaction mechanism, which has been suggested for  $\text{Li}(\text{Fe},\text{Mn})\text{PO}_4$  materials, as discussed in Chapter 3.3.2. For the lithiation direction at the  $\text{Fe}^{2+}/\text{Fe}^{3+}$  plateau (from 33% to 0% SOC),  $\Delta S$  shows a decreasing trend towards 0% SOC. This could be caused by existence of a solid-solution region, where equivalent lattice sites are filled with Li towards 0%

SOC. For the  $\text{Mn}^{2+}/\text{Mn}^{3+}$  plateau, a more constant  $\Delta S$  versus SOC was observed (similar to  $\text{LiFePO}_4$ ), consistent with a two-phase scenario.

In the transition region from  $\text{Fe}^{2+}/\text{Fe}^{3+}$  to  $\text{Mn}^{2+}/\text{Mn}^{3+}$ , a steep negative peak in  $\Delta S$  was observed in the present work (at approx. 33% SOC, equal to the Fe content).<sup>11</sup> This could be a composition with high degree of ordering (corresponding to a completely full or empty lattice). Alternatively, if a narrow single-phase region is assumed to exist only at the transition region, the sharp  $\Delta S$  could reflect the Li arrangement in that single-phase domain. Corresponding sharp changes in  $\Delta S$  have been reported for the solid-solution regions of  $\text{LiFePO}_4$ <sup>209,253</sup> and oxide positive electrode materials.<sup>242,245,246,248,249</sup> Dodd<sup>243</sup> measured the  $\Delta S$  behaviour of a  $\text{Li}(\text{Fe}_{0.8}\text{Mn}_{0.2})\text{PO}_4$  material. A similar sharp change in  $\Delta S$  near the  $\text{Fe}^{2+}/\text{Fe}^{3+}$  to  $\text{Mn}^{2+}/\text{Mn}^{3+}$  transition region was reported. Otherwise, regions of steeper  $\Delta S$  versus SOC were speculated to indicate solid-solution behaviour either at the  $\text{Fe}^{2+}/\text{Fe}^{3+}$  to  $\text{Mn}^{2+}/\text{Mn}^{3+}$  transition region or inside the  $\text{Fe}^{2+}/\text{Fe}^{3+}$  region.

In general, equivalent  $\Delta S$  results have been achieved with both calorimetric and potentiometric methods.<sup>246</sup> The potentiometric measurements are performed at equilibrium condition, whereas a constant current is applied in the calorimetric method. Thus if unstable phase-compositions exist, for example relaxation of a single-phase solid-solution to a two-phase composition, the two methods can give differing results.<sup>253</sup>

For measurements in half-cell configurations, the Li counter electrode theoretically affects the measured  $\Delta S$  values. However, its contribution is not assumed to change with SOC, as the electrode composition and chemical environment of Li remain constant.<sup>248,250,252</sup> Furthermore, Yazami *et al.*<sup>248</sup> measured a negligibly small  $\Delta S$  of 0.2 J/(mol K) for a cell with one fresh and one cycled Li electrode. This implies that no change in the Li counter electrode contribution is expected.

#### 4.4 Entropy Change in Full Cells

As different electrode materials are combined for different cell chemistries, the sum of their  $\Delta S$  values is to be examined. According to Equation 2, the  $Q_{\text{reversible}}$  direction (evolved or absorbed heat) is changed with the current direction (charge/discharge). Thus if a cooling effect due to positive  $Q_{\text{reversible}}$  and heat absorption is observed for discharge, the effect is reversed for the charge cycle and extra heat is produced (negative  $Q_{\text{reversible}}$ ).  $Q_{\text{reversible}}$  can induce significant heat accumulation in the cell;<sup>236</sup> only if the cycling is performed around a specific SOC, the effect of  $Q_{\text{reversible}}$  cancels out. To retain possibly constant heating profiles, a net  $\Delta S$  close to zero would be ideal. In terms of matching the positive and negative electrodes, possibly equal  $\Delta S$  values for the reduction direction are thus beneficial (Equation 8). In addition to the obvious use of  $\Delta S$  versus SOC data to design and scale cooling systems, the method could be utilized in choosing the most favourable SOC ranges for the battery operation.

In the present work, the  $Q_{\text{reversible}}$  was evaluated based on half-cell  $\Delta S$  data for cells of  $\text{LiFePO}_4$  or  $\text{Li}(\text{Fe}_{0.33}\text{Mn}_{0.67})\text{PO}_4$  positive and graphite or  $\text{Li}_4\text{Ti}_5\text{O}_{12}$  negative electrodes.<sup>1,11</sup> The calculated net  $\Delta S$  values versus SOC (Equation 8) for different cell chemistries are shown in Figure 18. In discharge direction, a positive net  $\Delta S$  results in positive  $Q_{\text{reversible}}$  (heat absorption) and a negative net  $\Delta S$  in negative  $Q_{\text{reversible}}$  (ex-

tra heat production). In the charge direction, the sign of  $Q_{reversible}$  is reversed. It is to be noticed that the measured half-cell values for negative electrodes have to be reversed in sign, in order to match the full cell  $\Delta S$  in the discharge direction (Equation 8).

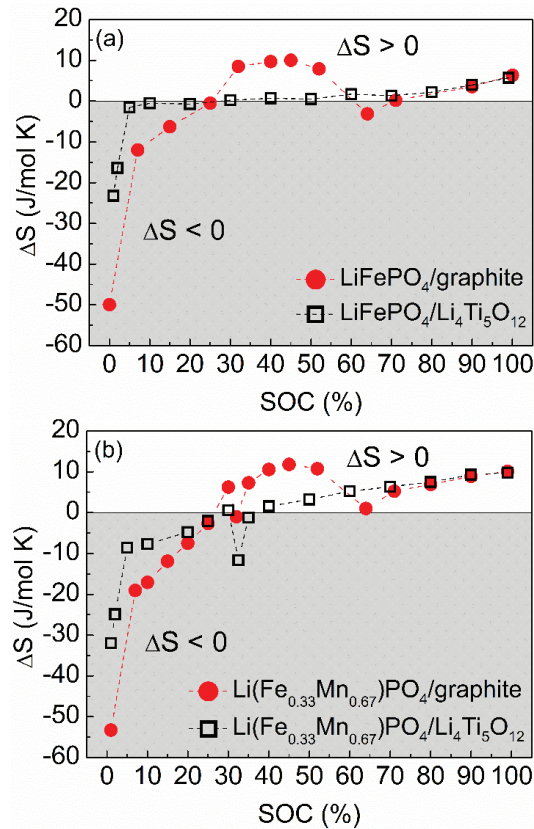


**Figure 18.** Entropy change ( $\Delta S$ ) as function of state of charge for different positive/negative electrode material combinations.<sup>1,11</sup> (a) LiFePO<sub>4</sub> and (b) Li(Fe<sub>0.33</sub>Mn<sub>0.67</sub>)PO<sub>4</sub> positive electrode combined with Li<sub>4</sub>Ti<sub>5</sub>O<sub>12</sub> or graphite negative electrode.

It was observed in the present work that extending the cycling SOC range to  $< 10\%$  SOC results in a sharp negative peak in the net  $\Delta S$  (Figure 18).<sup>1,11</sup> This arises from the strong positive  $\Delta S$  of both Li<sub>4</sub>Ti<sub>5</sub>O<sub>12</sub> and graphite negative electrodes (Figure 17). In practice, extra heat production is proposed at the end of discharge, and correspondingly, a cooling effect in the beginning of charging. The effect is especially strong for the graphite negative electrode. Also when comparing the  $> 10\%$  SOC regions, it was discovered that using Li<sub>4</sub>Ti<sub>5</sub>O<sub>12</sub> instead of graphite is beneficial in minimizing changes in the net  $\Delta S$  with SOC (Figure 18). For the graphite containing cells, a significant positive net  $\Delta S$  region at approx. 30 – 50% SOC was detected. This originates from the negative  $\Delta S$  during the stage-2L $\leftrightarrow$ stage-2 transition. The positive net  $\Delta S$  would result in extra cooling effect upon discharge and correspondingly, extra heating during charge. Mn substitution in the Li(Fe<sub>0.33</sub>Mn<sub>0.67</sub>)PO<sub>4</sub> material is concluded to slightly increase the net  $\Delta S$  values in comparison to LiFePO<sub>4</sub>.

Additionally, it brings about a sharp negative  $\Delta S$  peak at the specific SOC<sub>7</sub> where the Fe<sup>2+</sup>/Fe<sup>3+</sup> redox couple region changes to the Mn<sup>2+</sup>/Mn<sup>3+</sup> region.

In general, for layered Li(Co,Ni)O<sub>2</sub> oxides and LiMn<sub>2</sub>O<sub>4</sub> spinel, larger variations in  $\Delta S$  with SOC have been demonstrated.<sup>257</sup> These variations are due to phase transitions and the constantly changing Li content of the solid-solution regions. As a result, unwanted strong fluctuations in  $Q_{reversible}$  are predicted. For LiCoO<sub>2</sub>, the phase transition between hexagonal and monoclinic structures is shown as sharp changes in  $\Delta S$ .<sup>249,259</sup> For LiMn<sub>2</sub>O<sub>4</sub>, an s-shaped  $\Delta S$  curve is observed,<sup>242,245,246</sup> produced by two sublattices in which Li occupies sites with different energies. For Li(Ni,Co,Mn)O<sub>2</sub>, a constant  $\Delta S$  with SOC has been measured.<sup>257</sup>

The importance of  $\Delta S$  in practice was shown in the present work by potentiometrically measuring the  $\Delta S$  and by performing a qualitative calorimetric experiment for a commercial 45 Ah LiFePO<sub>4</sub>/graphite cell.<sup>1</sup>  $\Delta S$  versus SOC and the measured cell temperature change (describing the heat generation) during a 0.1C constant current charge/discharge cycle are presented in Figure 19. The heat generation behaviour predicted by the  $\Delta S$  data was observed to be reflected as corresponding temperature changes during charge/discharge. The dominant full cell positive  $\Delta S$ , originating from the negative  $\Delta S$  at graphite electrode's stage-2L $\leftrightarrow$ stage-2 transition, is seen as a cooling effect during discharge. Correspondingly, the strong negative  $\Delta S$  near 0% SOC, caused by the graphite electrode's strongly positive  $\Delta S$ , is demonstrated as extra heat generation at the end of discharge. Opposite effects were demonstrated during the charge cycle.

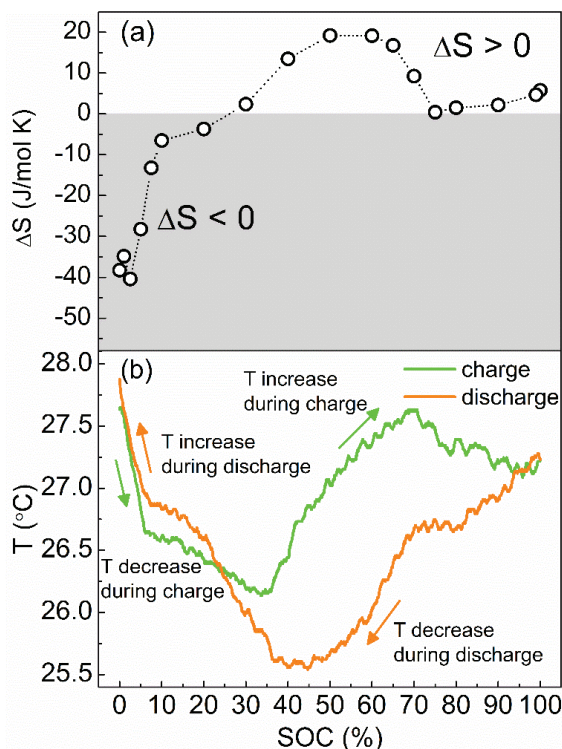


**Figure 19.** (a) Full cell entropy change ( $\Delta S$ ) and (b) cell temperature (during 0.1C charge/discharge) as functions of state of charge for a commercial 45 Ah LiFePO<sub>4</sub>/graphite cell.<sup>1</sup>

When simulating the net  $\Delta S$  of a full cell, the positive-to-negative electrode ratio has to be taken into account, as it shifts the relative SOC. For materials with sharp peaks in  $\Delta S$  with changing SOC, this can affect the locations of beneficial SOC ranges for cycling. Differing  $\Delta S$  curves were demonstrated for cells with the same  $\text{LiFePO}_4/\text{graphite}$  chemistry but different manufacturer.<sup>241</sup> This was explained by different locations of the graphite electrode's stage-2 $\leftrightarrow$ stage-1 transition at the SOC axis, caused by different positive-to-negative electrode ratios. Furthermore, due to aging, the individual electrodes' accessible SOC windows will shift along the SOC axis, which will also shift the  $\Delta S$  versus SOC curves.

## 5. Conclusions

In this work, various Li-ion battery electrode materials were studied from the viewpoint of large-sized battery packs for transportation and energy storage purposes. In particular, the cell safety and lifetime with maintaining adequate energy density were the crucial issues for which proper combinations of positive and negative electrodes were evaluated.

When the cycle aging of commercial Li-ion cells was studied at different temperatures, it was observed that issues related to the graphite negative electrode and its SEI-layer are mostly responsible for the cell aging. Especially in this work, Li plating was demonstrated not only as a consequence of low-temperature cycling but also after prolonged cycling at elevated temperatures: it was shown that increasing the discharge temperature from +45 °C to +65 °C resulted in significantly different aging mechanisms and reduced cell safety. The nature of the plated Li on the graphite negative electrode was found to be fundamentally different depending on the temperature; the high temperature Li plating leads to irreversible, dendritic depositions, which are difficult to distinguish without cell disassembly and post-mortem analysis. The mechanism was related in this work to excessive SEI-layer reactions at the graphite electrode, caused by the elevated temperature, and the resulting lack of electrolyte and the increased amount of gaseous components. In addition to a fast capacity fade, the ohmic resistance was observed to increase with increasing amount of Li plating. In a large battery, the internal temperature of the cells placed in the middle might be significantly elevated, producing different aging phenomena like high-temperature Li plating, although the overall operating temperature would be in tolerable limits. Furthermore, the possible formation of dendritic Li depositions should be taken into account when concerning second-life applications.

For safe batteries with long lifetimes, the graphite negative electrode must be replaced, and  $\text{Li}_4\text{Ti}_5\text{O}_{12}$  seems to be a good alternative. For  $\text{Li}_4\text{Ti}_5\text{O}_{12}$ , extremely long cycle lives have been demonstrated, and the reported gas evolution problem most probably could be avoided or at least suppressed by assuring extremely dry conditions in cell assembly or by electrolyte optimization. At the positive electrode side,  $\text{LiFePO}_4$  seems to benefit from the stable olivine structure, when compared to the oxide counterparts.<sup>135,260</sup> For the  $\text{LiFePO}_4/\text{Li}_4\text{Ti}_5\text{O}_{12}$  chemistry, excellent fast charging, safety, and lifetime properties have been demonstrated with 95% of original capacity after 30 000 cycles.<sup>41</sup> However, the nominal cell voltage is decreased from 3.2 V to 1.9 V when graphite negative electrode is substituted with  $\text{Li}_4\text{Ti}_5\text{O}_{12}$ . As a consequence, the related energy density is significantly reduced, leading to decreased EV driving ranges, for example. To compensate for this, high-voltage positive electrode materials with intrinsic structural safety are needed. Promising results

have been achieved with high-voltage metal phosphates: 3.2 V operating voltage was demonstrated for  $\text{LiCoPO}_4/\text{Li}_4\text{Ti}_5\text{O}_{12}$  cells.<sup>261,262</sup> However, the cycling performance of  $\text{LiMPO}_4$  ( $M = \text{Mn, Co, Ni}$ ) materials is not optimal.

Due to their stable olivine structure, mixed  $\text{Li}(\text{Fe}_{1-y}\text{M}_y)\text{PO}_4$  ( $M = \text{Co, Ni}$ ) materials were investigated in this work as new high-voltage positive electrodes:  $M$  increases the average potential but Fe enhances the conductivity properties and the overall performance, in comparison to the  $y = 0$  and 1 compositions, respectively. The  $M$ -for-Fe substitution was shown to have a mutual influence on both counterparts, in terms of *e.g.* shifting redox potentials and changing the  $\text{Fe}^{2+}/\text{Fe}^{3+}$  and  $M^{2+}/M^{3+}$  delithiation/lithiation characteristics. For higher  $M$  contents, a single-phase solid-solution mechanism appears to be induced at the  $\text{Fe}^{2+}/\text{Fe}^{3+}$  redox region, regardless of  $M$ . Especially the substitution was observed to alter the  $\text{Fe}^{3+}$  local environment. This effect was speculated to arise mainly from the next-nearest-neighboring Li, introduced by the presence of  $M^{2+}$ .

Although both Co and Ni substituents similarly influenced the  $\text{Fe}^{2+}/\text{Fe}^{3+}$  couple characteristics, reversible activation of the  $\text{Ni}^{2+}/\text{Ni}^{3+}$  redox couple itself was not achieved in this work, not even at higher Fe contents. At least the poor electrical conductivity seems to inhibit the  $\text{Ni}^{2+}/\text{Ni}^{3+}$  redox activity, based on the observed beneficial effects of carbon-coating and highly electrically conductive secondary phosphide phases. An initial, irreversible oxidation response was demonstrated at clearly lower potentials than the predicted  $\text{Ni}^{2+}/\text{Ni}^{3+}$  couple redox potential. The possibility of Ni moving to a different lattice site should be studied, as it might explain the lower potential and irreversible behaviour.

Based on this work, a composition around  $\text{Li}(\text{Fe}_{0.5}\text{Co}_{0.5})\text{PO}_4$  was proposed to be optimal, as it would show both a high energy density and a beneficial solid-solution delithiation/lithiation mechanism. In general, for more extensively investigated  $\text{Li}(\text{Fe,Mn})\text{PO}_4$  materials, advanced synthesis methods and particle surface treatments have already been studied,<sup>187,263</sup> but the  $\text{Li}(\text{Fe,Co/Ni})\text{PO}_4$  materials are not yet that far optimized. However, in order for the Co- and Ni-substituted electrodes to be commercialized, high-voltage electrolytes have to be developed,<sup>264,265</sup> based on for example fluorinated solvents,<sup>266–268</sup> special additives,<sup>268,269</sup> or ionic liquids.<sup>270,271</sup> Furthermore, as for many other electrode materials, the HF generated by the  $\text{LiPF}_6$  electrolyte salt decomposition has been proposed to be detrimental for the delithiated  $\text{CoPO}_4$ .<sup>65</sup> Discovering HF-free electrolyte systems would be extremely beneficial.

The dependence of the Li-ion cell heat generation on its electrode materials was studied in this work. Knowledge of the heat generation is particularly important for large-scale battery packs and for designing their cooling systems, in order to avoid the detrimental effect of elevated temperatures to cell lifetime and safety. The different delithiation/lithiation mechanisms of positive and negative electrode materials are reflected as different Li arrangements in their lattices. Thus for each studied material ( $\text{LiFePO}_4$ ,  $\text{Li}(\text{Fe}_{0.33}\text{Mn}_{0.67})\text{PO}_4$ , graphite, and  $\text{Li}_4\text{Ti}_5\text{O}_{12}$ ), a characteristic  $\Delta S$  versus SOC behaviour was observed. A cooling effect during discharging a commercial  $\text{LiFePO}_4/\text{graphite}$  cell at low current could be predicted based on the measured  $\Delta S$  data. This effect was attributed to the graphite electrode's stage-2L $\leftrightarrow$ stage-2 transition. Furthermore, according to the calculated net  $\Delta S$  values of different positive/negative electrode material combinations, the 0 – 10% SOC range was deter-

mined to be unfavourable: it causes extra heat production and fluctuations in the cell temperature. The underlying reason is the large configurational  $\Delta S$  of intercalating the first Li into an empty graphite or  $\text{Li}_4\text{Ti}_5\text{O}_{12}$  electrode lattice. Additionally, changes in the  $\text{Li}(\text{Fe}_{0.33}\text{Mn}_{0.67})\text{PO}_4$  delithiation/lithiation mechanism due to the Mn-for-Fe substitution were suggested to affect the  $\Delta S$  behaviour.

Due to the sensitivity to structural changes,  $\Delta S$  measurements could be more widely used in cell diagnostics as a non-destructive tool, for example in monitoring the cell state of health or aging. Based on the results demonstrated for  $\text{Li}(\text{Fe},\text{Mn})\text{PO}_4$ , measuring the  $\Delta S$  characteristics of  $\text{Li}(\text{Fe},\text{Co}/\text{Ni})\text{PO}_4$  materials could give interesting information on the delithiation/lithiation mechanisms, in addition to the traditional diffraction methods. However, in order to be able to perform potentiometric measurements with long stabilization times at these higher potential  $M^{2+}/M^{3+}$  redox plateaus, a high-voltage electrolyte is needed.

# References

- 1 J.-M. Tarascon and M. Armand, *Nature*, 2001, **414**, 359–367.
- 2 T. H. Kim, J. S. Park, S. K. Chang, S. Choi, J. H. Ryu and H. K. Song, *Adv. Energy Mater.*, 2012, **2**, 860–872.
- 3 B. Scrosati, *J. Electrochem. Soc.*, 1992, **139**, 2776–2781.
- 4 G. Jeong, Y.-U. Kim, H. Kim, Y.-J. Kim and H.-J. Sohn, *Energy Environ. Sci.*, 2011, **4**, 1986–2002.
- 5 U.S. Department of Energy, Energy Efficiency & Renewable Energy, FY 2014 Annual Progress Report - Energy Storage R&D, 2015, pp. 11-12. Available at [http://energy.gov/sites/prod/files/2015/03/f20/FY2014\\_APR\\_Energy\\_Storage\\_R%26D\\_FINAL\\_Part1\\_of\\_3\\_o.pdf](http://energy.gov/sites/prod/files/2015/03/f20/FY2014_APR_Energy_Storage_R%26D_FINAL_Part1_of_3_o.pdf) (accessed 11.8.2015).
- 6 D. Andre, S.-J. Kim, P. Lamp, S. F. Lux, F. Maglia, O. Paschos and B. Stiaszny, *J. Mater. Chem. A*, 2015, **3**, 6709–6732.
- 7 United States Council for Automotive Research LLC - USABC Goals for Advanced Batteries for EVs - CY 2020. Available at [http://www.uscar.org/commands/files\\_download.php?files\\_id=364](http://www.uscar.org/commands/files_download.php?files_id=364) (accessed 11.8.2015)
- 8 Q. Wang, P. Ping, X. Zhao, G. Chu, J. Sun and C. Chen, *J. Power Sources*, 2012, **208**, 210–224.
- 9 F. Orsini, a Du Pasquier, B. Beaudoin, J. . Tarascon, M. Trentin, N. Langenhuizen, E. De Beer and P. Notten, *J. Power Sources*, 1998, **76**, 19–29.
- 10 F. Orsini, a. du Pasquier, B. Beaudouin, J. M. Tarascon, M. Trentin, N. Langenhuizen, E. de Beer and P. Notten, *J. Power Sources*, 1999, **81-82**, 918–921.
- 11 R. Bhattacharyya, B. Key, H. Chen, A. S. Best, A. F. Hollenkamp and C. P. Grey, *Nat. Mater.*, 2010, **9**, 504–510.
- 12 R. M. Spotnitz, J. Weaver, G. Yeduvaka, D. H. Doughty and E. P. Roth, *J. Power Sources*, 2007, **163**, 1080–1086.
- 13 M. S. Islam and C. A. J. Fisher, *Chem. Soc. Rev.*, 2014, **43**, 185–204.
- 14 M. Winter, J. O. Besenhard, M. E. Spahr and P. Novák, *Adv. Mater.*, 1998, **10**, 725–763.
- 15 H. Ge, N. Li, D. Li, C. Dai and D. Wang, *J. Phys. Chem. C*, 2009, **113**, 6324–6326.
- 16 K. Mizushima, P. C. Jones, P. J. Wiseman and J. B. Goodenough, *Mater. Res. Bull.*, 1980, **15**, 783–789.
- 17 J. N. Reimers and J. R. Dahn, *J. Electrochem. Soc.*, 1992, **139**, 2091–2097.
- 18 G. G. Amatucci, J. M. Tarascon and L. C. Klein, *Solid State Ionics*, 1996, **83**, 167–173.

- 19 J. R. Dahn, U. von Sacken, M. W. Juzkow and H. Al-Janaby, *J. Electrochem. Soc.*, 1991, **138**, 2207–2211.
- 20 S. Yamada, M. Fujiwara and M. Kanda, *J. Power Sources*, 1995, **54**, 209–213.
- 21 T. Ohzuku, A. Ueda and M. Nagayama, *J. Electrochem. Soc.*, 1993, **140**, 1862–1870.
- 22 W. Li and J. C. Currie, *J. Electrochem. Soc.*, 1997, **144**, 2773–2779.
- 23 A. Rougier, I. Saadoune, P. Gravereau, P. Willmann and C. Delmas, *Solid State Ionics*, 1996, **90**, 83–90.
- 24 Y. Wang, J. Jiang and J. R. Dahn, *Electrochem. Commun.*, 2007, **9**, 2534–2540.
- 25 I. Belharouak, W. Lu, D. Vissers and K. Amine, *Electrochem. Commun.*, 2006, **8**, 329–335.
- 26 T. Ohzuku and Y. Makimura, *Chem. Lett.*, 2001, **30**, 642–643.
- 27 L. Wang, J. Li, X. He, W. Pu, C. Wan and C. Jiang, *J. Solid State Electrochem.*, 2009, **13**, 1157–1164.
- 28 K. M. Shaju, G. V. Subba Rao and B. V. R. Chowdari, *Electrochim. Acta*, 2002, **48**, 145–151.
- 29 I. Belharouak, Y. K. Sun, J. Liu and K. Amine, *J. Power Sources*, 2003, **123**, 247–252.
- 30 Y. W. Zeng, *J. Power Sources*, 2008, **183**, 316–324.
- 31 S.-C. Yin, Y.-H. Rho, I. Swainson and L. F. Nazar, *Chem. Mater.*, 2006, **18**, 1901–1910.
- 32 O. Dolotko, A. Senyshyn, M. J. Mühlbauer, K. Nikolowski and H. Ehrenberg, *J. Power Sources*, 2014, **255**, 197–203.
- 33 T. Ohzuku, M. Kitagawa and T. Hirai, *J. Electrochem. Soc.*, 1990, **137**, 769–775.
- 34 J. M. Tarascon, W. R. McKinnon, F. Coowar, T. N. Bowmer, G. Amatucci and D. Guyomard, *J. Electrochem. Soc.*, 1994, **141**, 1421–1431.
- 35 M. M. Thackeray, *Prog. Solid State Chem.*, 1997, **25**, 1–71.
- 36 G. G. Amatucci, A. Blyr, C. Sigala, P. Alfonse and J. M. Tarascon, *Solid State Ionics*, 1997, **104**, 13–25.
- 37 Y. Xia, Y. Zhou and M. Yoshio, *J. Electrochem. Soc.*, 1997, **144**, 2593–2600.
- 38 M. M. Thackeray, Y. Shao-Horn, A. J. Kahaian, K. D. Kepler, E. Skinner, J. T. Vaughey and S. A. Hackney, *Electrochem. Solid-State Lett.*, 1998, **1**, 7–9.
- 39 M. M. Thackeray, S.-H. Kang, C. S. Johnson, J. T. Vaughey, R. Benedek and S. A. Hackney, *J. Mater. Chem.*, 2007, **17**, 3112–3125.
- 40 A. K. Padhi, K. S. Nanjundaswamy and J. B. Goodenough, *J. Electrochem. Soc.*, 1997, **144**, 1188–1194.
- 41 K. Zaghib, M. Dontigny, A. Guerfi, P. Charest, I. Rodrigues, A. Mauger and C. M. Julien, *J. Power Sources*, 2011, **196**, 3949–3954.

- 42 L.-X. Yuan, Z.-H. Wang, W.-X. Zhang, X.-L. Hu, J.-T. Chen, Y.-H. Huang and J. B. Goodenough, *Energy Environ. Sci.*, 2011, **4**, 269–284.
- 43 J. Wang and X. Sun, *Energy Environ. Sci.*, 2015, **8**, 1110–1138.
- 44 A. Yamada, S. C. Chung and K. Hinokuma, *J. Electrochem. Soc.*, 2001, **148**, A224–A229.
- 45 H. Huang, S.-C. Yin and L. F. Nazar, *Electrochem. Solid-State Lett.*, 2001, **4**, A170–A172.
- 46 A. Yamada and S.-C. Chung, *J. Electrochem. Soc.*, 2001, **148**, A960–A967.
- 47 C. Delacourt, L. Laffont, R. Bouchet, C. Wurm, J.-B. Leriche, M. Morcrette, J.-M. Tarascon and C. Masquelier, *J. Electrochem. Soc.*, 2005, **152**, A913–A921.
- 48 M. Yonemura, A. Yamada, Y. Takei, N. Sonoyama and R. Kanno, *J. Electrochem. Soc.*, 2004, **151**, A1352–A1356.
- 49 A. Yamada, M. Hosoya, S. C. Chung, Y. Kudo, K. Hinokuma, K. Y. Liu and Y. Nishi, *J. Power Sources*, 2003, **119-121**, 232–238.
- 50 Z. X. Nie, C. Y. Ouyang, J. Z. Chen, Z. Y. Zhong, Y. L. Du, D. S. Liu, S. Q. Shi and M. S. Lei, *Solid State Commun.*, 2010, **150**, 40–44.
- 51 S. Okada, S. Sawa, M. Egashira, J. I. Yamaki, M. Tabuchi, H. Kageyama, T. Konishi and A. Yoshino, *J. Power Sources*, 2001, **97-98**, 430–432.
- 52 K. Amine, H. Yasuda and M. Yamachi, *Electrochem. Solid-State Lett.*, 2000, **3**, 178–179.
- 53 M. Nakayama, S. Goto, Y. Uchimoto, M. Wakihara and Y. Kitajima, *Chem. Mater.*, 2004, **16**, 3399–3401.
- 54 J. Wolfenstine, J. Read and J. L. Allen, *J. Power Sources*, 2007, **163**, 1070–1073.
- 55 N. N. Bramnik, K. Nikolowski, C. Baetz and K. G. Bramnik, *Chem. Mater.*, 2007, **19**, 908–915.
- 56 J. Wolfenstine, U. Lee, B. Poesche and J. L. Allen, *J. Power Sources*, 2005, **144**, 226–230.
- 57 M. Kaus, I. Issac, R. Heinzmann, S. Doyle, S. Mangold, H. Hahn, V. S. K. Chakravadhanula, C. Kübel, H. Ehrenberg and S. Indris, *J. Phys. Chem. C*, 2014, **118**, 17279–17290.
- 58 N. N. Bramnik, K. G. Bramnik, C. Baetz and H. Ehrenberg, *J. Power Sources*, 2005, **145**, 74–81.
- 59 J. Xu, S. L. Chou, M. Avdeev, M. Sale, H. K. Liu and S. X. Dou, *Electrochim. Acta*, 2013, **88**, 865–870.
- 60 R. Ruffo, C. M. Mari, F. Morazzoni, F. Rosciano and R. Scotti, *Ionics*, 2007, **13**, 287–291.
- 61 J. Wolfenstine, *J. Power Sources*, 2006, **158**, 1431–1435.

- 62 Y.-M. Kang, Y.-I. Kim, M.-W. Oh, R.-Z. Yin, Y. Lee, D.-W. Han, H.-S. Kwon, J. H. Kim and G. Ramanath, *Energy Environ. Sci.*, 2011, **4**, 4978–4983.
- 63 N. V. Kosova, O. A. Podgornova, E. T. Devyatkina, V. R. Podugolnikov and S. A. Petrov, *J. Mater. Chem. A*, 2014, **2**, 20697–20705.
- 64 N. N. Bramnik, K. G. Bramnik, T. Buhrmester, C. Baehtz, H. Ehrenberg and H. Fuess, *J. Solid State Electrochem.*, 2004, **8**, 558–564.
- 65 E. Markevich, R. Sharabi, H. Gottlieb, V. Borgel, K. Fridman, G. Salitra, D. Aurbach, G. Semrau, M. A. Schmidt, N. Schall and C. Bruenig, *Electrochem. Commun.*, 2012, **15**, 22–25.
- 66 F. Zhou, M. Cococcioni, K. Kang and G. Ceder, *Electrochem. Commun.*, 2004, **6**, 1144–1148.
- 67 J. Wolfenstine and J. Allen, *J. Power Sources*, 2005, **142**, 389–390.
- 68 L. Dimesso, D. Becker, C. Spanheimer and W. Jaegermann, *J. Solid State Electrochem.*, 2012, **16**, 3791–3798.
- 69 J. Wolfenstine and J. Allen, *J. Power Sources*, 2004, **136**, 150–153.
- 70 D. Wang, J. Xiao, W. Xu and J.-G. Zhang, 15th International Meeting on Lithium Batteries Abstr.#372, 2010.
- 71 J. Molenda, A. Kulka, A. Milewska, W. Zajac and K. Świerczek, *Materials*, 2013, **6**, 1656–1687.
- 72 K. Rissouli, K. Benkhoulja, J. R. Ramos-Barrado and C. Julien, *Mater. Sci. Eng. B*, 2003, **98**, 185–189.
- 73 S. M. Rommel, N. Schall, C. Brünig and R. Wehrich, *Monatshefte Chem.-Chem. Mon.*, 2014, **145**, 385–404.
- 74 J. R. Dahn, *Phys. Rev. B*, 1991, **44**, 9170–9177.
- 75 D. Aurbach, Y. Ein-Eli, B. Markovsky, A. Zaban, S. Luski, Y. Carmeli and H. Yamin, *J. Electrochem. Soc.*, 1995, **142**, 2882–2890.
- 76 R. Fong, U. von Sacken and J. R. Dahn, *J. Electrochem. Soc.*, 1990, **137**, 2009–2013.
- 77 D. Aurbach, Y. Ein-Eli, O. Chusid, Y. Carmeli, M. Babai and H. Yamin, *J. Electrochem. Soc.*, 1994, **141**, 603–611.
- 78 J. Vetter, P. Novák, M. R. Wagner, C. Veit, K. C. Möller, J. O. Besenhard, M. Winter, M. Wohlfahrt-Mehrens, C. Vogler and A. Hammouche, *J. Power Sources*, 2005, **147**, 269–281.
- 79 P. Arora, R. E. White and M. Doyle, *J. Electrochem. Soc.*, 1998, **145**, 3647–3667.
- 80 P. Arora, M. Doyle and R. E. White, *J. Electrochem. Soc.*, 1999, **146**, 3543–3553.
- 81 S. S. Zhang, K. Xu and T. R. Jow, *J. Power Sources*, 2006, **160**, 1349–1354.
- 82 T. Ohzuku, A. Ueda, N. Yamamoto and Y. Iwakoshi, *J. Power Sources*, 1995, **54**, 99–102.

- 83 T. Ohzuku, A. Ueda and N. Yamamoto, *J. Electrochem. Soc.*, 1995, **142**, 1431–1435.
- 84 E. Ferg, R. J. Gummow, A. De Kock and M. M. Thackeray, *J. Electrochem. Soc.*, 1994, **141**, L147–L150.
- 85 K. Kanamura, H. Naito and Z. Takehara, *Chem. Lett.*, 1997, **1**, 45–46.
- 86 K. Amine, I. Belharouak, Z. Chen, T. Tran, H. Yumoto, N. Ota, S. T. Myung and Y. K. Sun, *Adv. Mater.*, 2010, **22**, 3052–3057.
- 87 S. Scharner, W. Weppner and P. Schmid-Beurmann, *J. Electrochem. Soc.*, 1999, **146**, 857–861.
- 88 S. Panero, P. Reale, F. Ronci, B. Scrosati, P. Perfetti and V. R. Albertini, *Phys. Chem. Chem. Phys.*, 2001, **3**, 845–847.
- 89 T. Rauhala, K. Jalkanen and T. Kallio, *Unpublished results*.
- 90 C. Forgez, D. Vinh Do, G. Friedrich, M. Morcrette and C. Delacourt, *J. Power Sources*, 2010, **195**, 2961–2968.
- 91 M. Klett, R. Eriksson, J. Groot, P. Svens, K. Ciosek Högstöm, R. W. Lindström, H. Berg, T. Gustafson, G. Lindbergh and K. Edström, *J. Power Sources*, 2014, **257**, 126–137.
- 92 T. Waldmann, M. Wilka, M. Kasper, M. Fleischhammer and M. Wohlfahrt-Mehrens, *J. Power Sources*, 2014, **262**, 129–135.
- 93 M. Petzl, M. Kasper and M. A. Danzer, *J. Power Sources*, 2015, **275**, 799–807.
- 94 G. Sarre, P. Blanchard and M. Broussely, *J. Power Sources*, 2004, **127**, 65–71.
- 95 M. Wohlfahrt-Mehrens, C. Vogler and J. Garche, *J. Power Sources*, 2004, **127**, 58–64.
- 96 M. Broussely, P. Biensan, F. Bonhomme, P. Blanchard, S. Herreyre, K. Nechev and R. J. Staniewicz, *J. Power Sources*, 2005, **146**, 90–96.
- 97 Y. Li, M. Bettge, B. Polzin, Y. Zhu, M. Balasubramanian and D. P. Abraham, *J. Electrochem. Soc.*, 2013, **160**, A3006–A3019.
- 98 T. Yoon, S. Park, J. Mun, J. H. Ryu, W. Choi, Y. S. Kang, J. H. Park and S. M. Oh, *J. Power Sources*, 2012, **215**, 312–316.
- 99 B. Stiaszny, J. C. Ziegler, E. E. Krauß, J. P. Schmidt and E. Ivers-Tiffée, *J. Power Sources*, 2014, **251**, 439–450.
- 100 B. Stiaszny, J. C. Ziegler, E. E. Krauß, M. Zhang, J. P. Schmidt and E. Ivers-Tiffée, *J. Power Sources*, 2014, **258**, 61–75.
- 101 R. Fu, S. Y. Choe, V. Agubra and J. Fergus, *J. Power Sources*, 2014, **261**, 120–135.
- 102 M. Koltypin, D. Aurbach, L. Nazar and B. Ellis, *Electrochem. Solid-State Lett.*, 2007, **10**, A40–A44.
- 103 S. Malmgren, K. Ciosek, R. Lindblad, S. Plogmaker, J. Kühn, H. Rensmo, K. Edström and M. Hahlin, *Electrochim. Acta*, 2013, **105**, 83–91.

- 104 K. Edström, T. Gustafsson and J. O. Thomas, *Electrochim. Acta*, 2004, **50**, 397–403.
- 105 P. Niehoff and M. Winter, *Langmuir*, 2013, **29**, 15813–15821.
- 106 K. Ciosek Högström, M. Hahlin, S. Malmgren, M. Gorgoi, H. Rensmo and K. Edström, *J. Phys. Chem. C*, 2014, **118**, 12649–12660.
- 107 P. Maire, A. Evans, H. Kaiser, W. Scheifele and P. Novák, *J. Electrochem. Soc.*, 2008, **155**, A862–A865.
- 108 S. J. Harris, A. Timmons, D. R. Baker and C. Monroe, *Chem. Phys. Lett.*, 2010, **485**, 265–274.
- 109 M. Petzl and M. A. Danzer, *J. Power Sources*, 2014, **254**, 80–87.
- 110 R. Spotnitz, *J. Power Sources*, 2003, **113**, 72–80.
- 111 H. J. Ploehn, P. Ramadass and R. E. White, *J. Electrochem. Soc.*, 2004, **151**, A456–A462.
- 112 D. Aurbach, *J. Power Sources*, 2000, **89**, 206–218.
- 113 B. Markovsky, a. Rodkin, Y. S. Cohen, O. Palchik, E. Levi, D. Aurbach, H. J. Kim and M. Schmidt, *J. Power Sources*, 2003, **119-121**, 504–510.
- 114 D. Aurbach, B. Markovsky, A. Rodkin, M. Cojocar, E. Levi and H. J. Kim, *Electrochim. Acta*, 2002, **47**, 1899–1911.
- 115 R. Imhof and P. Novák, *J. Electrochem. Soc.*, 1998, **145**, 3313–3319.
- 116 N. Legrand, B. Knosp, P. Desprez, F. Lapique and S. Raël, *J. Power Sources*, 2014, **245**, 208–216.
- 117 Z. Li, J. Huang, B. Yann Liaw, V. Metzler and J. Zhang, *J. Power Sources*, 2014, **254**, 168–182.
- 118 J. Fan and S. Tan, *J. Electrochem. Soc.*, 2006, **153**, A1081–A1092.
- 119 M. C. Smart and B. V. Ratnakumar, *J. Electrochem. Soc.*, 2011, **158**, A379–A389.
- 120 B. V. Ratnakumar and M. C. Smart, *Electrochem. Soc. Trans.*, 2010, **25**, 241–252.
- 121 I. Belharouak, G. M. Koenig and K. Amine, *J. Power Sources*, 2011, **196**, 10344–10350.
- 122 H.-G. Jung, M. W. Jang, J. Hassoun, Y.-K. Sun and B. Scrosati, *Nat. Commun.*, 2011, **2**, 1–5.
- 123 I. Belharouak, G. M. Koenig, T. Tan, H. Yumoto, N. Ota and K. Amine, *J. Electrochem. Soc.*, 2012, **159**, A1165–A1170.
- 124 R. Bernhard, S. Meini and H. A. Gasteiger, *J. Electrochem. Soc.*, 2014, **161**, A497–A505.
- 125 P. Svens, R. Eriksson, J. Hansson, M. Behm, T. Gustafsson and G. Lindbergh, *J. Power Sources*, 2014, **270**, 131–141.

- 126 K. Wu, J. Yang, Y. Zhang, C. Wang and D. Wang, *J. Appl. Electrochem.*, 2012, **42**, 989–995.
- 127 Y.-B. He, B. Li, M. Liu, C. Zhang, W. Lv, C. Yang, J. Li, H. Du, B. Zhang, Q.-H. Yang, J.-K. Kim and F. Kang, *Sci. Rep.*, 2012, **2**, 1–9.
- 128 Y. B. He, M. Liu, Z. D. Huang, B. Zhang, Y. Yu, B. Li, F. Kang and J. K. Kim, *J. Power Sources*, 2013, **239**, 269–276.
- 129 V. Borgel, G. Gershinsky, T. Hu, M. G. Theivanayagam and D. Aurbach, *J. Electrochem. Soc.*, 2013, **160**, A650–A657.
- 130 H. Kuriyama, H. Saruwatari, H. Satake, A. Shima, F. Uesugi, H. Tanaka and T. Ushirogouchi, *J. Power Sources*, 2015, **275**, 99–105.
- 131 M. Safari and C. Delacourt, *J. Electrochem. Soc.*, 2011, **158**, A1123–A1135.
- 132 P. Liu, J. Wang, J. Hicks-Garner, E. Sherman, S. Soukiazian, M. Verbrugge, H. Tataria, J. Musser and P. Finamore, *J. Electrochem. Soc.*, 2010, **157**, A499–A507.
- 133 K. Amine, J. Liu, S. Kang, I. Belharouak, Y. Hyung, D. Vissers and G. Henriksen, *J. Power Sources*, 2004, **129**, 14–19.
- 134 H. Zheng, Q. Sun, G. Liu, X. Song and V. S. Battaglia, *J. Power Sources*, 2012, **207**, 134–140.
- 135 A. Eddahech, O. Briat and J.-M. Vinassa, *Energy*, 2015, **84**, 542–550.
- 136 J. Wang, Y. Tang, J. Yang, R. Li, G. Liang and X. Sun, *J. Power Sources*, 2013, **238**, 454–463.
- 137 J. Wang, J. Yang, Y. Tang, R. Li, G. Liang, T.-K. Sham and X. Sun, *J. Mater. Chem. A*, 2013, **1**, 1579–1586.
- 138 K. Amine, J. Liu and I. Belharouak, *Electrochem. Commun.*, 2005, **7**, 669–673.
- 139 D. Aurbach, M. D. Levi, E. Levi, H. Teller, B. Markovsky, G. Salitra, U. Heider and L. Heider, *J. Electrochem. Soc.*, 1998, **145**, 3024–3034.
- 140 D. Aurbach, K. Gamolsky, B. Markovsky, G. Salitra, Y. Gofer, U. Heider, R. Oesten and M. Schmidt, *J. Electrochem. Soc.*, 2000, **147**, 1322–1331.
- 141 J. Li, J. Zhang, X. Zhang, C. Yang, N. Xu and B. Xia, *Electrochim. Acta*, 2010, **55**, 927–934.
- 142 M. Ecker, J. B. Gerschler, J. Vogel, S. Käbitz, F. Hust, P. Dechent and D. U. Sauer, *J. Power Sources*, 2012, **215**, 248–257.
- 143 J. Fan and S. Tan, *J. Electrochem. Soc.*, 2006, **153**, A1081.
- 144 M. Broussely, S. Herreyre, P. Biensan, P. Kasztejna, K. Nechev and R. J. Staniewicz, *J. Power Sources*, 2001, **97-98**, 13–21.
- 145 P. Niehoff, E. Kraemer and M. Winter, *J. Electroanal. Chem.*, 2013, **707**, 110–116.
- 146 W. Waag, S. Käbitz and D. U. Sauer, *Appl. Energy*, 2013, **102**, 885–897.

- 147 I. Bloom, L. K. Walker, J. K. Basco, D. P. Abraham, J. P. Christophersen and C. D. Ho, *J. Power Sources*, 2010, **195**, 877–882.
- 148 V. Zinth, C. von Lüders, M. Hofmann, J. Hattendorff, I. Buchberger, S. Erhard, J. Rebelo-Kornmeier, A. Jossen and R. Gilles, *J. Power Sources*, 2014, **271**, 152–159.
- 149 K. Takahashi and V. Srinivasan, *J. Electrochem. Soc.*, 2015, **162**, A635–A645.
- 150 J. Christensen, *J. Electrochem. Soc.*, 2010, **157**, A366–A380.
- 151 K. An, P. Barai, K. Smith and P. P. Mukherjee, *J. Electrochem. Soc.*, 2014, **161**, A1058–A1070.
- 152 N. Omar, M. A. Monem, Y. Firouz, J. Salminen, J. Smekens, O. Hegazy, H. Gaulous, G. Mulder, P. Van den Bossche, T. Coosemans and J. Van Mierlo, *Appl. Energy*, 2014, **113**, 1575–1585.
- 153 T. Yuan, X. Yu, R. Cai, Y. Zhou and Z. Shao, *J. Power Sources*, 2010, **195**, 4997–5004.
- 154 K. Zaghbi, M. Dontigny, P. Perret, a. Guerfi, M. Ramanathan, J. Prakash, a. Mauger and C. M. Julien, *J. Power Sources*, 2014, **248**, 1050–1057.
- 155 K. Chen, Z. Yu, S. Deng, Q. Wu, J. Zou and X. Zeng, *J. Power Sources*, 2015, **278**, 411–419.
- 156 J. S. Wang, P. Liu, S. Soukiazian, H. Tataria, M. Dontigny, A. Guerfi, K. Zaghbi and M. W. Verbrugge, *J. Power Sources*, 2014, **256**, 288–293.
- 157 A. Senyshyn, M. J. Mühlbauer, O. Dolotko and H. Ehrenberg, *J. Power Sources*, 2015, **282**, 235–240.
- 158 W. Chang, S.-J. Kim, I.-T. Park, B.-W. Cho, K. Y. Chung and H.-C. Shin, *J. Alloys Compd.*, 2013, **563**, 249–253.
- 159 M. Ecker, N. Nieto, S. Käbitz, J. Schmalstieg, H. Blanke, A. Warnecke and D. U. Sauer, *J. Power Sources*, 2014, **248**, 839–851.
- 160 B. Bitzer and A. Gruhle, *J. Power Sources*, 2014, **262**, 297–302.
- 161 N. N. Bramnik, D. M. Trots, H. J. Hofmann and H. Ehrenberg, *Phys. Chem. Chem. Phys.*, 2009, **11**, 3271–3277.
- 162 K. Du, L.-H. Zhang, Y.-B. Cao, H. Guo, Z.-D. Peng and G.-R. Hu, *J. Appl. Electrochem.*, 2011, **41**, 1349–1355.
- 163 H. Gwon, D. H. Seo, S. W. Kim, J. Kim and K. Kang, *Adv. Funct. Mater.*, 2009, **19**, 3285–3292.
- 164 K.-W. Nam, X.-J. Wang, W.-S. Yoon, H. Li, X. Huang, O. Haas, J. Bai and X.-Q. Yang, *Electrochem. Commun.*, 2009, **11**, 913–916.
- 165 Q.-Q. Zou, G.-N. Zhu and Y.-Y. Xia, *J. Power Sources*, 2012, **206**, 222–229.
- 166 G. Rousse, J. Rodriguez-Carvajal, S. Patoux and C. Masquelier, *Chem. Mater.*, 2003, **15**, 4082–4090.

- 167 M. S. Islam, D. J. Driscoll, C. A. J. Fisher and P. R. Slater, *Chem. Mater.*, 2005, **17**, 5085–5092.
- 168 C. A. J. Fisher, V. M. Hart Prieto and M. S. Islam, *Chem. Mater.*, 2008, **20**, 5907–5915.
- 169 K. Momma and F. Izumi, *J. Appl. Crystallogr.*, 2011, **44**, 1272–1276.
- 170 Q. Liu, Z. Liu, G. Xiao and S. Liao, *Ionics*, 2013, **19**, 445–450.
- 171 H. Gao, L. Jiao, J. Yang, Z. Qi, Y. Wang and H. Yuan, *Electrochim. Acta*, 2013, **97**, 143–149.
- 172 S.-Y. Chung, J. T. Bloking and Y.-M. Chiang, *Nat. Mater.*, 2002, **1**, 123–128.
- 173 G. Kobayashi, A. Yamada, S. I. Nishimura, R. Kanno, Y. Kobayashi, S. Seki, Y. Ohno and H. Miyashiro, *J. Power Sources*, 2009, **189**, 397–401.
- 174 A. Yamada, Y. Kudo and K.-Y. Liu, *J. Electrochem. Soc.*, 2001, **148**, A1153–A1158.
- 175 J. Molenda, W. Ojczyk and J. Marzec, *J. Power Sources*, 2007, **174**, 689–694.
- 176 D. Wang, Z. Wang, X. Huang and L. Chen, *J. Power Sources*, 2005, **146**, 580–583.
- 177 R. D. Shannon, *Acta Crystallogr., Sect. A Found. Crystallogr.*, 1976, **32**, 751–767.
- 178 A. Yamada, Y. Kudo and K.-Y. Liu, *J. Electrochem. Soc.*, 2001, **148**, A747–A754.
- 179 S. M. Rommel, J. Rothballer, N. Schall, C. Brünig and R. Wehrich, *Ionics*, 2015, **21**, 325–333.
- 180 A. S. Andersson, B. Kalska, L. Häggström and J. O. Thomas, *Solid State Ionics*, 2000, **130**, 41–52.
- 181 Z. Li and I. Shinno, *Mineral. J.*, 1997, **19**, 99–107.
- 182 V. Rusakov, S. Yaroslavtsev, M. Matsnev, T. Kulova, A. Skundin, S. Novikova and A. Yaroslavtsev, *Hyperfine Interact.*, 2014, **226**, 791–796.
- 183 I. K. Lee, I.-B. Shim and C. S. Kim, *J. Appl. Phys.*, 2010, **107**, 09A522.
- 184 S. Novikova, S. Yaroslavtsev, V. Rusakov, T. Kulova, A. Skundin and A. Yaroslavtsev, *Electrochim. Acta*, 2014, **122**, 180–186.
- 185 I. K. Lee, C. M. Kim, S. J. Kim and C. S. Kim, *J. Appl. Phys.*, 2012, **111**, 07D722.
- 186 S. A. Novikova, S. A. Yaroslavtsev, V. S. Rusakov, T. L. Kulova, A. M. Skundin and A. B. Yaroslavtsev, *Mendeleev Commun.*, 2013, **23**, 251–252.
- 187 S.-Y. Yan, C.-Y. Wang, R.-M. Gu, S. Sun and M.-W. Li, *J. Alloys Compd.*, 2015, **628**, 471–479.
- 188 S. Li, Z. Su, X. Jiang and A. Muslim, *Mater. Lett.*, 2015, **154**, 29–32.
- 189 B. Zhang, X. Wang, H. Li and X. Huang, *J. Power Sources*, 2011, **196**, 6992–6996.
- 190 N. Penazzi, M. Arrabito, M. Piana, S. Bodoardo, S. Panero and I. Amadei, *J. Eur. Ceram. Soc.*, 2004, **24**, 1381–1384.

- 191 R. Qing, M.-C. Yang, Y. S. Meng and W. Sigmund, *Electrochim. Acta*, 2013, **108**, 827–832.
- 192 P. S. Herle, B. Ellis, N. Coombs and L. F. Nazar, *Nat. Mater.*, 2004, **3**, 147–152.
- 193 B. Ellis, P. Subramanya Herle, Y. H. Rho, L. F. Nazar, R. Dunlap, L. K. Perry and D. H. Ryan, *Faraday Discuss.*, 2007, **134**, 119–141.
- 194 Gangulibabu, D. Bhuvanewari, N. Kalaiselvi, N. Jayaprakash and P. Periasamy, *J. Sol-Gel Sci. Technol.*, 2009, **49**, 137–144.
- 195 J. R. Croy, M. Balasubramanian, D. Kim, S.-H. Kang and M. M. Thackeray, *Chem. Mater.*, 2011, **23**, 5415–5424.
- 196 T. Muraliganth and A. Manthiram, *J. Phys. Chem. C*, 2010, **114**, 15530–15540.
- 197 G. Li, H. Azuma and M. Tohda, *J. Electrochem. Soc.*, 2002, **149**, A743–A747.
- 198 Z.-H. Wang, L.-X. Yuan, W.-X. Zhang and Y.-H. Huang, *J. Alloys Compd.*, 2012, **532**, 25–30.
- 199 R. Malik, F. Zhou and G. Ceder, *Nat. Mater.*, 2011, **10**, 587–590.
- 200 V. Srinivasan and J. Newman, *J. Electrochem. Soc.*, 2004, **151**, A1517–A1529.
- 201 C. Delmas, M. Maccario, L. Croguennec, F. Le Cras and F. Weill, *Nat. Mater.*, 2008, **7**, 665–671.
- 202 A. S. Andersson and J. O. Thomas, *J. Power Sources*, 2001, **97-98**, 498–502.
- 203 J. Wang, Y. K. Chen-Wiegart and J. Wang, *Nat. Commun.*, 2014, **5**, 1–10.
- 204 N. Meethong, H. Y. S. Huang, S. A. Speakman, W. C. Carter and Y. M. Chiang, *Adv. Funct. Mater.*, 2007, **17**, 1115–1123.
- 205 B. Kang and G. Ceder, *Nature*, 2009, **458**, 190–193.
- 206 C. Delacourt, P. Poizot, J.-M. Tarascon and C. Masquelier, *Nat. Mater.*, 2005, **4**, 254–260.
- 207 N. Meethong, H.-Y. S. Huang, W. C. Carter and Y.-M. Chiang, *Electrochem. Solid-State Lett.*, 2007, **10**, A134–A138.
- 208 G. Kobayashi, S. I. Nishimura, M.-S. S. Park, R. Kanno, M. Yashima, T. Ida and A. Yamada, *Adv. Funct. Mater.*, 2009, **19**, 395–403.
- 209 A. Yamada, H. Koizumi, S.-I. Nishimura, N. Sonoyama, R. Kanno, M. Yonemura, T. Nakamura and Y. Kobayashi, *Nat. Mater.*, 2006, **5**, 357–360.
- 210 A. Yamada, H. Koizumi, N. Sonoyama and R. Kanno, *Electrochem. Solid-State Lett.*, 2005, **8**, A409–A413.
- 211 X. Zhang, M. Van Hulzen, D. P. Singh, A. Brownrigg, J. P. Wright, N. H. Van Dijk and M. Wagemaker, *Nano Lett.*, 2014, **14**, 2279–2285.
- 212 Y. Orikasa, T. Maeda, Y. Koyama, H. Murayama, K. Fukuda, H. Tanida, H. Arai, E. Matsubara, Y. Uchimoto and Z. Ogumi, *J. Am. Chem. Soc.*, 2013, **135**, 5497–500.

- 213 S. Nishimura, R. Natsui and A. Yamada, *Angew. Chemie Int. Ed.*, 2015, **54**, 1–4.
- 214 H. Ehrenberg, N. N. Bramnik, A. Senyshyn and H. Fuess, *Solid State Sci.*, 2009, **11**, 18–23.
- 215 H. Ju, J. Wu and Y. Xu, *Int. J. Energy Environ. Eng.*, 2013, **4**, 2–7.
- 216 A. Osnis, M. Kosa, D. Aurbach and D. T. Major, *J. Phys. Chem. C*, 2013, **117**, 17919–17926.
- 217 S. T. Sun, C. Q. Du, J. W. Wu, Z. Y. Tang, M. Yang and X. H. Zhang, *Ionics*, 2014, **20**, 1627–1634.
- 218 D. W. Han, Y. M. Kang, R. Z. Yin, M. S. Song and H. S. Kwon, *Electrochem. Commun.*, 2009, **11**, 137–140.
- 219 C. Delacourt, P. Poizot, M. Morcrette, J.-M. Tarascon and C. Masquelier, *Chem. Mater.*, 2004, **16**, 93–99.
- 220 G. Li, H. Azuma and M. Tohda, *Electrochem. Solid-State Lett.*, 2002, **5**, A135–A137.
- 221 C. V. Ramana, A. Ait-Salah, S. Utsunomiya, U. Becker, A. Mauger, F. Gendron and C. M. Julien, *Chem. Mater.*, 2006, **18**, 3788–3794.
- 222 N. N. Bramnik, K. G. Bramnik, K. Nikolowski, M. Hinterstein, C. Baetz and H. Ehrenberg, *Electrochem. Solid-State Lett.*, 2005, **8**, A379–A381.
- 223 K. W. Nam, W. S. Yoon, K. Zaghbi, K. Yoon Chung and X. Q. Yang, *Electrochem. commun.*, 2009, **11**, 2023–2026.
- 224 M. R. Roberts, G. Vitins, G. Denuault and J. R. Owen, *J. Electrochem. Soc.*, 2010, **157**, A381–A386.
- 225 J. Molenda, W. Ojczyk, K. Świerczek, W. Zajac, F. Krok, J. Dygas and R. S. Liu, *Solid State Ionics*, 2006, **177**, 2617–2624.
- 226 N. V. Kosova, E. T. Devyatkina, a. I. Ancharov, a. V. Markov, D. D. Karnaushenko and V. K. Makukha, *Solid State Ionics*, 2012, **225**, 564–569.
- 227 R. Malik, F. Zhou and G. Ceder, *Phys. Rev. B*, 2009, **79**, 1–7.
- 228 D. Baster, K. Zheng, W. Zajac, K. Świerczek and J. Molenda, *Electrochim. Acta*, 2013, **92**, 79–86.
- 229 F. Omenya, J. K. Miller, J. Fang, B. Wen, R. Zhang, Q. Wang, N. A. Chernova and M. S. Whittingham, *Chem. Mater.*, 2014, **26**, 6206–6212.
- 230 M. R. Giuliano, A. K. Prasad and S. G. Advani, *J. Power Sources*, 2012, **216**, 345–352.
- 231 D. Bernardi, E. Pawlikowski and J. Newman, *J. Electrochem. Soc.*, 1985, **132**, 5–12.
- 232 T. M. Bandhauer, S. Garimella and T. F. Fuller, *J. Electrochem. Soc.*, 2011, **158**, R1–R25.
- 233 K. E. Thomas and J. Newman, *J. Electrochem. Soc.*, 2003, **150**, A176–A192.
- 234 W. B. Gu and C. Y. Wang, *J. Electrochem. Soc.*, 2000, **147**, 2910–2922.

- 235 G. Liu, M. Ouyang, L. Lu, J. Li and X. Han, *J. Therm. Anal. Calorim.*, 2014, **116**, 1001–1010.
- 236 T. M. Bandhauer, S. Garimella and T. F. Fuller, *J. Power Sources*, 2014, **247**, 618–628.
- 237 K. Smith and C.-Y. Wang, *J. Power Sources*, 2006, **160**, 662–673.
- 238 G. G. Botte, B. A. Johnson and R. E. White, *J. Electrochem. Soc.*, 1999, **146**, 914–923.
- 239 S. C. Chen, C. C. Wan and Y. Y. Wang, *J. Power Sources*, 2005, **140**, 111–124.
- 240 L. Song and J. W. Evans, *J. Electrochem. Soc.*, 2000, **147**, 2086–2095.
- 241 J. P. Schmidt, A. Weber and E. Ivers-Tiffée, *Electrochim. Acta*, 2014, **137**, 311–319.
- 242 K. E. Thomas, C. Bogatu and J. Newman, *J. Electrochem. Soc.*, 2001, **148**, A570–A575.
- 243 J. L. Dodd, Phase Composition and Dynamical Studies of Lithium Iron Phosphate. Ph.D. thesis, California Institute of Technology, California, 2007, pp. 75–94.
- 244 K. Takano, Y. Saito, K. Kanari, K. Nozaki, K. Kato, a. Negishi and T. Kato, *J. Appl. Electrochem.*, 2002, **32**, 251–258.
- 245 T. Kashiwagi, M. Nakayama, K. Watanabe, M. Wakihara, Y. Kobayashi and H. Miyashiro, *J. Phys. Chem. B*, 2006, **110**, 4998–5004.
- 246 Y. Kobayashi, Y. Mita, S. Seki, Y. Ohno, H. Miyashiro, M. Nakayama and M. Wakihara, *J. Electrochem. Soc.*, 2008, **155**, A14–A19.
- 247 M. Nakayama, M. Wakihara, Y. Kobayashi and H. Miyashiro, *J. Phys. Chem. B*, 2005, **109**, 14648–14653.
- 248 R. Yazami, Y. Reynier and B. Fultz, *ECS Trans.*, 2006, **1**, 87–96.
- 249 Y. Reynier, J. Graetz, T. Swan-Wood, P. Rez, R. Yazami and B. Fultz, *Phys. Rev. B*, 2004, **70**, 174304.
- 250 Y. F. Reynier, R. Yazami and B. Fultz, *J. Electrochem. Soc.*, 2004, **151**, A422–A426.
- 251 S. Bach, J. P. Pereira-Ramos, N. Baffier and R. Messina, *J. Electrochem. Soc.*, 1990, **137**, 1042–1048.
- 252 Y. Reynier, R. Yazami and B. Fultz, *J. Power Sources*, 2003, **119-121**, 850–855.
- 253 K. Kai, Y. Kobayashi, H. Miyashiro, G. Oyama, S. I. Nishimura, M. Okubo and A. Yamada, *ChemPhysChem*, 2014, **15**, 2156–2161.
- 254 M. Kitta, T. Akita, S. Tanaka and M. Kohyama, *J. Power Sources*, 2014, **257**, 120–125.
- 255 K. Kanamura, T. Umegaki, H. Naito, Z. Takehara and T. Yao, *J. Appl. Electrochem.*, 2001, **31**, 73–78.
- 256 W. Lu, I. Belharouak, J. Liu and K. Amine, *J. Power Sources*, 2007, **174**, 673–677.

- 257 V. V. Viswanathan, D. Choi, D. Wang, W. Xu, S. Towne, R. E. Williford, J. G. Zhang, J. Liu and Z. Yang, *J. Power Sources*, 2010, **195**, 3720–3729.
- 258 M. Wagemaker, D. R. Simon, E. M. Kelder, J. Schoonman, C. Ringpfeil, U. Haake, D. Lützenkirchen-Hecht, R. Frahm and F. M. Mulder, *Adv. Mater.*, 2006, **18**, 3169–3173.
- 259 S. Al Hallaj, R. Venkatachalapathy, J. Prakash and J. R. Selman, *J. Electrochem. Soc.*, 2000, **147**, 2432–2436.
- 260 M. Brand, S. Gläser, J. Geder, S. Menacher, S. Obpacher, A. Jossen and D. Quinger, in *EVS27 International Battery, Hybrid and Fuel Cell Electric Vehicle Symposium*, 2013, pp. 1–9.
- 261 J. Ni, W. Liu, J. Liu, L. Gao and J. Chen, *Electrochem. Commun.*, 2013, **35**, 1–4.
- 262 C. Du, Z. Tang, J. Wu, H. Tang and X. Zhang, *Electrochim. Acta*, 2014, **125**, 58–64.
- 263 L. Wang, P. Zuo, G. Yin, Y. Ma, X. Cheng, C. Du and Y. Gao, *J. Mater. Chem. A*, 2015, **3**, 1569–1579.
- 264 K. Xu, *Chem. Rev.*, 2014, **114**, 11503–11618.
- 265 M. Hu, X. Pang and Z. Zhou, *J. Power Sources*, 2013, **237**, 229–242.
- 266 Z. Zhang, L. Hu, H. Wu, W. Weng, M. Koh, P. C. Redfern, L. a. Curtiss and K. Amine, *Energy Environ. Sci.*, 2013, **6**, 1806.
- 267 R. Sharabi, E. Markevich, K. Fridman, G. Gershinsky, G. Salitra, D. Aurbach, G. Semrau, M. A. Schmidt, N. Schall and C. Bruenig, *Electrochem. Commun.*, 2013, **28**, 20–23.
- 268 J. L. Allen, J. L. Allen, S. A. Delp and T. R. Jow, *ECS Trans.*, 2014, **61**, 63–68.
- 269 M. Hu, J. Wei, L. Xing and Z. Zhou, *J. Appl. Electrochem.*, 2012, **42**, 291–296.
- 270 D. Di Lecce, S. Brutti, S. Panero and J. Hassoun, *Mater. Lett.*, 2015, **139**, 329–332.
- 271 V. Borgel, E. Markevich, D. Aurbach, G. Semrau and M. Schmidt, *J. Power Sources*, 2009, **189**, 331–336.



ISBN 978-952-60-6551-9 (printed)  
ISBN 978-952-60-6552-6 (pdf)  
ISSN-L 1799-4934  
ISSN 1799-4934 (printed)  
ISSN 1799-4942 (pdf)

**Aalto University**  
**School of Chemical Technology**  
**Department of Chemistry**  
[www.aalto.fi](http://www.aalto.fi)

**BUSINESS +  
ECONOMY**

**ART +  
DESIGN +  
ARCHITECTURE**

**SCIENCE +  
TECHNOLOGY**

**CROSSOVER**

**DOCTORAL  
DISSERTATIONS**